Angewandte Physik

Excitation and control of spin-wave dynamics by spin-orbit torques in ultrathin YIG/Pt structures

Inaugural-Dissertation
zur Erlangung des Doktorgrades
der Naturwissenschaften im Fachbereich Physik
der Mathematisch-Naturwissenschaftlichen Fakultät
der Westfälischen Wilhelms-Universität Münster

vorgelegt von
Michael Evelt
aus Werne

– 2018 –

Dekan: Prof. Dr. Michael Klasen

Erster Gutachter: Prof. Dr. Sergej O. Demokritov

Zweiter Gutachter: Prof. Dr. Carsten Fallnich

Tag der mündlichen Prüfung:

Tag der Promotion:

“An expert is a person who has found out by his own painful experience all the mistakes that one can make in a very narrow field.”

–Niels Bohr, 1885-1962

Abstract

In this thesis, the influence of spin-orbit torques on the magnetization dynamics in a magnetic insulator is investigated experimentally. Therefore, ultrathin Yttrium Iron Garnet (YIG) films with an adjacent platinum (Pt) layer – patterned in a variety of shapes – are examined at room temperature. A static magnetic field is applied to magnetize the YIG layer to saturation and fix the equilibrium orientation of the magnetization vector. In all experiments, an electric current is sent through the Pt layer that due to the strong spin-orbit coupling in Pt is converted into a pure spin current by means of the spin-Hall effect (SHE). This spin current is injected into the adjacent YIG layer where it exerts a spin transfer torque (STT) on the magnetization. The combination of spin-current formation by spin-orbit interaction and injection with the subsequent spin transfer torque is referred to as spin-orbit torque (SOT). For a properly chosen orientation of the electric current and the magnetic field, SOT can be used to effectively compensate the natural damping of the system and excite spin waves by driving it out of thermal equilibrium. By applying sufficiently strong SOT, the natural damping can even be fully compensated at a critical electric current, leading to the excitation of coherent auto-oscillations.

In this thesis, four experimental studies are presented that demonstrate efficient excitation and control of spin waves by SOT. Spin wave behaviors for electric currents below and above the point of full dissipation compensation are investigated. The measurements are performed using a frequency-, space- and time-resolved Brillouin light scattering (BLS) setup.

The first experiment demonstrates the first spatially resolved investigation of auto-oscillations in a YIG/Pt bilayer, revealing an efficient nonlinear mode coupling for high spin-wave amplitudes in YIG that leads to the formation of a spatially extended auto-oscillation mode.

In the second study, a microwave antenna on a YIG/Pt bilayer stripe waveguide is used to inductively excite coherently propagating spin waves. It is demonstrated that under the influence of SOT, the propagation length of the coherently excited spin waves can be precisely controlled. Still, at the point of full damping compensation, high amplitude spin waves excited by SOT lead to strong scattering of the propagating spin waves, so that true amplification cannot be achieved.

The third investigation presents the first experimental realization of auto-oscillations in a YIG nanowire excited by SOT, where the YIG layer is not directly grown on the typically used substrate Gadolinium Gallium Garnet (GGG), but on a Pt layer. Although the structural quality is inevitably reduced due to a stronger lattice mismatch between YIG and the substrate, which is accompanied by an increment of the natural damping, the critical current density is comparable to values measured for structures grown in the traditional order. The demonstrated setup is a first step to more flexible YIG based designs that will enable future structures to, for example, use double sided spin-current injections, which is impossible for YIG films that are directly grown on GGG.

The fourth and final experimental study demonstrates a method to locally excite auto-oscillations by SOT in an extended Bi doped YIG (BiYIG) film by using a Pt stripe on top of the film. The auto-oscillating region excites coherent spin waves that propagate through the surrounding unconfined BiYIG film. In previous investigations, the emission of coherent spin waves was hindered by the nonlinear frequency red shift in the auto-oscillation regime, caused by the large amplitudes of the magnetization dynamics leading to an effective reduction of the magnetization. In the BiYIG films presented here, the influence of the magnetization on the precession frequency is compensated by a significant perpendicular magnetic anisotropy (PMA). Accordingly, the high amplitude auto-oscillations are not accompanied by a frequency red shift and the demonstrated setup can be used as an SOT driven emitter of coherently propagating spin waves.

Zusammenfassung

In dieser Arbeit wird der Einfluss von Spin-Bahn-Drehmomenten auf die Magnetisierungsdynamik in magnetischen Isolatoren experimentell untersucht. Zu diesem Zweck werden ultradünne Yttrium-Eisen-Granat (YIG) Filme mit einer angrenzenden Platinschicht (Pt) in einer Vielzahl von Strukturen bei Raumtemperatur untersucht. Ein statisches Magnetfeld wird angelegt, um die YIG Schicht zur Sättigung zu magnetisieren und die Gleichgewichtsorientierung des Magnetisierungsvektors festzulegen. In allen Experimenten wird ein elektrischer Strom durch die Pt-Schicht geleitet, welcher, aufgrund der starken Spin-Bahn-Kopplung in Pt und dem damit verbundenen Spin-Hall-Effekt (SHE), in einen reinen Spinstrom umgewandelt wird. Dieser Spinstrom wird in die benachbarte YIG-Schicht injiziert, wo er ein Spinübertragungsdrehmoment (STT) auf die Magnetisierung ausübt. Die Kombination aus der Bildung eines Spinstromes durch die Spin-Bahn-Wechselwirkung und dessen Injektion mit dem nachfolgenden Spinübertragungsdrehmoment wird als Spin-Bahn Drehmoment (SOT) bezeichnet. Für eine entsprechend gewählte Ausrichtung des elektrischen Stroms und des Magnetfeldes können SOT genutzt werden, um die natürliche Dämpfung zu kompensieren und Spinwellen anzuregen, indem sie das untersuchte System aus dem thermischen Gleichgewicht bringen. Durch die Verwendung hinreichend starker SOT kann die natürliche Dämpfung des Systems sogar vollständig ausgeglichen werden, was zur Anregung kohärenter Autooszillationen führt. Der dazu benötigte elektrische Strom wird als kritischer Strom bezeichnet.

In dieser Arbeit werden vier experimentelle Studien vorgestellt, welche die effiziente Anregung und Steuerung von Spinwellen durch SOT demonstrieren. Das Verhalten von Spinwellen für elektrische Ströme unterhalb und oberhalb des Punktes der vollständigen Dissipationskompensation wird untersucht. Die Messungen werden mit einem frequenz-, orts- und zeitaufgelösten Brillouin-Lichtstreuungs (BLS)

Aufbau durchgeführt.

Das erste Experiment zeigt die erste ortsaufgelöste Untersuchung von durch SOT angeregten Autooszillationen in einer YIG/Pt-Doppelschicht. Es wird eine effiziente nichtlineare Modenkopplung bei hohen Spinwellen-Amplituden in YIG beobachtet, die zur Ausbildung einer räumlich ausgedehnten Autooszillationsmode führt.

In der zweiten Studie wird eine Mikrowellenantenne auf einem YIG/Pt-Doppelschicht Streifenwellenleiter verwendet, um kohärent propagierende Spinwellen induktiv anzuregen. Es kann gezeigt werden, dass unter dem Einfluss von SOT eine präzise Steuerung der Propagationslänge von kohärent angeregten Spinwellen möglich ist. Dennoch kann keine tatsächliche Verstärkung der Spinwellen erreicht werden, da an dem Punkt der vollständigen Dämpfungskompensation durch SOT, Spinwellen mit hoher Amplitude angeregt werden. Diese führen zu einer starken Streuung der sich ausbreitenden Spinwellen, so dass eine echte Verstärkung nicht erreicht werden kann.

Die dritte Untersuchung präsentiert die erste experimentelle Realisierung von Autooszillationen in einem von SOT angeregten YIG-Nanodraht, in dem die YIG-Schicht nicht direkt auf dem typischerweise verwendeten Substrat Gadolinium Gallium Garnet (GGG) gewachsen wurde, sondern auf einer Pt-Schicht. Obwohl die unvermeidbar verminderte strukturelle Qualität der magnetischen Schicht, aufgrund einer stärkeren Abweichung der Gittereigenschaften zwischen YIG und dem Substrat, von einer Erhöhung der natürlichen Dämpfung begleitet wird, ist die kritische Stromdichte vergleichbar mit gemessenen Werten für Strukturen, die in der traditionellen Reihenfolge erstellt wurden. Der demonstrierte Aufbau ist ein erster Schritt zu flexibleren YIG-basierte Designs, die es zukünftigen Strukturen ermöglicht, zum Beispiel doppelseitige Spinstrom-Injektion zu verwenden – eine Möglichkeit, welche für YIG-Filme, die direkt auf GGG gewachsen wurden, nicht gegeben ist.

Die vierte und letzte experimentelle Studie zeigt eine Methode zur lokalen Anregung von Autooszillationen durch SOT in einem ausgedehnten Bi-dotierten YIG-Film (BiYIG) unter Verwendung eines Pt Streifens auf dem Film. Die autooszillierende Region regt kohärente Spinwellen an, die sich durch den umgebenden, ausgedehnten BiYIG Film ausbreiten. In früheren Untersuchungen wurde die Emission von kohärenten Spinwellen durch die nichtlineare Frequenzrotverschiebung in der Gegenwart von Autooszillation unterdrückt. Die Frequenzreduktion wurde durch die hohen Amplituden der Magnetisierungsdynamik und die damit verbundene Reduktion der Magnetisierung ausgelöst. In den hier verwendeten BiYIG Filmen ist der Einfluss der Magnetisierung auf die Frequenz durch eine signifikante senkrechte magnetische Anisotropie (PMA) kompensiert. Dementsprechend tritt hier keine Frequenzrotverschiebung in der Gegenwart von Autooszillationen auf und der demonstrierte Versuchsaufbau kann als SOT-getriebener Emitter von sich kohärent ausbreitenden Spinwellen verwendet werden.

Contents

1 Introduction

In common electric devices, information is transferred, detected and stored using the electric charge of the electron. In spintronics [1,2], this approach is extended by an additional degree of freedom – the orientation of the electron spin in space. Probably, the most famous example is the giant magneto resistance (GMR) discovered by Grünberg and Fert [3, 4], that was used in improved hard drive reading heads developed by IBM already shortly after its discovery. The discovery was granted with the Nobel Prize in physics (2007).

A subfield of spintronics, the emerging field of magnonics [5], focuses on processing information by making use of the unique properties of spin waves – a phase-coherent precession of spin magnetic moments [6] – that was first described by Bloch already in 1930 [7]. The name magnonics originates in the quasiparticle representation of the spin wave – the magnon – which can be regarded as a collective excitation of a magnetically ordered system. The objective of magnonics is to examine the dynamic behavior of magnetic nanostructures and to use the gained insights to design new technical applications [5, 8]. A typical magnonic device consists of a source and a detector to excite and detect the spin wave, a functional medium that allows for spin-wave propagation over sufficiently large distances and an external control that enables manipulation of the transmitted information [5]. Since the excitation efficiency is mainly responsible for the energy consumption and reliability of magnonic devices, this step is of high interest. The original and still widely used method is the inductive excitation of spin waves where an alternating electric current in a microwave antenna or a cavity leads to the formation of an Oersted field that couples to the magnetic moment via the dipolar interaction [9–11]. Still, this method faces several shortcomings [11], so that another method would be desirable.

In 1996, Slonczewski [12] and Berger [13] independently predicted a possibility to excite spin waves in magnetic multilayers by direct spin-polarized electric currents passing through the structure. Via the exchange interaction, the angular momentum carried by the so-called spin current is transferred to the magnetic system leading to the formation of a damping like torque acting on the magnetization. This process is referred to as spin-transfer torque and is accompanied by a reduction of the current polarization. Depending on the orientation of the spin polarization relative to the magnetization alignment, it can lead to either a suppression or an enhancement of spin-wave modes in the system and is accompanied by an effective reduction or increment of the natural dissipation.

Since its first experimental demonstration [14], the interest in current driven spin-wave excitation steadily increased [15]. However, the multilayer STT approach faces several problems. Since the electric current has to flow through the magnetic layer, a top electrode on the excited magnet is needed, preventing the use of magnetooptical investigation methods like BLS [11]. Also, the usage of magnetic insulators is excluded by this setup that are of particular interest for magnonic devices due to their superior dissipation properties compared to metallic magnets. Accordingly, to integrate insulating materials into applications, the transfer of angular momentum to the magnetic system by STT has to be realized by pure spin currents – spin currents that are not accompanied by an electric current in the magnetic layer. This can be achieved by making use of the spin-Hall effect [16] that converts a direct electric current by spin-orbit interaction into a transverse pure spin current. In the past decade, significant progress could be made by combining metallic magnets like permalloy (Py) with materials with a strong spin-orbit coupling (for example Pt) in bilayers. The injected spin-current was used to drive the system out of thermal equilibrium and effectively control magnetic fluctuations [17, 18] and even to fully compensate the natural damping of the system and excite SOT driven auto-oscillations in so-called nano-oscillators [19–22]. Although the lower damping in magnetic insulators like YIG should simplify the full compensation of the dissipation, the inverse proportionality of the SOT effectivity to the magnetic film thickness [12, 13, 23] was presenting a major problem. Only recently – with the successful fabrication of high-quality ultrathin YIG films [24–26] – significant progress could be made and the excitation of magnetization auto-oscillations excited by SOT in YIG/Pt bilayers could be observed [27, 28].

This thesis is dedicated to further increase the understanding of the magnetization dynamics in ultrathin YIG films driven by SOT. Therefore, a variety of YIG/Pt bilayer structures are studied experimentally. It is demonstrated that SOT presents an efficient mechanism to excite and control coherent and incoherent magnetization dynamics in magnetic insulators. The measurements are performed by using a frequency-, space- and time-resolved micro-Brillouin light scattering (μBLS) setup. The experimental claims are supported by micromagnetic simulations and analytical calculations. The present work is organized as follows:

Chapter 2 presents a brief summary of the theoretical considerations of spin waves in confined geometries under the influence of different excitation mechanisms. The subjects of chapter 3 are experimental and numerical methods used to examine spin-wave phenomena in chapter 4 where four experimental studies on ultrathin YIG/Pt bilayers are presented in the chronological order in which they were performed. Finally, in chapter 5, the obtained results will be discussed and summarized.

2 General concepts of spin waves

In this chapter the general concepts of spin waves will be presented. Therefore, the equation of motion by Landau and Lifshitz will be examined. The discussion will then be extended to spin waves in a confined magnet and and under the influence of different excitation mechanisms.

The spin of an electron is connected with the appearence of a magnetic moment μ. In a magnetically ordered system it is not nescessary to consider each electron individually, but a continuous approach can be chosen [29]. Therefore we define the magnetization vector $\boldsymbol{M}(\boldsymbol{r},t)$ as the density of magnetic moments $\boldsymbol{\mu}(\boldsymbol{r},t)$ in a unit volume ΔV [6]:

$$\boldsymbol{M}(\boldsymbol{r},t) = \frac{\sum_{\Delta V} \boldsymbol{\mu}(\boldsymbol{r},t)}{\Delta V}. \tag{2.1}$$

In case of full parallel alignment of the magnetic moments the magnitude of the magnetization vector is maximized to the saturation magnetization M_s.
The reaction of the magnetization to disturbances by magnetic fields is given by the Landau-Lifshitz equation (LLE, 1935) [30]:

$$\frac{\partial \boldsymbol{M}}{\partial t} = -\gamma(\boldsymbol{M} \times \boldsymbol{H}_\mathrm{eff}). \tag{2.2}$$

The effective magnetic field $\boldsymbol{H}_\mathrm{eff}$ can be regarded as the sum of effective and real magnetic fields:

$$\boldsymbol{H}_\mathrm{eff} = \boldsymbol{H}_\mathbf{0} + \boldsymbol{H}_\mathrm{a} + \boldsymbol{h}_\mathrm{dyn} + \boldsymbol{h}_\mathrm{ex} + \boldsymbol{h}_\mathrm{d} + \dots \tag{2.3}$$

with $\boldsymbol{H}_\mathbf{0}$ as a static magnetic field, $\boldsymbol{H}_\mathrm{a}$ as the anisotropy field, $\boldsymbol{h}_\mathrm{dyn}$ as a dynamic excitation field (see section 2.2.1), $\boldsymbol{h}_\mathrm{ex}$ as the effective field describing the exchange interaction between neighboring spins (see below) and $\boldsymbol{h}_\mathrm{d}$ representing the dipolar interaction of the magnetic moments of the electron (see below). Due to quantum mechanical connection of the electron magnetic moment with its angular momentum [6], the right side of equation (2.2) can be regarded as a torque that is exerted on the magnetization vector mediated by the real and effective magnetic fields. Since this torque is perpendicular to the magnetization vector at all times (see Fig. 2.1), only its orientation in space is altered, but never the absolute value of the magneti-

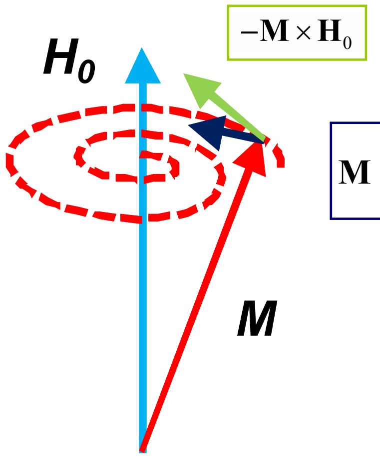

Fig. 2.1: Magnetization precession. The Landau-Lifshitz torque (green) forces a right hand precession around the static magnetic field $\boldsymbol{H}_0$. The Gilbert torque (purple) exerts a torque on the magnetization towards $\boldsymbol{H}_0$ (phenomenological damping term) [31].

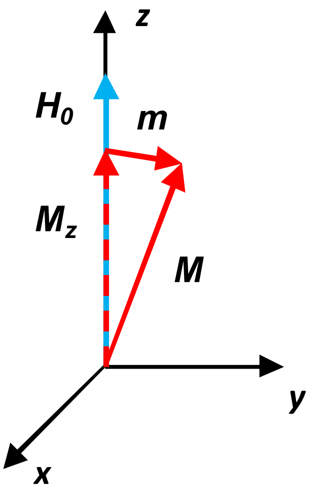

Fig. 2.2: Magnetization vector $\boldsymbol{M}$ decomposed into the static magnetization $\boldsymbol{M}_z$ parallel to the static magnetic field $\boldsymbol{H}_0$ and the dynamic magnetization $\boldsymbol{m}$ [31].

zation. In the simplest case $\boldsymbol{H}_{\text{eff}}$ only consists of the static magnetic field $\boldsymbol{H}_\mathbf{0}$. In the linear regime the dynamic component $\boldsymbol{m}$ (see Fig. 2.2) is considered to be small so that $M_\text{z} \approx M_\text{s}$. Here, the equation describes a uniform, right hand precession of the magnetization vector around the magnetic field vector (see Fig. 2.1) at a frequency of

$$\omega_0 = \gamma H_0. \tag{2.4}$$

To account for magnetic losses the LLE has to be extended by the phenomenological Gilbert term (Landau-Liftshifts-Gilbert equation, LLG 1955) [32, 33]

$$\frac{\partial \boldsymbol{M}}{\partial t} = -\gamma(\boldsymbol{M} \times \boldsymbol{H}_{\text{eff}}) + \frac{\alpha}{M_\text{s}}\left(\boldsymbol{M} \times \frac{\partial \boldsymbol{M}}{\partial t}\right) \tag{2.5}$$

with α as the Gilbert damping constant. This additional term exerts a torque towards the equilibrium orientation. For $\boldsymbol{H}_{\text{eff}} = \boldsymbol{H}_0$ this leads to a continuous reduction of the precession angle with time and finally the magnetization vector comes to rest parallel to the static magnetic field $\boldsymbol{H}_0$ (see Fig. 2.1).

Spin waves

So far we have only considered uniform precession of all magnetic moments around the static magnetic field. In this section this simple picture will be extended. By introducing phase shifts between the precession of neighboring spins, we can describe a wave of precession with frequency ω and wave vector k – a spin wave (see Fig.2.3). In this case, the terms $\boldsymbol{h}_{\mathrm{ex}}$ and $\boldsymbol{h}_{\mathrm{d}}$ from equation (2.3) are not zero anymore.

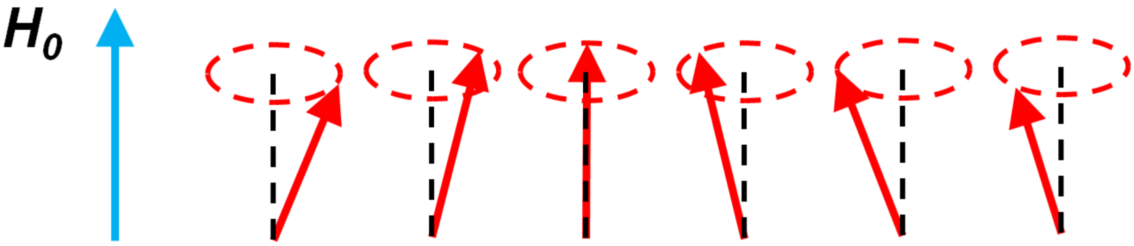

Fig. 2.3: Schematic view of a spin wave with the magnetic moments (red arrows) precessing around the orientation of the static magnetic field [31].

Exchange interaction The exchange interaction in a ferromagnet favors a parallel alignment of neighboring spins as it was first presented by Heisenberg (1928) [34] and is a purely quantum mechanical effect. Any deviation from parallel alignment therefore leads to an increment of energy and subsequently to a shift in the precession frequency. The exchange interaction is independent of the direction of spin-wave propagation and is therefore isotropic [6]. The exchange field $\boldsymbol{h}_{\mathrm{ex}}$ is a mean field approximation to this phenomenon and merely to be regarded as a mathematical construct. Its magnitude grows proportional with the squared wave vector k and therefore dominates spin-wave spectra for short wavelengths.

Dipolar interaction The dipolar interaction leads to a more complicated behavior than the exchange interaction. It originates in the interaction of a magnetic moment with the magnetic field of another magnetic moment [35]. In contrast to the exchange interaction the dipolar interaction is not limited to its next neighbor, but has a long range influence. Additionally, it is not isotropic leading to a strong dependence of the spin-wave behavior on the direction of the wave propagation [6]. For an unbound ferromagnet $\boldsymbol{h}_{\mathrm{d}}$ is independent of the magnitude of the wave vector, while for a confined geometry the dipolar interaction often dominates the shape of the spin-wave dispersion relation at low wave vectors, due to the presence of surfaces.

2.1 Spin waves in a confined geometry

Due to the influence of the dipolar interaction, the shape of a magnetic structure can have significant influence on the characteristics of a spin-wave spectrum. In analogy to electrostatics, the magnetic dipole moment can be regarded as a pair of effective magnetic charges [36] (see Fig. 2.4a)). Inside the structure for uniform or non-precessing magnetic moments these magnetic charges are fully compensated. Accordingly, there is no influence on an infinite ferromagnet. At the surface not parallel to the magnetization, on the other hand, uncompensated charges give rise to a demagnetizing field – a magnetic field that for an arbitrary shape of the magnetic structure can only be determined numerically. An example of a demagnetizing field in an ellipsoidal ferromagnet is shown in Fig. 2.4b). This phenomenon is referred to as shape anisotropy.

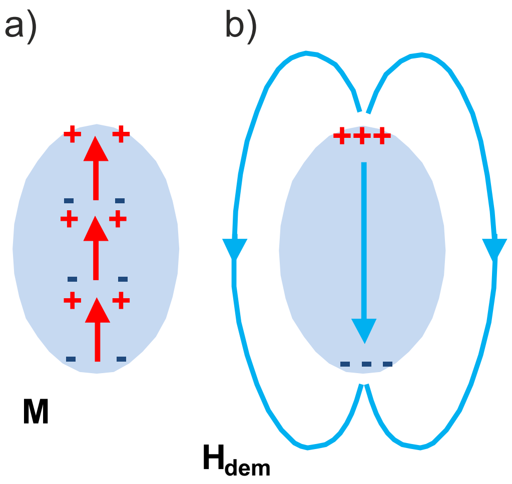

Fig. 2.4: a) Representation of magnetic dipoles as a combination magnetic charges in a finite ferromagnet. b) Uncompensated magnetic charges at surfaces not parallel to the magnetization form a demagnetizing field [31].

2.1.1 In-plane magnetized thin films

Mathematically, the influence of surfaces on spin waves was first described by Kittel (1948) [37] for ellipsoidal ferromagnets by defining demagnetizing factors that depend on the shape of the magnetic structure. By adding boundaries in one dimension, for example the z-axis, we receive an infinite film in the xy-plane. For an in-plane magnetized film (see Fig. 2.5a)) there is no static demagnetizing field, since the magnetization is parallel to the surface. Still, due to the precession of magnetic

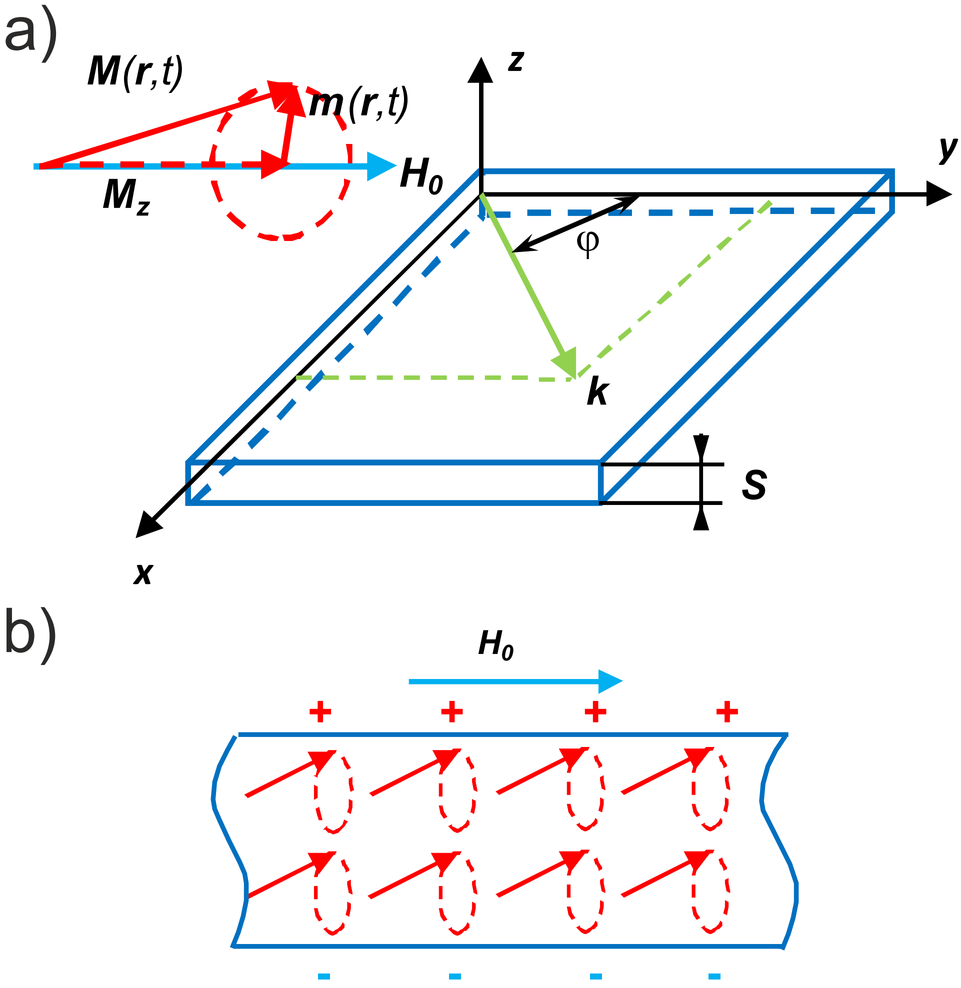

Fig. 2.5: a) In-plane magnetized film of thickness S b) Dynamic magnetic charges for a uniform precession in an in-plane magnetized film [31].

moments dynamic demagnetizing fields are formed (see Fig. 2.5b)) leading to a positive frequency shift of the uniform ($k = 0$) precession frequency. So equation (2.4) is altered to the Kittel equation for in-plane magnetized films

$$\omega_0 = \sqrt{\omega_{\mathrm{H}}(\omega_{\mathrm{H}} + \omega_{\mathrm{M}})} \tag{2.6}$$

with

$$\omega_{\mathrm{H}} = \gamma H_0 \qquad \text{and} \qquad \omega_{\mathrm{M}} = \gamma 4\pi M_0. \tag{2.7}$$

For spin waves with non-vanishing wave vector the calculations have to be extended.

While in an unbound ferromagnet the wave vector could take any value, it experiences a discretization along the confined axis (here the z-axis) and the in-plane wave vector k remains continuous. This phenomenon is called spin-wave quantization. In general this leads to the formation of resonances - so called thickness modes - with varying amplitudes along the thickness S of the film. These mode profiles depend on the magnitude as well as the orientation of the in-plane wave vector. Fortunately, this behavior only contributes in a significant way for thick films. In the experiments presented in chapter 4, all investigated structures can be regarded as ultrathin, meaning the thickness is small compared to the in-plane wave length ($kS \ll 1$). In this case the out-of-plane spin-wave profile can be assumed to be uniform and the two dimensional dispersion relation following the dipole-exchange theory by Kalinikos and Slavin [38] can be calculated:

$$\omega = \sqrt{(\omega_\mathrm{H} + \omega_\mathrm{M}(1 - P + qk^2)(\omega_\mathrm{H} + \omega_\mathrm{M} P \sin^2(\varphi) + qk^2)} \tag{2.8}$$

with

$$P = 1 - \frac{1}{kS}\Big[1 - \exp(-kS)\Big] \tag{2.9}$$

and φ as the angle between the static magnetic field $\boldsymbol{H}_0$ and the in-plane wave vector $\boldsymbol{k}$ (see Fig. 2.5a)) and q as the exchange stiffness. Spin waves propagating parallel to the magnetic field ($\varphi = 0°$) are called backward volume waves due to their negative group velocity. For $\varphi = 90°$ spin waves are referred to as Damon-Eshbach (DE) waves named after their first describers [39].
A graphical representation of a 2D spin-wave spectrum can be found in Fig. 2.6. Note that for simplicity in this picture only the dipolar interaction is considered ($q = 0$), which, for low wave vectors, is a valid approximation.

Spin-wave propagation in YIG

YIG is a ferrimagnetic dielectric with the following typical parameters [6]

- $M_0 = 1750\,\mathrm{G}$
- $\gamma/(2\pi) = 2.8\,\mathrm{MHz/Oe}$
- $q = 3.0 \times 10^{-12}\,\mathrm{cm}^2$

For the investigation of spin-wave dynamics in the low GHz regime the antiferromagnetic component can be neglected. Due to its insulating character all magnetic moments are localized. This enables the fantastically low Gilbert damping constant that can be as low as $\alpha = 5 \times 10^{-5}$ [6]. This value is unmatched by any other known material [40] allowing for spin-wave propagation lengths that can reach

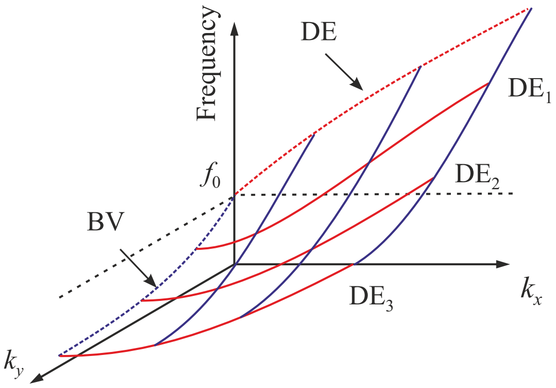

Fig. 2.6: Two dimensional dispersion relation (only dipolar interaction) of an in-plane magnetized film with the static magnetic field applied in x-direction [11].

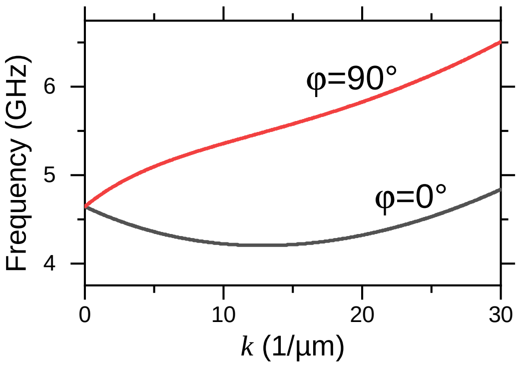

Fig. 2.7: Spectrum of an in-plane magnetized YIG film of thickness S=20 nm for a static magnetic field of 1000 Oe. φ denotes the angle between the static magnetic field and the in-plane wave vector k. Dipolar and exchange interaction are considered.

macroscopic distances. Additionally, the low magnetization facilitates the excitation of nonlinear phenomena, since a small dynamic magnetization $\boldsymbol{m}$ can lead to significant precession angles. YIG is therefore a highly promising candidate for applications [27, 28, 41–47]. An example spectrum for a 20 nm thin YIG film with the static magnetic field set to $H = 1000$ Oe, is shown in Fig. 2.7.

2.1.2 Spin-wave propagation in a waveguide

In this section, we will investigate the properties of spin waves in a stripe waveguide – a thin magnetic stripe – that can be used for directional signal guidance and is therefore of particular interest for applications.

Here, the waveguide is infinite in the x-direction and restricted along the y-axis (see Fig. 2.8). The finite width of the structure leads to the quantization of the wave vector in the y-direction k_y. For a waveguide magnetized perpendicular to its long axis fulfilling the condition $S \ll w$, with w as the width of the waveguide, spin waves form standing waves along the axis of confinement with zero amplitude at the edges (see Fig. 2.8). This type of boundary condition is called magnetic wall boundary and is caused by a pinning of the magnetic moments at the edges of the waveguide due to strongly non-uniform dipolar fields close to the edges [48] (see below). Accordingly, the wave number k_y^n is limited to

$$k_y^n = \frac{n\pi}{w} \quad \text{with} \quad n = 1, 2, \ldots \tag{2.10}$$

where n is the mode number [11]. For a transversely magnetized waveguide the spin-wave spectrum can be obtained by cutting the 2D surface at the allowed values for k_y^n (see the red lines in Fig. 2.6). By projecting the received curve into the $k_x\omega$-plane we see that all modes are located at frequencies below the Damon-Eshbach branch (DE) of the infinite film spectrum (see Fig. 2.9). This is reasonable, since an increasing mode number also increases the wave number parallel to the magnetic field leading to a frequency shift towards lower values (backward volume geometry).

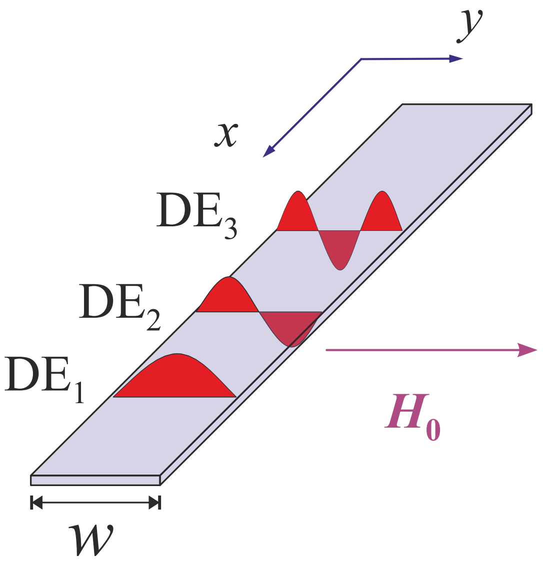

Fig. 2.8: Transversely magnetized waveguide of width w with the first 3 transversal mode profiles [11].

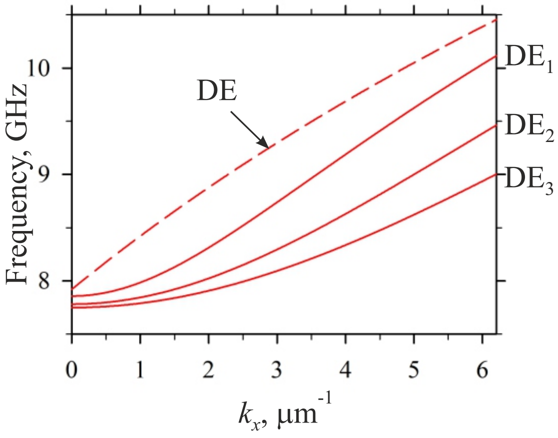

Fig. 2.9: Spectrum of propagating Damon-Eshbach modes in a transversely magnetized waveguide with the first 3 transversal spin-wave modes DE$_1$, DE$_2$ and DE$_3$ (solid lines) and the DE mode of an infinite film (dashed line) [11].

The internal magnetic field

It should be emphasized that the method described above is only a rough approximation to the spin-wave spectrum in a waveguide that delivers a good first impression of the system's properties.

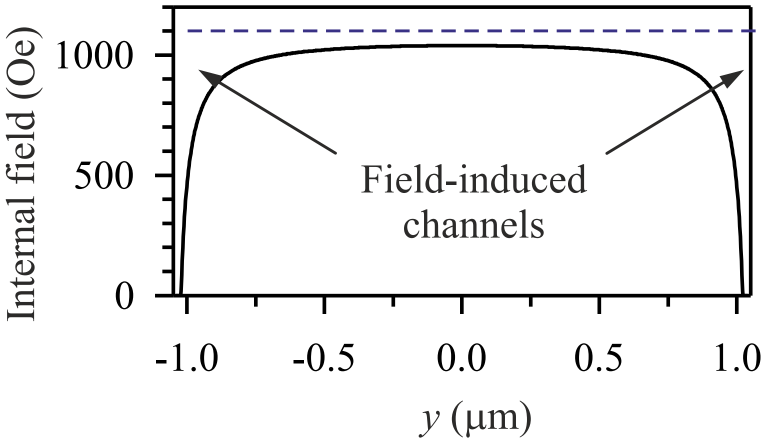

Fig. 2.10: Internal magnetic field of a transversely magnetized permalloy waveguide. The field induced channels enable the propagation of edge modes [11].

To gain a deeper understanding of spin waves in a waveguide we have to take a closer look at the internal magnetic field. Due to the finite width of the examined structure, the internal magnetic field is non-uniform caused by demagnetizing effects. While the influence around the center of the structure is limited, the demagnetizing field gives rise to significant changes at the edges (see Fig. 2.10). The internal field is given by [11]

$$H(x) = H_0 - \frac{4\pi M_0}{\pi}\left[\arctan\left(\frac{S}{2x+w}\right) - \arctan\left(\frac{S}{2x-w}\right)\right]. \tag{2.11}$$

Center and edge modes In a transversely magnetized waveguide two types of modes have to be considered: The center and the edge modes [11]. Following their names, it is evident that the center modes show most pronounced amplitudes of the dynamic magnetization at the center of the waveguide. Since the deviation of the static magnetic field from the externally applied field H_0 around the center is not very large, the approximation of quantized wave vectors (equation (2.10)) to determine the precession frequency is still a good estimation. The wave vector on the other hand has to be taken with care, since a real wave vector cannot be defined in a non-uniform environment.

Regions close to the edge show a different behavior. Here, the magnetic field is strongly reduced leading to the formation of field-induced channels. These channels give rise to localization of spin-waves at the edges of the waveguide. These modes are called edge modes and have no analogue in an infinite film. Due to the reduced magnetic field, edge modes oscillate at lower frequencies. An example of the spatial distribution of center and edge modes is shown in Fig. 2.11 and 2.12.

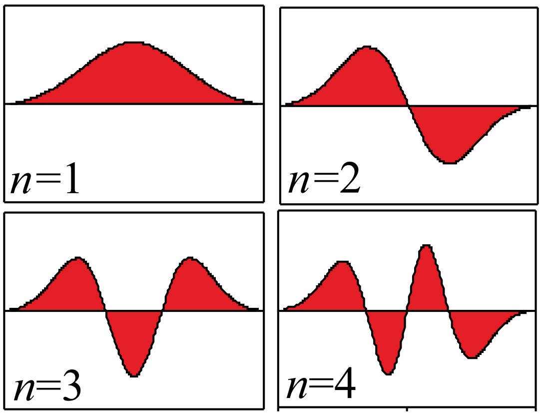

Fig. 2.11: Transversal spin-wave profiles of the first 4 centre modes in a transversely magnetized waveguide [31].

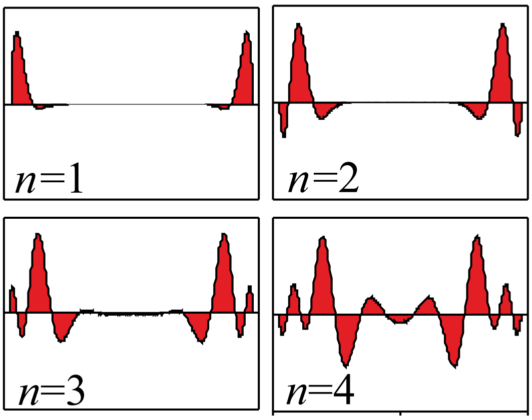

Fig. 2.12: Transversal spin-wave profiles of the first 4 edge modes in a transversely magnetized waveguide [31].

2.2 Excitation of spin waves

There are many possible ways to excite spin waves of which we will focus on the three methods relevant for this thesis: The excitation of spin-waves by dynamic magnetic fields, the excitation by spin-orbit torques and the excitation by thermal gradients.

2.2.1 Excitation of spin waves by dynamic magnetic fields

The excitation of spin waves by an external dynamic magnetic field is based on the dipolar interaction of the excitation field with the magnetic moments of the ferromagnet. As shown in equation (2.3) the effective magnetic field can contain a dynamic magnetic field $\boldsymbol{h}_{\text{dyn}}$. For excitation fields that are small compared to the static magnetic field ($\boldsymbol{h}_{\text{dyn}} \ll \boldsymbol{H}_0$, linear regime) calculations show that only dynamic magnetic field components that are oriented perpendicular to the static magnetic field $\boldsymbol{H}_0$ contribute to the excitation of spin precession (see Fig. 2.13). In case of a periodic excitation field ($\boldsymbol{h}_{\text{dyn}} \propto \exp(i\omega t)$) the response of the magnetic system can be noted as follows [6]:

$$\boldsymbol{m} = \chi \boldsymbol{h}_{\text{dyn}}. \tag{2.12}$$

Here, $\boldsymbol{m}$ is the dynamic magnetization with $(\boldsymbol{m} \ll \boldsymbol{M})$ and χ is the dynamic susceptibility tensor. The tensors components resonantly depend on the excitation frequency ω for a fixed static magnetic field $\boldsymbol{H}_0$ and vice versa.
In case of a uniform excitation field the magnetic moments precess uniformly ($k = 0$) around the static magnetic field axis. If the system is driven at the resonance frequency the excitation reaches maximum efficiency and is referred to as ferromagnetic resonance (FMR).
For a local dynamic field only magnetic moments in the vicinity of the point of excitation are excited at the driving frequency. Due to the dipolar and exchange interaction between spins, energy is transferred to the surrounding magnetic moments. These spins start precessing at the excitation frequency with a phase shift with respect to their neighbors. This way, a propagating spin wave with $k \neq 0$ is excited.
In the following we will take a closer look at the local excitation of spin waves by the inductive field of a stripline antenna.

Inductive excitation of spin waves

The transmission of a microwave-frequency current through an antenna induces a dynamic magnetic field $\boldsymbol{h}_{\mathrm{dyn}}$ that couples to the magnetic moments as described above. The coupling efficiency depends on the overlap of the dynamic magnetic field with the dynamic magnetization profile of the excited spin wave (see Fig. 2.13). In the given setup of a transversely magnetized stripe waveguide, only the dynamic field components h_x and h_z are perpendicular to the static magnetic field and can therefore contribute to an excitation of spin waves (linear approximation). Additionally, h_z can be assumed to be of negligible influence due to the strong out-of-plane demagnetizing field for thin magnetic layers, so in good approximation only the x-component has to be considered. The transversal profile of centre modes can be estimated by a sine-function

$$m_x^n(y) \;\propto \sin\left(k_y^n(y + w/2)\right) \tag{2.13}$$

where k_y^n is the transversal wave vector (see equation (2.10)). A graphical presentation can be seen in Fig. 2.13. The x-dependence of the dynamic magnetization $m_x^n(x)$ is determined by a propagating spin wave and is therefore periodic:

$$m_x^n(x) \;\propto \exp(-ik_x^n x) \tag{2.14}$$

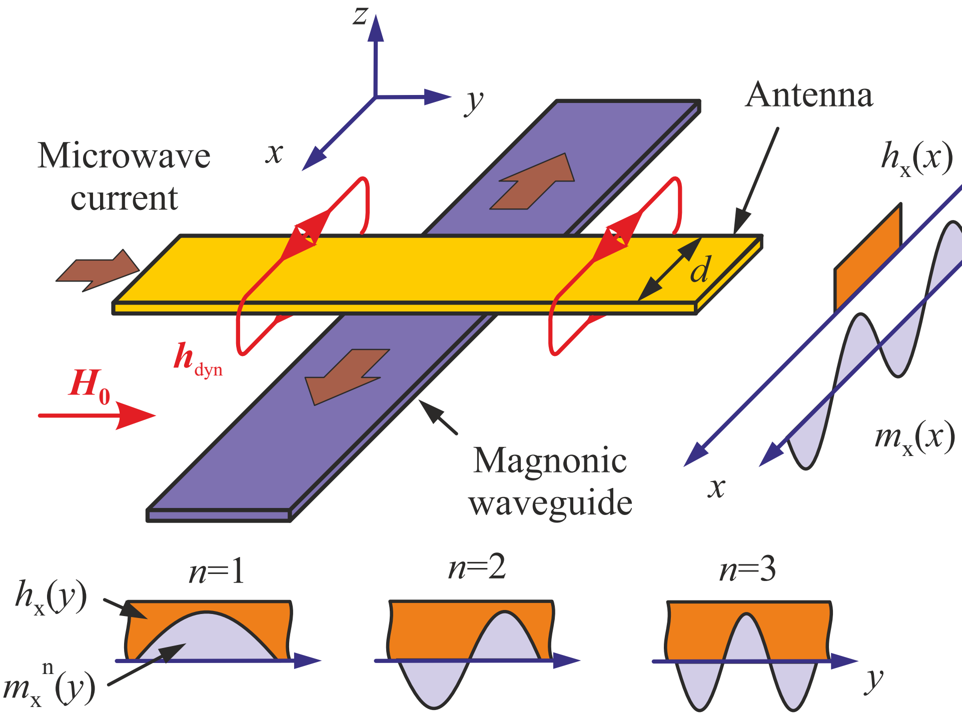

Fig. 2.13: Schematic presentation of the inductive excitation of spin waves in a waveguide with an antenna. Inset: x- and y-profiles of the dynamic magnetization $\boldsymbol{m}$ of different spin-wave modes and the excitation field $\boldsymbol{h}_{\text{dyn}}$ [11].

Following the calculations for the amplitude of the excited mode A_n in [10] we get

$$A_n \propto \left| \int\limits_{-w/2}^{w/2} h_x(y) m_x^n(y) dy \right| \cdot \left| \int\limits_{\infty}^{\infty} h_x(x) m_x^n(x) dx \right|. \tag{2.15}$$

In a first approximation, the dynamic magnetic field can be assumed to be uniform below the antenna and zero for every other location, so we get

$$A_n \ \propto \frac{1-(-1^n)}{n} \frac{|\sin(k_x^n d/2)|}{k_x^n} \tag{2.16}$$

where d is the width of the antenna. We see that only modes with an uneven values of n can be excited by the inductive field of an antenna. Additionally, the excitation efficiency follows a sinc function in dependence of the longitudinal wave vector k_x^n.

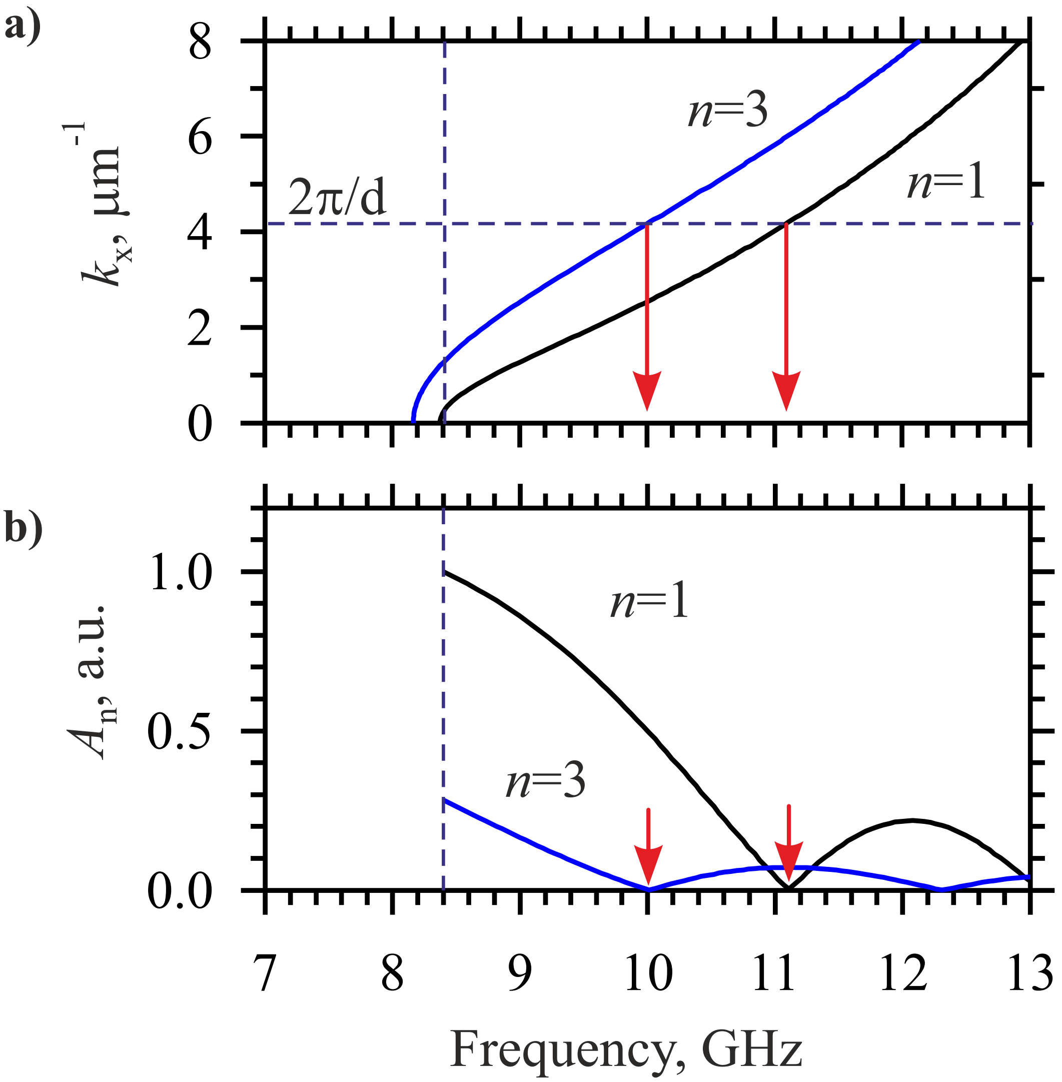

Fig. 2.14: a) Dispersion relation of a 2 µm wide permalloy waveguide of thickness 36 nm with a static magnetic field of 900 Oe. b) Frequency dependence of the excited spin-wave amplitude of the transversal modes for $n = 1$ and $n = 3$ [11].

Using equation (2.8) for centre modes (equation (2.10)), we can determine the frequency dependence of the spin-wave amplitude A_n (see Fig. 2.14b)).
From this analysis we see that short wave length spin waves, corresponding to higher precession frequencies, can only be excited with very narrow antennae. Unfortunately, this leads to microwave impedance matching problems and accordingly increases microwave losses and is therefore not helping to improve the excitation

efficiency.
In the following section, we will explore a possibility to excite spin waves by direct currents. Due to the absence of microwave currents this technique does not encounter problems like impedance matching or limited coupling efficiency between the excitation field and the dynamic magnetization.

2.2.2 Excitation of spin waves by spin-orbit torques (SOT)

The excitation of spin waves by spin-orbit torques (SOT) is a threefold process (see Fig. 2.15): Creating a pure spin current by making use of the interaction between the electron spin and its orbital angular moment, then transferring the spin current into the magnetic system and finally the transfer of angular momentum from the spin current into the magnetic system via the exchange interaction (spin transfer torque (STT)). Depending on the examined structure some of these processes can occur simultaneously.

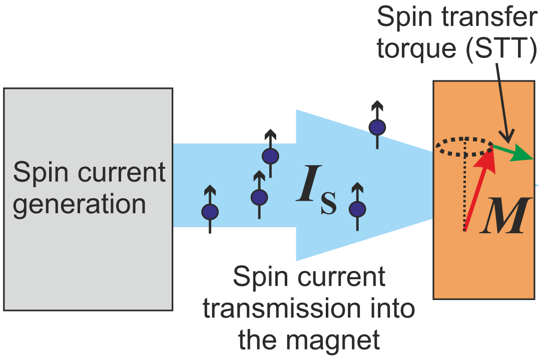

Fig. 2.15: Schematic of the excitation of spin waves by spin-orbit torques (SOT). Step 1: Generation of a pure spin current by spin-orbit interaction. Step 2: Transmission of the spin current into the magnet. Step 3: Transfer of angular momentum to the magnetic system by spin-transfer torques (STT).

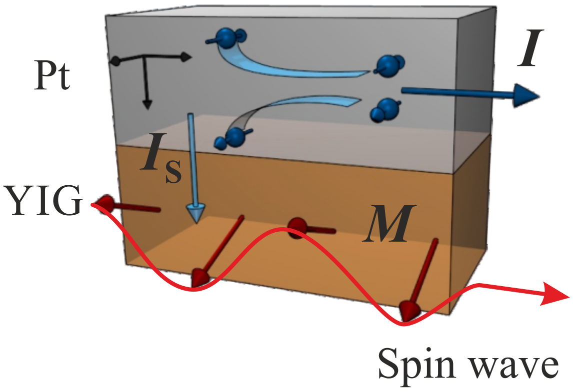

Fig. 2.16: Schematic of the spin orbit torques in a YIG/Pt bilayer. An electric current I in the Pt layer is converted into a pure spin current I_S by spin-orbit coupling (spin-Hall effect). I_S is injected into the YIG layer and excites spin waves by the spin-transfer torque [44].

Spin-Hall effect

The spin-Hall effect is a scattering process based on spin-orbit coupling that connects the orientation of the spin with its orbital angular momentum. The origin of this can be both internally, for example due to band structure configurations of the material, and externally - due to skew scattering at impurities [16]. The effect manifests in the following form:

Transmitting an unpolarized, electric, direct current I with a current density $\boldsymbol{j}$ through a material with spin-orbit coupling - i.e. platinum (Pt) - leads to a spin dependent scattering of the electrons (see Fig. 2.16). This behavior causes the formation of pure spin currents I_s – with a spin current density $\boldsymbol{j}_\mathrm{s}$ flowing perpendicular to the charge current density ($\boldsymbol{j} \perp \boldsymbol{j}_\mathrm{s}$) – that create spin accumulations at the boundaries of the conductor. The polarization $\boldsymbol{\sigma}$ of the spin current can be determined from the direction of the spin and charge current. In a bilayer structure consisting of a metal with strong spin-orbit coupling and a magnet only the spin current direction normal to the interface towards the magnetic layer has to be considered (here the $\boldsymbol{z}$-axis). The corresponding polarization is given by [49]

$$\boldsymbol{\sigma} = \boldsymbol{z} \times \frac{\boldsymbol{j}}{j}. \tag{2.17}$$

It is to be mentioned that in a magnet/normal metal bilayer a reverse process appears as well. The precession of spins in the magnet leads to a transfer of angular momentum to the normal metal [50, 51]. This process is called spin-pumping. By means of the spin-Hall effect this spin current is transformed into an electric current perpendicular to direction of the spin current flow, referred to as the inverse spin-Hall effect [50]. Since this process presents an additional relaxation channel for spin waves, it significantly increases the natural damping of the system [28, 51].

Spin transfer torque (STT)

In a normal metal/magnet bilayer the spin current created by the spin-Hall effect can diffuse into the magnetic layer, where it exerts a torque on the magnetization. This process is called spin transfer torque since it is based on the transfer of angular momentum from the spin current to the magnetic system. While for a metallic magnet the electrons diffuse into the magnetic layer, this is not possible for an insulating magnet. In the latter case a spin accumulation is created at the interface making SOT for a normal metal/insulating ferromagnet bilayer structures a purely interfacial process. Mathematically the spin transfer torque can be described by an additional torque τ_STT, the Slonczewski torque, acting on the magnetization in the

LLG equation [6,12]:

$$\frac{\partial \boldsymbol{M}}{\partial t} = -\gamma(\boldsymbol{M} \times \boldsymbol{H}_{\text{eff}}) + \frac{\alpha}{M_0}\left(\boldsymbol{M} \times \frac{\partial \boldsymbol{M}}{\partial t}\right) - \frac{\beta}{M_0}\left[\boldsymbol{M} \times (\boldsymbol{M} \times \boldsymbol{\sigma})\right] \tag{2.18}$$

with

$$\beta = I\frac{\varepsilon g \mu_B}{2eM_0AS}. \tag{2.19}$$

where ε is the spin polarization efficiency, g is the Landé-factor, μ_B is Bohr's magneton, e is the elemental charge and A is the area of spin current injection (interface). While this equation was originally developed to describe the interaction between a spin polarized current and a ferromagnet, it also holds for the behavior of pure spin currents, since only the transfer of angular momentum is considered [12]. Therefore, it is still applicable for magnetic insulators like YIG. Inserting (2.17) into (2.18) reveals a sinusoidal dependence of the STT magnitude on the angle between the electric current and magnetization, which, for small spin-wave amplitudes, is parallel to the static magnetic field. Accordingly, the influence of SOT is maximized in case of perpendicular orientation between $\boldsymbol{I}$ and $\boldsymbol{H}_0$ as was first experimentally demonstrated by Kimura et.al. in 2007 [52]. This setup is called spin-Hall geometry. For the described geometry it can be seen in Fig. 2.17 that the Slonczewski torque is either oriented parallel or antiparallel to the Gilbert torque that, for a fixed orientation of the static magnetic field, depends on the orientation of the electric current. This characteristic allows for interesting new applications. A torque, that is aligned parallel to the Gilbert torque leads to an effective amplification of the system's natural damping and to a suppression of magnetization precession.

A reversal of the electric current orientation creates a more complex situation. Here, the Slonczewski torque is oriented antiparallel to the Gilbert torque and therefore compensates the dissipation, acting as a "negative damping" driving the magnetic system out of thermal equilibrium. This can lead to a variety of phenomena like magnetization switching [53] or the amplification of magnetic fluctuations [17,18]. For a properly chosen current density and system design the natural damping can be fully compensated and the magnetic system enters the auto-oscillation regime [19–22,27,43,44,47,54,55], as described in the following section.

Auto-oscillations

In the following we will examine the current dependence of the magnetization precession in the weakly nonlinear regime. By introducing the dimensionless, complex

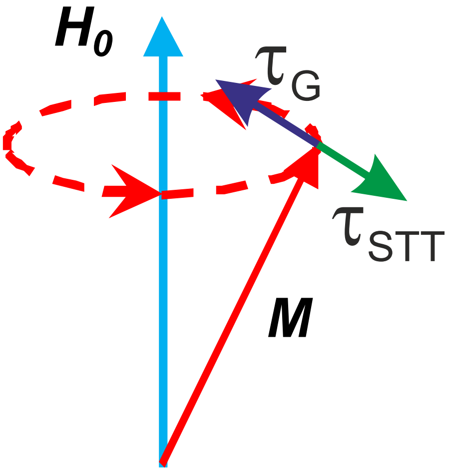

Fig. 2.17: Schematic view of the Gilbert torque $\boldsymbol{\tau}_{\mathrm{G}}$ and the Slonczewski torque $\boldsymbol{\tau}_{\mathrm{STT}}$ acting on the magnetization $\boldsymbol{M}$ with opposite signs. $\boldsymbol{\tau}_{\mathrm{STT}}$ can be considered an effective "negative damping".

amplitude

$$c = \frac{M_x - iM_y}{\sqrt{2M_0(M_0 + M_z)}}, \tag{2.20}$$

with physical meaning only for $|c| < 1$, the Landau-Lifshitz-Gilbert-Slonczewski equation can be rewritten in the universal form of an auto-oscillator [54]:

$$\underbrace{\frac{\mathrm{d}c}{dt} + i\omega(|c^2|)c}_{\text{conservative motion}} + \underbrace{\Gamma_+(|c^2|)c}_{\text{Gilbert damping}} - \underbrace{\Gamma_-(|c^2|)c}_{\text{STT}} = \underbrace{f(t)}_{\text{external force}} . \tag{2.21}$$

The external force $f(t)$ represents influences like thermal fluctuations. While this equation is only fully correct for an out-of-plane magnetized nanopillar [54], it is still approximately correct for arbitrary field directions and other geometries [56]. With the power $p = |c|^2$ the oscillation frequency is given by

$$\omega(p) \approx \omega(p = 0) + Np \tag{2.22}$$

with N as the nonlinear frequency shift that depending on the spin-wave geometry and magnetic properties of the system can be positive or negative. For the Gilbert term we obtain

$$\Gamma_+(p) \approx \omega_{\mathrm{r}}(1 + Qp) \tag{2.23}$$

where Q is a measure for the development of the Gilbert damping with the spin-wave intensity and ω_r is the relaxation frequency. The Gilbert term is always positive and therefore leads to a reduction of p with time. The Slonczewski term is given by

$$\Gamma_-(p) \approx \beta I(1-p) \tag{2.24}$$

with β as a proportionality constant. It can be positive or negative, depending on the direction of the electric current. For a positive I the Slonczewski torque can compensate the Gilbert torque. It can be shown that $p = 0$ is a stable solution for the system as long as $\Gamma_-(0) < \Gamma_+(0)$, while it is instable for $\Gamma_-(0) > \Gamma_+(0)$. Accordingly, $\Gamma_-(0) = \Gamma_+(0)$ defines the threshold for the transition of the system into the auto-oscillation regime. The corresponding current I_c is called critical or threshold current. Calculations reveal that the inverse average power $1/\overline{p}$ linearly decreases with the electric current for currents below I_c

$$\frac{1}{\overline{p}} \sim (I_\mathrm{c} - I). \tag{2.25}$$

Accordingly, I_c can be determined by a linear fit to the current dependence of the inverse average power. The intersect of the corresponding line with the current axis then defines the onset of the auto-oscillation regime. At this point, the equation loses its validity, since the system cannot be regarded as weakly nonlinear anymore and would require an infinite average power.

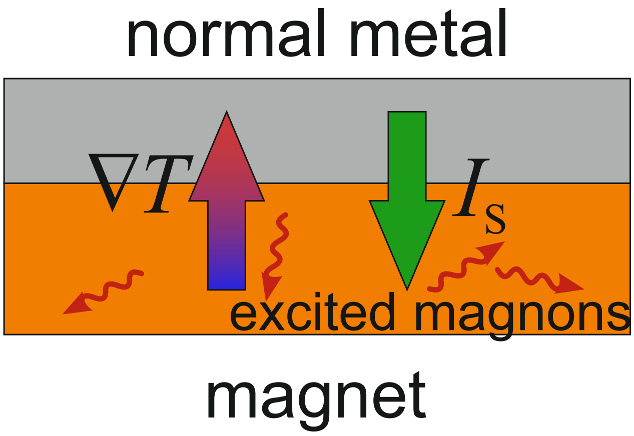

Fig. 2.18: A schematic view of the spin-Seebeck effect for an increased temperature of the normal metal with respect to the magnet. The displayed spin current orientation leads to the excitation of magnons.

2.2.3 Excitation of spin waves by thermal gradients

Another mechanism to excite spin waves makes use of thermal gradients. In a bilayer consisting of a normal metal and a magnet, a thermal gradient can lead to a spin accumulation at the interface and consequently to a spin current through the boundary. This phenomenon is called spin-Seebeck effect and was first experimentally demonstrated by Uchida et.al. [57] in 2008. It is to be mentioned that the original interpretation could not be confirmed by later investigations, since a different length scale of the effect would be required (see for example [58]). An alternate theoretical model was presented by Xiao et.al. [59]. Here, the electron temperature in the normal metal and the magnon temperature in the magnetic layer (represented by the magnon population at the interface) are calculated. The theory predicts the formation of a spin current through the interface in presence of a thermal gradient oriented parallel to the interface normal. In case of an enhanced normal metal temperature with respect to the magnet (see Fig. 2.18), this spin current leads to a flow of angular momentum from the normal metal into the magnet, where spin waves can be amplified and excited by means of the spin transfer torque.

The thermal gradient can be provided, for example, by an electric current in the normal metal layer (Joule heating). Since the heating power is proportional to I^2, the strength of the current driven spin-Seebeck effect is independent of the orientation of the electric current.

3 Methods

3.1 Brillouin light scattering

Brillouin light scattering (BLS) is a powerful tool to examine spin waves. Its extremely high sensitivity [60], that even allows for the detection of low intensity thermal spin waves, combined with its high spatial, temporal and sufficient frequency resolution [61] enables a broad spectrum of applications. The concept of BLS is based on the interaction of magnetization dynamics in magnetic materials with an incident photon. In a quantum mechanical representation this process can be regarded as an inelastic scattering of a photon by a magnon - the particle representation of a spin wave. Analogue to Raman scattering of photons from phonons [62] two mechanisms have to be considered here:

1. Magnon creation: Excitation of a magnon by the incident photon, Stokes process (see Fig. 3.1)
2. Magnon annihilation: Absorption of an existing magnon by the incident photon, anti-Stokes process (see Fig. 3.2)

Both processes obey the energy and - for properly chosen magnetic structures [60] - the momentum conservation law. Accordingly for the magnon creation process, the energy and therefore the frequency of the incident photon $\omega_\mathrm{p}^\mathrm{in}$, is reduced to $\omega_\mathrm{p}^\mathrm{out}$ since part of the photons energy is transferred to the new magnon. Also the momentum and therefore the wave vector $\boldsymbol{k}_\mathrm{p}^\mathrm{in}$ is altered to $\boldsymbol{k}_\mathrm{p}^\mathrm{out}$:

$$\hbar\omega_\mathrm{p}^\mathrm{out} = \hbar(\omega_\mathrm{p}^\mathrm{in} - \omega_\mathrm{M}) \tag{3.1}$$

$$\hbar\boldsymbol{k}_\mathrm{p}^\mathrm{out} = \hbar(\boldsymbol{k}_\mathrm{p}^\mathrm{in} - \boldsymbol{k}_\mathrm{M}) \tag{3.2}$$

where ω_M and $\boldsymbol{k}_\mathrm{M}$ are the frequency and the wave vector of the spin wave. For magnon annihilation, the energy is increased:

$$\hbar\omega_\mathrm{p}^\mathrm{out} = \hbar(\omega_\mathrm{p}^\mathrm{in} + \omega_\mathrm{M}) \tag{3.3}$$

$$\hbar\boldsymbol{k}_\mathrm{p}^\mathrm{out} = \hbar(\boldsymbol{k}_\mathrm{p}^\mathrm{in} + \boldsymbol{k}_\mathrm{M}) \tag{3.4}$$

In a classical picture, the process is mediated by magneto-optical effects, since spin waves create dynamic fluctuations in the dielectric permittivity tensor. These fluctuations form a phase grating that is propagating with the phase velocity of the spin

wave. Due to Bragg-reflection and a Doppler-shift of the incident light, the wave vector and frequency of the scattered light are modified as described above [60]. Since mainly the off-diagonal components of the tensor are responsible for the scattering process (Faraday-effect, magnetic birefringence effects) the polarization of the reflected light is rotated by 90° with respect to the incident light polarization [63]. At room temperature both processes – annihilation and creation – are of comparable probability, if magnons with frequencies below 1 THz are considered [60]. It can be shown that the scattering cross section and accordingly the intensity of the inelastically scattered light is proportional to the squared dynamic magnetization $\boldsymbol{m}^2$ and therefore proportional to the spin-wave intensity in both cases [64].
In the following, we will take a closer look at the experimental setup used to examine spin waves by BLS.

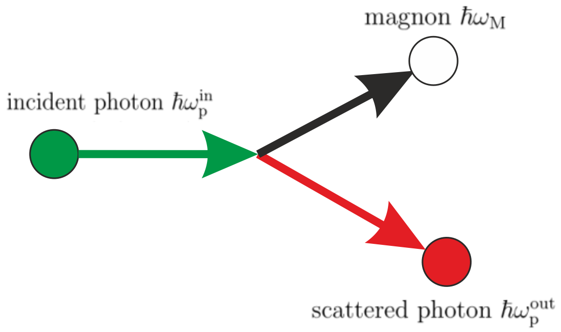

Fig. 3.1: Magnon creation: Excitation of a magnon of energy $\hbar\omega_{\mathrm{M}}$ by an incident photon of energy $\hbar\omega_{\mathrm{p}}^{\mathrm{in}}$ resulting in a scattered photon of energy $\hbar\omega_{\mathrm{p}}^{\mathrm{out}}$ and a magnon.

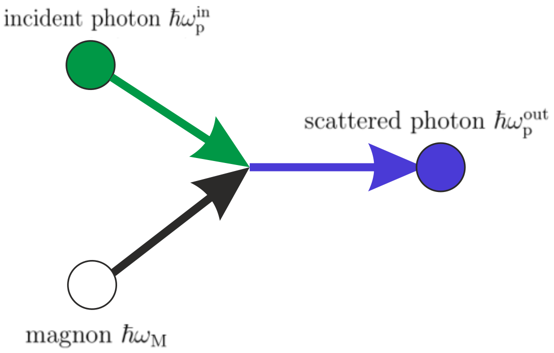

Fig. 3.2: Magnon annihilation: Absorption of a magnon of energy $\hbar\omega_{\mathrm{M}}$ by an incident photon of energy $\hbar\omega_{\mathrm{p}}^{\mathrm{in}}$ resulting in a scattered photon of energy $\hbar\omega_{\mathrm{p}}^{\mathrm{out}}$.

3.1.1 Micro-focus Brillouin light scattering setup

A micro-focus BLS setup (μBLS) combines the high sensitivity of Brillouin light scattering to even low intensity spin waves with submicrometer spatial resolution as it was first demonstrated in [65]. A schematic of the setup is shown in Fig. 3.3. To be able to achieve high spatial resolution with a sufficient frequency resolution several requirements are needed of which the main aspects shall be discussed here briefly [61]:

- A monochromatic light
- A single spatial mode of the incident light
- High degree of polarization of the incident light

Laser and focusing optics

To locally investigate a magnetic structure the incident light is focused into a diffraction limited spot. To achieve maximum spatial and frequency resolution the source has to be monochromatic, since a sufficient frequency resolution of the observed spin waves can only be achieved by using monochromatic incident light to extract the frequency difference between the incident and the scattered light. To fulfill this requirement, a diode-pumped solid state cw laser with a wavelength of 473 nm – blue light – and a linewidth of below 10 MHz is used[1], if not mentioned differently.

Additionally, to a monochromatic light source a single spatial mode is needed to be able to focus the laser beam into a diffraction limited spot. Deviations from this condition, leads to a broadening or deformation of the focal spot. To receive a single spatial mode, the primary laser beam is expanded by a beam expander and then spatially filtered with a pin hole aperture. The resulting spatial mode is the TEM_{00} that is reflected through an objective lens and focused onto the analyzed structure. The utilized objective lens[2] with a numerical aperture of 0.85 and a magnification x100 enables a focal diameter of down to 250 nm. The objective lens can be used the focus a laser beam through a transparent substrate – in the experiments presented in chapter 4 it is always Gadolinium Gallium Garnet (GGG).

Separation of elastically and inelastically scattered light

Since the elastically scattered light (elastic light) exceeds the intensity of the inelastically scattered light (inelastic light) by several orders of magnitude, an efficient

---

[1] EXLSR-473-50-CDRH by Spectra Physics

[2] LCPLFLN-LCD by Olympus

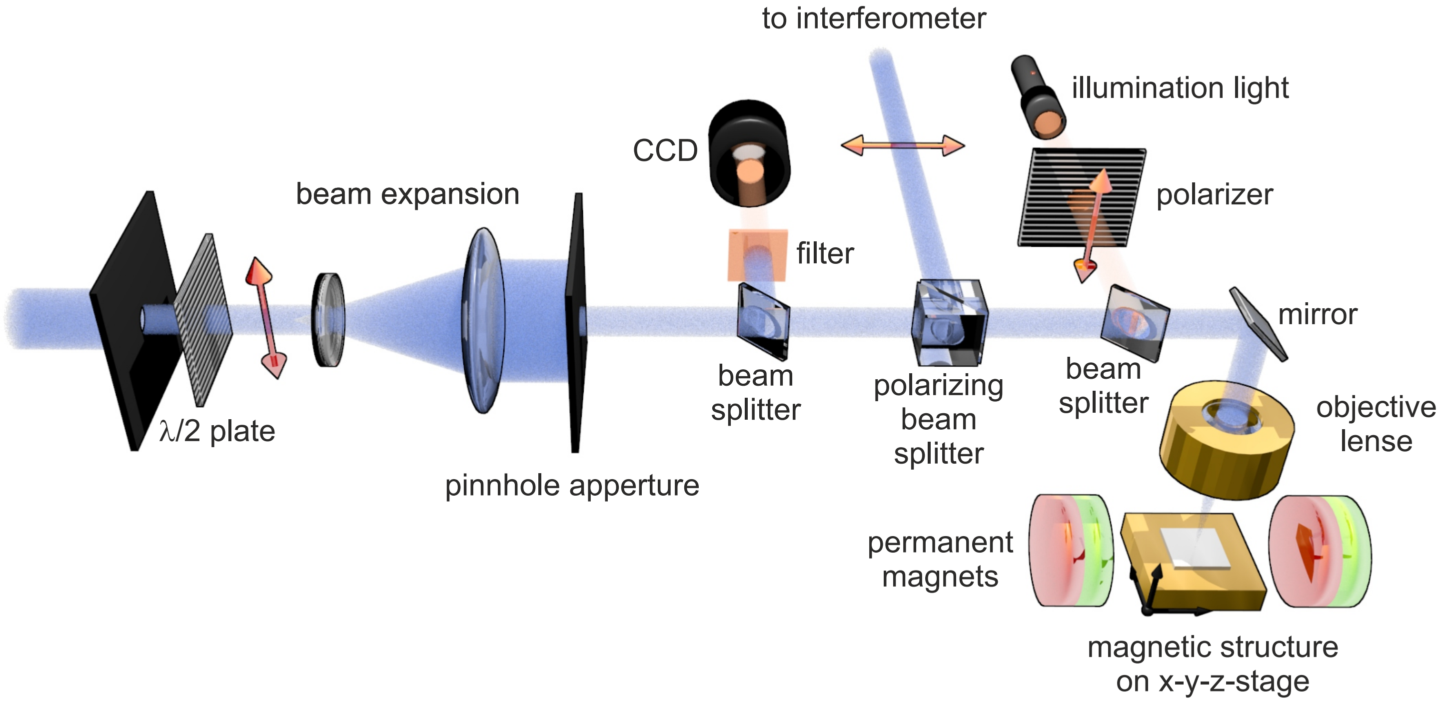

Fig. 3.3: Schematic view of a micro-focus Brillouin light scattering setup [66].

separation mechanism is needed to achieve a reasonable signal to noise ratio. The main discrimination mechanism is based on the frequency filtering using a Fabry Perot interferometer (s. below). However, to further increase the sensitivity of the setup, we make use of the polarization rotation by 90° of the inelastic light with respect to the incident light. For the elastic scattering process the polarization is conserved. To separate both parts, a $\lambda/2$ wave-plate is inserted into the beam path setting the polarization direction of the incident laser beam. This way the light reflected from the magnetic structure can be separated into beams of different polarization by a polarizing beam splitter. The inelastically scattered light is guided to the interferometer for further processing.

Positioning and scanning of the magnetic structure

To properly study the dynamics in magnetic structures of submicrometer dimensions precise positioning is of high importance. Therefore, the sample is mounted on a xyz piezoelectric stage with a positioning precision of about 50 nm. To illuminate and monitor the sample a CCD camera and an orange light source are integrated into the light path (see Fig. 3.3). The orange light is polarized to enable separation of the illumination light from the inelastically scattered laser light. The reflected orange light is guided through a filter into the CCD camera. The filter is needed to avoid overexposure of the camera due to elastically reflected laser light. While this setup also can be used with a white light illumination, orange light allows for an improved filtering of the illumination and the laser light due to a better frequency separation.
Additionally, to precise positioning of the sample, the monitoring setup – based on an image recognition software – is used to compensate for thermally induced spatial drift of the examined structure. This way it can be assured that the laser spot is focused on the same part of the examined structure for the duration of the measurements.

The piezoelectric stage also provides the possibility to measure power maps $P(\omega, \boldsymbol{r})$ of the dynamic magnetization, revealing the spatial distribution of the spin-wave intensity. Therefore 1D or 2D rastering with the focused laser spot of the magnetic structure can be performed. The spatial resolution of this mapping equals the diameter of the laser spot (≈ 250 nm), while the frequency resolution is limited by the interferometer (see section 3.1.2).

μBLS measurements with temporal resolution

In addition to spatially resolved measurement, investigations using temporal resolution can be performed [60]. In the experiments presented in section 4.4, this is achieved by using a time correlated single-photon counting method, similar to time-of-flight experiments performed in mass spectrometry or in particle physics. Therefore, the electric current used to exert spin-orbit torques on the magnetic system, is applied in pulses, leading to the formation of a pulsed spin-wave signal. The current pulse is also used as a starting signal of a 32 bit reference counter. At the position of the laser spot, the probing light is inelastically scattered from magnetization oscillations, then passes through the interferometer (see section 3.1.2) and is detected by a single photon detector[3]. The detected photon is used as a stop signal for the counter. This setup allows for the detection of about 10^6 events per second with a temporal resolution that, for properly chosen conditions, can be as low as 1 ns.

The static magnetic field

To magnetize the sample in the desired orientation, permanent magnets are used that allow for magnetic fields between 150 Oe and 2000 Oe. Although different configurations are possible, in the experiments presented in chapter 4 only in-plane magnetic fields are used.

3.1.2 Tandem Fabry Perot interferometer

The inelastically scattered light is sent into the 6-pass Tandem Fabry Perot interferometer (TFPI)[4]. The TFPI is based on two Fabry Perot interferometers (FPI, two coplanar mirror pairs) with non parallel optical axis'. Each interferometer pair is a bandpass filter with the transmission depending on the distance between mirrors d and the wavelength λ of the examined light. At $d = \lambda/2$ maximum transmission is achieved:

$$\mathcal{T}(d,\lambda) = \frac{1}{1 + \frac{4\mathcal{F}^2}{\pi^2}\sin^2\left(\frac{2\pi d}{\lambda}\right)} \tag{3.5}$$

with $\mathcal{F}$ being the finesse that is determined by the quality and reflectivity of the mirrors. The finesse can be determined from the width of the bandpass $\delta\lambda$ as follows

$$\mathcal{F} = \frac{\delta\lambda}{\lambda}. \tag{3.6}$$

To receive transmission for both FPI simultaneously for each interferometer one mirror is mounted on the same moving stage. The advantage of this configuration compared to a single FPI is the improved contrast $\mathcal{C}$ between the maximum intensity I_{max} and the minimum intensity I_{min} of the transmitted light. For a single FPI it is

---

[3] Single photon counting module, COUNT BLUE-10B by Laser Components

[4] Tandem Interferometer TFP-1 by JRS Scientific Instruments

given by

$$\mathcal{C}_{\mathrm{FPI}} = \frac{I_{\mathrm{max}}}{I_{\mathrm{min}}} = 1 + \frac{4\mathcal{F}^2}{\pi^2}. \tag{3.7}$$

In the TFPI this contrast is strongly improved by a 6 pass configuration (3 for each mirror pair), since the contrast scales with the power of the number of passes and is therefore proportional to $\mathcal{F}^{12}$

$$\mathcal{C}_{\mathrm{TFPI}} \propto \mathcal{C}_{\mathrm{FPI}}^{6} \propto \mathcal{F}^{12}. \tag{3.8}$$

This strong separation is needed, since the elastic light intensity exceeds the intensity of the inelastic light by several orders of magnitude.

The transmitted light is detected by a semiconductor detector. Since the detected signal equals the convolution of the spin-wave spectrum and the instrumental response function the maximum frequency resolution is limited to 50 MHz, which is sufficient for the experiments performed in chapter 4.

3.2 Micromagnetic simulations

To support the interpretation of the experimental data presented in chapter 4, often micromagnetic simulation are used. These simulations are performed using the GPU-accelerated program MuMaX3 [67]. In MuMax the magnetization is regarded as a continuum field $\boldsymbol{M}(\boldsymbol{r}, t)$ and then discretizes magnetic samples into orthorhombic finite difference cells of equal size and of individual uniform magnetization [67, 68]. To examine the dynamic behavior of each cell, the Landau-Lifshitz equation is integrated in discrete time steps. This way, real and effective fields are determined locally. Quantum mechanical effects, like the exchange interaction, are approximated by mean fields.

In the experimental studies presented in chapter 4 micromagnetic simulations are used to reproduce the frequency and spatial distribution of eigenmodes of the examined system. The typical procedure is performed as follows:
First, the equilibrium orientation of the magnetization has to be determined. As initialization, the magnetization in every cell is aligned parallel to the static magnetic field $\boldsymbol{M}||\boldsymbol{H}_0$. To find the relaxation orientation of the magnetization, the Gilbert damping is set to an artificially high value and time integration of the Landau-Lifshitz equation is performed leading to the static equilibrium state.
In a second step, a dynamic magnetic field pulse oriented in-plane and perpendicular to the static magnetic field $\boldsymbol{h}_{\mathrm{dyn}} \perp \boldsymbol{H}_0$ is applied. Since the simulations are used to describe structures of finite thickness, the magnetization vector performs an

elliptic precession around the magnetic field vector with the long axis oriented in plane. Accordingly, the excitation by an in-plane field is more efficient. For analysis, the out-of-plane dynamic magnetization is used, since the µBLS setup described above is most sensitive to this component [69]. For the excitation pulse shape a sinc-function is chosen

$$\boldsymbol{h}_{\mathrm{dyn}}(t) = \boldsymbol{h}_0 \frac{\sin(2\pi f_{\mathrm{max}} t)}{2\pi f_{\mathrm{max}} t} \tag{3.9}$$

with $f_{\mathrm{max}} = 20\,\mathrm{GHz}$, since the Fourier transformation of a sinc function is a rectangular function providing an equal excitation power to all frequencies with values below $f_{\mathrm{max}}/2$. Accordingly, eigenmodes with their resonance frequency in this interval will respond resonantly to the excitation field. $\boldsymbol{h}_0$ is the amplitude of the excitation pulse and is chosen sufficiently small to obtain a linear excitation. In contrast to the determination of the equilibrium state, the damping parameter is set to realistic value. By performing Fourier transformations of the calculated out-of-plane dynamic magnetization, power maps $P(\omega, \boldsymbol{r})$ of eigenmodes can be created that resemble BLS measurements.

4 Experimental results

4.1 Direct observation of spin-wave modes excited in a magnetic insulator

In recent years spin waves excited by spin-orbit torques have been broadly investigated. For magnetic 3d metals a large variety of structures was found to support the excitation of auto-oscillations by SOTs [19–22]. These oscillations manifested in the formation of a single spin-wave mode – the so called bullet mode [19, 70] – that due to nonlinear effects demonstrated a self-localizing behavior. Since magnetic insulators like YIG have a lower Gilbert damping parameter than magnetic metals, it was expected that the compensation of the natural damping by spin-orbit torques in YIG based structures should easily facilitate the excitation of coherent magnetization auto-oscillations. In contrast to these expectations, this goal could not be achieved for many years. Only recently, the production of high quality ultrathin YIG films became feasible [24–26], enabling the excitation of auto-oscillations in YIG/Pt bilayers [27, 28, 44].

The experiments demonstrated in this section present the first spatially resolved experimental study of SOT induced auto-oscillations in YIG/Pt bilayers [43]. These measurements allow for a detailed investigation of the behavior of spin waves in insulating magnets close to the threshold current for full compensation of the natural damping of the system. Similar to measurements performed with magnetic metals at electric currents close to the critical value, a strong localization of the magnetization dynamics can be observed. Nevertheless, at currents slightly above the threshold the maximum spin-wave intensity quickly saturates and a strong spatial broadening can be observed. Since the behavior of magnetic systems under the influence of spin-orbit torques is mainly determined by the dynamic nonlinearity, the observed behavior can be attributed to efficient nonlinear mode coupling, which is strongly enhanced in low damping materials like YIG [71].

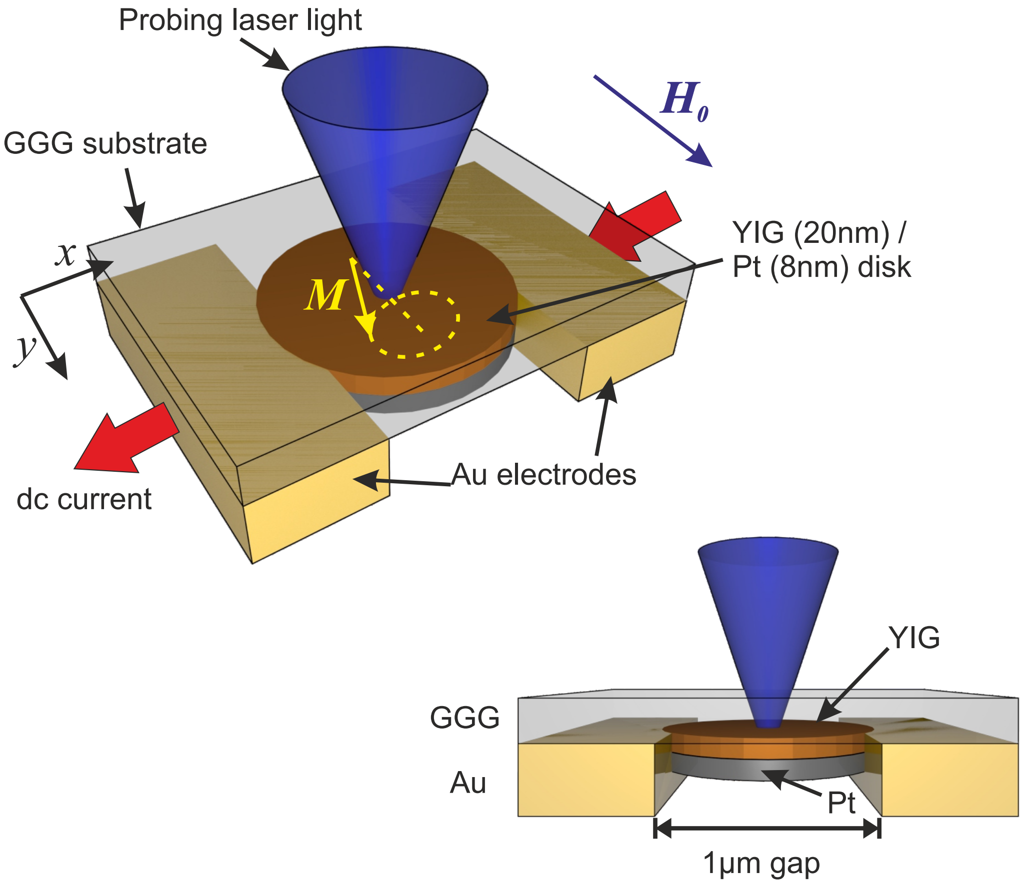

Fig. 4.1: Schematic view of the experimental setup. A YIG(20nm)/Pt(8nm) bilayer disk with a diameter of 2 µm is electrically contacted by two gold electrodes. The electric current in the Pt layer leads to the formation of spin-orbit torques exciting spin-waves in the YIG layer in the 1 µm gap between the Au electrodes. The probing laser beam is focused through the GGG substrate on the YIG surface.

4.1.1 Experimental setup

A schematic representation of the experiment is shown in Fig. 4.1. The magnetic structure consists of a YIG/Pt disk with a diameter of 2 µm, a Pt thickness of 8 nm and a YIG thickness of 20 nm on a GGG substrate. The electric contact to the Pt layer is provided by two Au(80 nm)/Ti(20 nm) electrodes with a gap of 1 µm. Since the resistivity of Pt exceeds the value of Au by about a factor of five [72], significant parts of the electric current only flow through the Pt layer in the gap between the Au contacts. Only in this region, the excitation of spin waves by SOT is possible. Subsequently, this region is called “active area”. The static magnetic field is applied in-plane and perpendicular to the current direction (spin-Hall geometry). The shown current direction corresponds to amplification orientation by SOT and is defined as positive. All the data shown are measured at a representative value of $H_0 = 1000\,\mathrm{Oe}$.

Sample fabrication The YIG layer is grown on a GGG (111) substrate by pulsed laser deposition [25]. The Pt layer was created by dc magnetron sputtering. The dynamical properties of the pure YIG film and the YIG/Pt bilayer were determined from broadband FMR measurements on extended films. E-Beam lithography was used to shape the films into disks [28]. The same technique was used to shape the Au(80 nm)/Ti(20 nm) electrodes. To insulate the system it was covert with a SiO_2 layer of 300 nm thickness. Additionally, a 5 µm wide and 250 nm thick Au antenna was defined on top of the system by optical lithography.

Magnetooptical measurements The spatially resolved measurements are performed using the micro-focus BLS setup as described in section 3.1.1. Since the Pt layer is not transparent, the laser beam is focused through the GGG substrate on the YIG surface. The objective lens is adjusted to compensate the aberration of the substrate. The laser power is chosen to be $P_\mathrm{L} = 0.05\,\mathrm{mW}$ guaranteeing negligible heating of the magnetic structure and accordingly no changes to the saturation magnetization.

4.1.2 Magnetic fluctuations under the influence of spin-orbit torque

In Fig. 4.2 the µBLS spectra for different applied electric currents are shown, recorded at the center of the disk. The black squares demonstrate the spectrum of thermally excited magnons with no applied current. For positive electric currents an increment of I leads to a continuously enhanced BLS intensity, while for negative currents the oscillations are suppressed, as expected in the presence of SOTs. The strong asymmetry indicates negligible contributions of spin-wave excitations by thermal gradients [57, 59]. To confirm that the amplifications originate in SOT, the orientation of the static magnetic field was reversed leading to an inversion of the amplification current direction. This behavior is in agreement with the geometry of the spin-Hall effect.

At the critical current of $I_\mathrm{c} \approx 8\,\mathrm{mA}$ with a corresponding current density of $j_\mathrm{c} \approx 5 \times 10^{11}\,\mathrm{A/m^2}$ (red circles), the natural damping is fully compensated leading to the onset of the SOT induced auto-oscillations, manifesting in the a sudden increment of the detected BLS intensity caused by spin-waves. The detected peak has a narrow spectral linewidth and an intensity that exceeds the BLS intensity of thermal magnons by about two orders of magnitude. The high spin-wave intensity

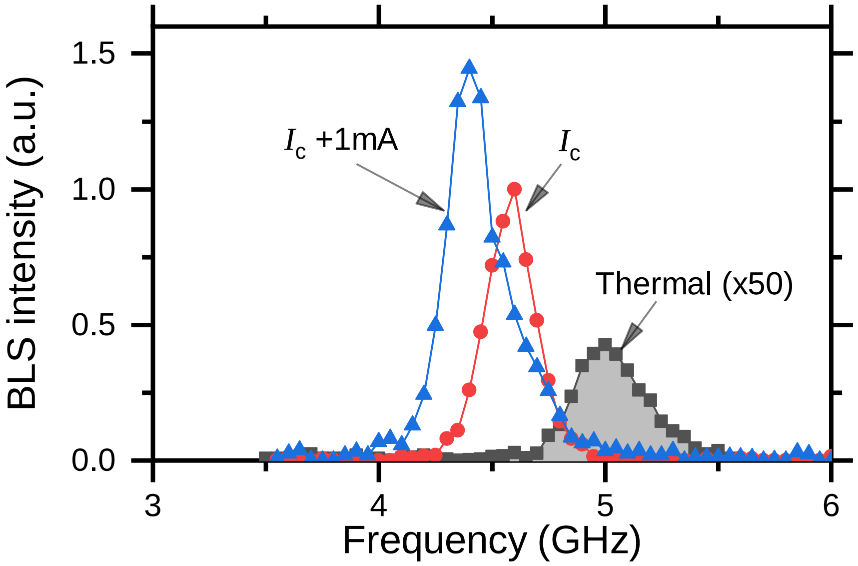

Fig. 4.2: Spectrum of spin-waves recorded by µBLS at the center of the YIG/Pt disk. Thermal spectrum at $I = 0$ (black squares) magnified by a factor of 50, the spectrum at the onset of the auto-oscillations $I = I_c$ (red circles) and the spectrum of auto-oscillations at $I = I_c + 1\,\mathrm{mA}$ (blue triangles) at $H_0 = 1000\,\mathrm{Oe}$.

is accompanied by a negative nonlinear frequency shift as observed in metallic systems [19–22]. Further increment of the current above the threshold value leads to an enhanced reduction of the resonance frequency and to a broadening of the spectral linewidth (see blue triangles) indicating the presence of multimode auto-oscillations and not of singlemode auto-oscillations as observed for all metallic systems.

4.1.3 Spatial distribution of multimode excitations

For a deeper understanding of which spin-wave modes contribute to the observed spectra, the analyzed structure is examined using spatially resolved µBLS measurements by rastering the laser spot in the two lateral directions. A representative power map $P(\boldsymbol{r}, \omega_0)$ of the spin-wave intensity for $I = I_c + 1\,\mathrm{mA}$ is shown in Fig. 4.3. The circle marks the position of the YIG/Pt disk. The region between the white horizontal lines frames the gap between the gold electrodes and therefore marks the active area. In Fig. 4.3 we see, that the auto-oscillations are localized within this region. To be more precise, a clear localization within the y-direction can be observed, while for the x-direction the entire range shows intense excitation of spin waves. The confinement is caused by a combined effect of the Oersted field and Joule heating caused by the electric current in the Pt layer and SOT acting on the magnetization leading to the formation of an effective potential well, as will be explained in more detail in the discussion section 4.1.4.

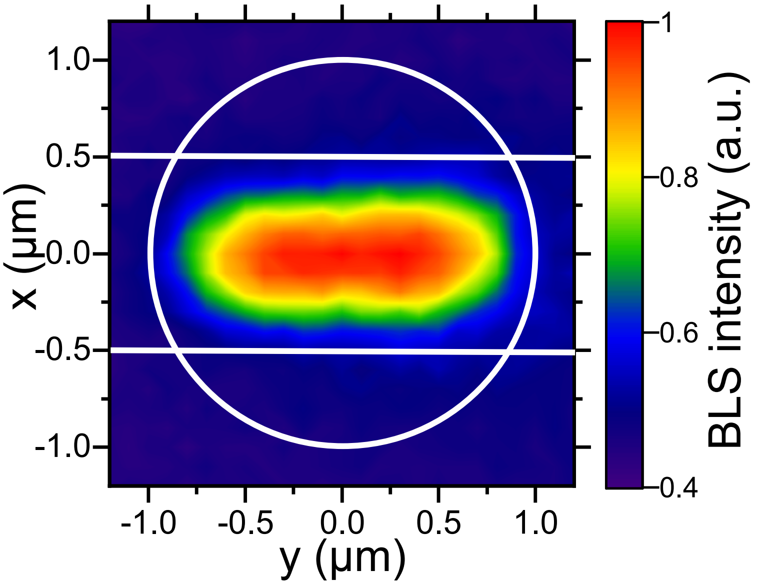

Fig. 4.3: 2D power map of the spin-wave intensity recorded by rastering the focal spot in the lateral dimensions of the structure for $I = I_c + 1\,\mathrm{mA}$ at $H_0 = 1000\,\mathrm{Oe}$. The white horizontal lines frame the gap between the electrodes. The white circle marks the position of the YIG/Pt disk.

Current dependence of the spatial exctend of the auto-oscillations along the y-axis

To achieve a better insight into the origin of this localization, the current dependence of the spatial distribution is investigated. Therefore, spatial scans along the y-axis at the center of the gap ($x = 0$) are performed at different driving currents (see Fig. 4.4a)). It can be seen, that at the onset of the auto-oscillations ($I = I_c$, black squares) the excited spin waves do not cover the entire width of the active area, as it is the case in Fig. 4.3, but only a narrow peak is formed revealing a localization at the center of the YIG/Pt disk. By increasing the current above the excitation threshold, the peak rapidly broadens along the gap width until a wide range of the active area demonstrates auto-oscillations. As can be seen in Fig. 4.4b) the spatial full width half maximum (FWHM) increases linearly with the electric current, starting at a width of about 0.5 µm at I_c until it saturates at about $I = 9\,\mathrm{mA}$ with a FWHM of 1.5 µm.

Also the current dependence of the normalized BLS intensity at the center of the

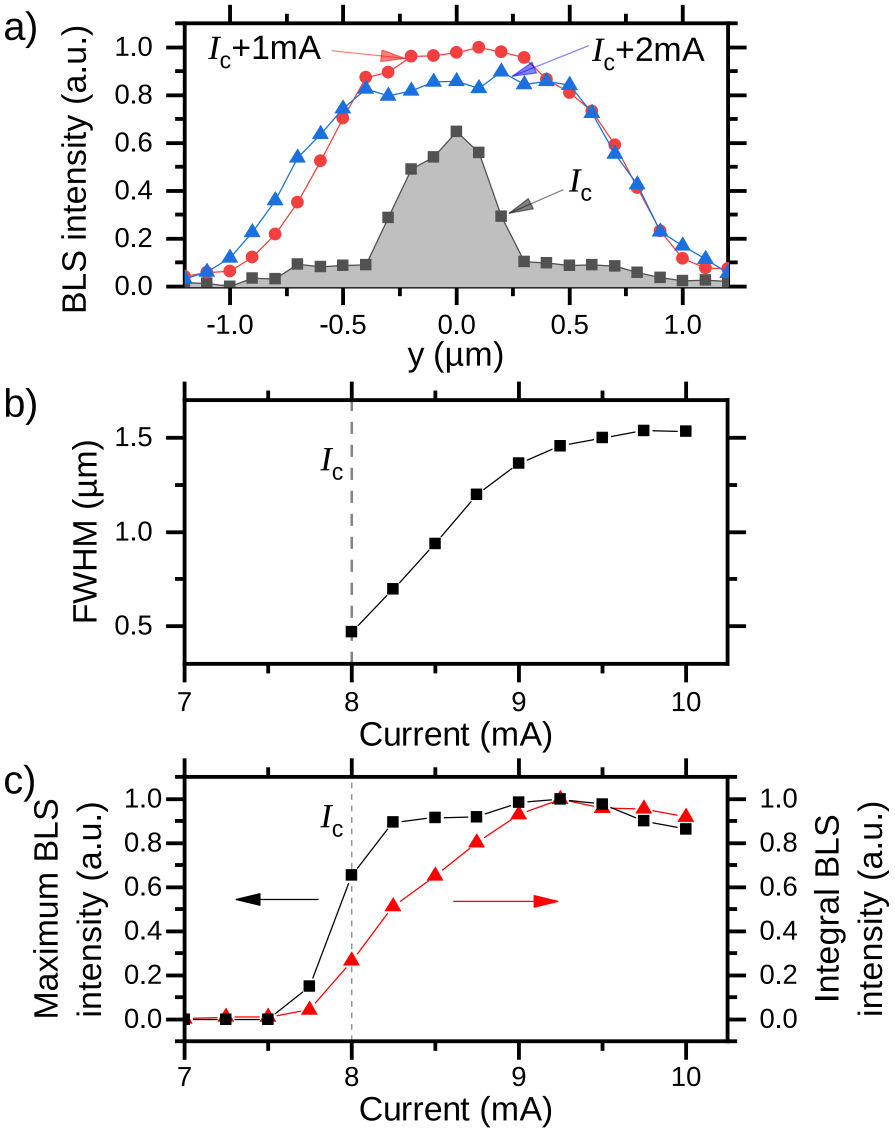

Fig. 4.4: a) 1D spatial scan along the y-direction at the center of the disk for different driving currents: $I = I_c$ (black squares), $I = I_c + 1\,\text{mA}$ (red circles), $I = I_c + 2\,\text{mA}$ (blue triangles). b) FWHM of the spatial distribution in the x-direction displayed against the driving current. c) Current dependence of the normalized BLS intensity integrated along the y-axis (red triangles) and the normalized maximum BLS intensity (black squares). All measurements are recorded at $H_0 = 1000\,\text{Oe}$. The solid lines are guides to the eye.

disk (maximum BLS intensity) and the normalized BLS intensity integrated along the y-axis are investigated (integral BLS intensity) – see Fig. 4.4c). While the maximum intensity (black squares) rapidly increases for currents approaching I_c and than quickly saturates at $I \approx I_\mathrm{c} + 0.2\,\mathrm{mA}$, the integral BLS intensity (red triangles) is enhanced at a slower rate and saturates at $\approx 1\,\mathrm{mA}$ above the point of intensity saturation, therefore following a similar curve as it was observed for the FWHM. Consequently, for driving currents slightly above I_c, the energy transferred to the system does not further increase the maximum amplitude of a single mode, but leads to the formation of a multimode auto-oscillation forming a spatially extended mode that – along the y-axis – is only limited by the lateral dimensions of the YIG disk. This distribution of energy to different spin-wave modes is enabled by the low Gilbert damping constant of YIG, which enhances the efficiency of nonlinear mode coupling [71]. Due to its nonlinear nature, the observed spatially-extended mode cannot be regarded as a linear combination of eigenmodes of the magnetic system [73]. This idea is supported by the spectral broadening detected for $I > I_\mathrm{c}$.

Current dependence of the spatial extend of the auto-oscillations along the x-axis

Following the described scenario for the spatial expansion of excited spin waves in the y-direction, a similar behavior is expected for the x-direction. In contrast, Fig 4.5a) and b) show that no significant excitation of spin waves can be observed outside the active area. Even within the gap, only small changes to the measured FWHM of the auto-oscillation mode are visible, although it has to be mentioned that the spatial resolution of the µBLS setup is limited to $\approx 250\,\mathrm{nm}$ and therefore a detailed analysis of the development of the spatial extend along the x-axis within the gap is to be taken with care.

As for the measurements along the gap width, the maximum and integral intensity in the x-direction are compared (see Fig. 4.5c)). As expected from the weak variations in the FWHM, the maximum and integral intensity show a similar behavior over the entire measured current range. Both quickly rise around I_c and saturate at $I \approx I_\mathrm{c} + 0.2\,\mathrm{mA}$.

The results show that the shape of the multimode auto-oscillations at currents above the excitation threshold is mainly determined by the geometry of the active area. This is in clear contrast to the observations that have been made for auto-oscillations in magnetic metals. In metals, the excitation of auto-oscillations by SOT led to the formation of a single, high amplitude and self-localized spin-wave mode – the so called bullet mode [70] – whose spatial extend is not determined by the size of the region of excitation, but by nonlinear characteristics of the investigated system. Since the natural damping in magnetic metals exceeds the value in magnetic dielectrics like YIG by several orders of magnitude, the nonlinear mode coupling is

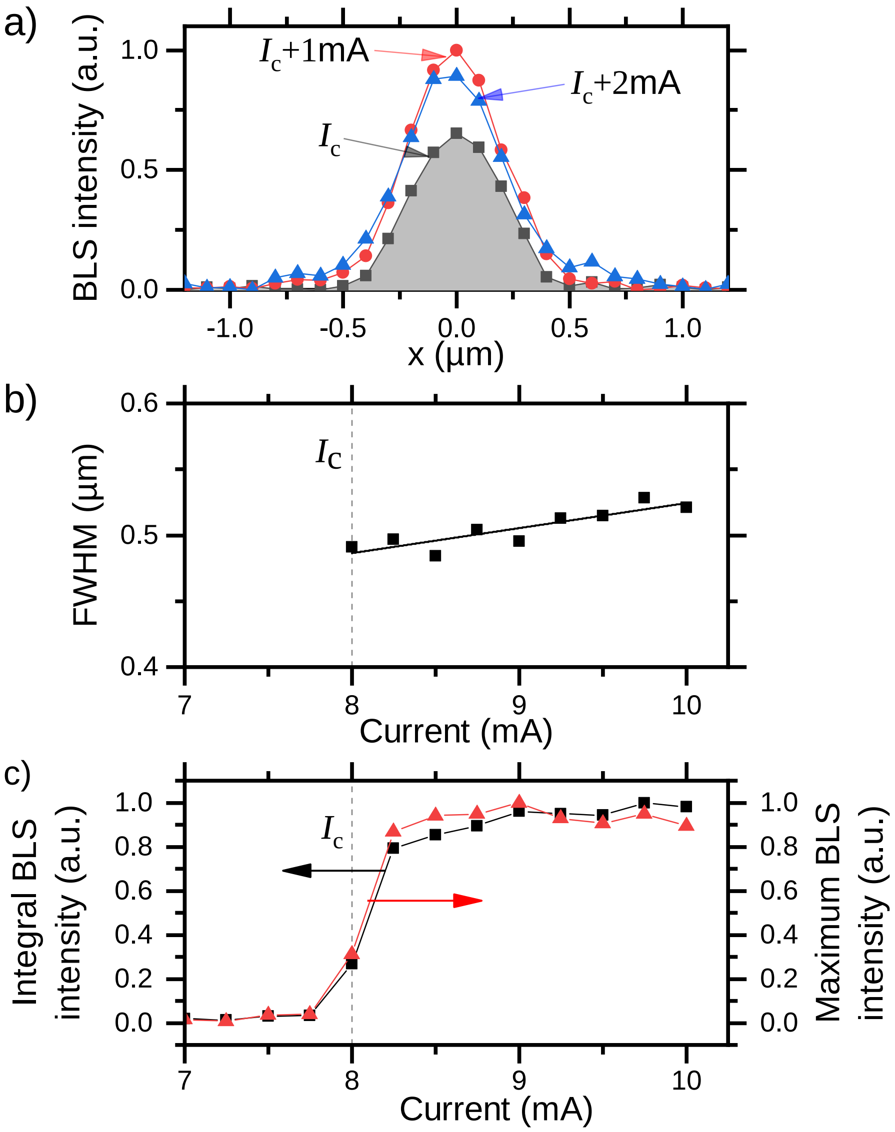

Fig. 4.5: a) 1D spatial scan along the x-direction at the center of the disk for different driving currents: $I = I_c$ (black squares), $I = I_c + 1\,\mathrm{mA}$ (red circles), $I = I_c + 2\,\mathrm{mA}$ (blue triangles). b) FWHM of the spatial distribution in the x-direction displayed against the driving current. c) Current dependence of the normalized BLS intensity integrated along the x-axis (red triangles) and the normalized maximum BLS intensity (black squares). All measurements are recorded at $H_0 = 1000\,\mathrm{Oe}$.

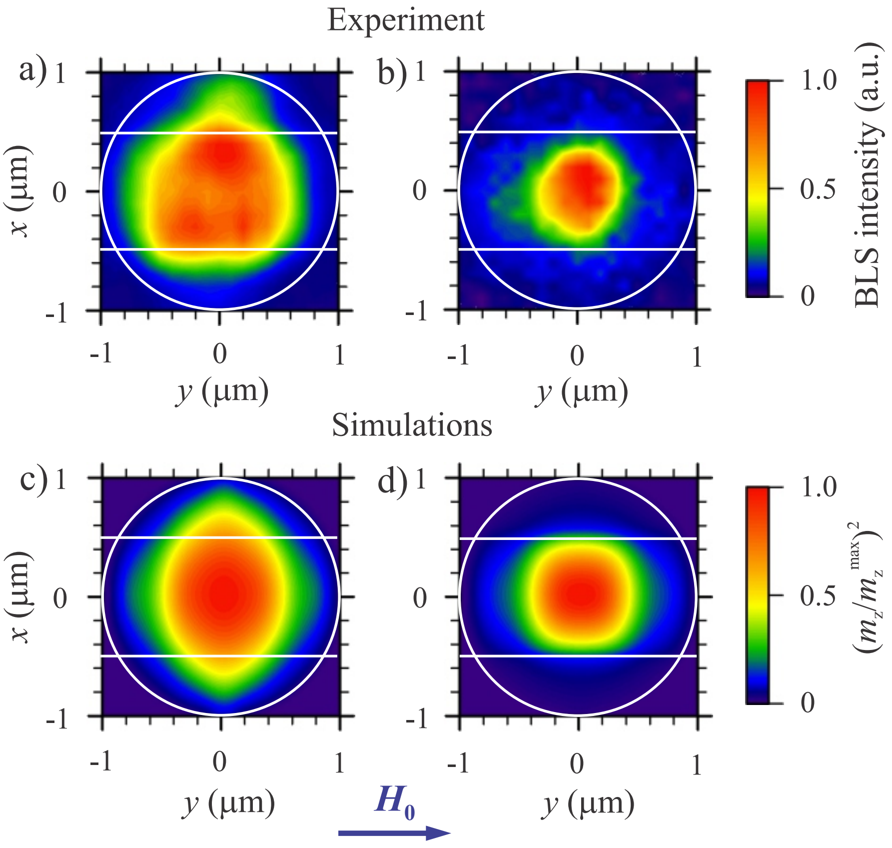

Fig. 4.6: a) 2D spatial scan of the FMR mode excited by a stripe antenna at a direct current of $I = 0$ and b) $I = 7\,\mathrm{mA}$. c) Simulations of eigenmode excitations for uniform material parameters and H_0 across the entire disk and d) for a reduced H_0, α and M_s in the gap between the electrodes.

suppressed, allowing for the formation of singlemode auto-oscillations.

4.1.4 Discussion

Although the auto-oscillations observed in the experiments presented here are confined in the entire active area for $I \geq I_\mathrm{c} + 1\,\mathrm{mA}$, the spatial scans reveal that for currents close to the excitation threshold $I \approx I_\mathrm{c}$ self-localization at the center of the disk is detected. In this section, the behavior of the self-localization of spin waves for $I < I_\mathrm{c}$ will be examined. Therefore, a stripe antenna with a width of 5 μm is used to excite ferromagnetic resonance (FMR) within the YIG disk. A sufficiently small microwave power is applied to exclude nonlinear self-localization effects. These measurements are performed at different electric direct currents in the Pt layer and the corresponding resonance frequency is determined. For $I = 0$ (Fig. 4.6a)) and $I = 7\,\mathrm{mA} < I_\mathrm{c}$ (Fig. 4.6b)) power maps of the BLS intensity are recorded at the corresponding resonance frequencies. At $I = 0$ the FMR mode clearly extends over the entire range of the disk and no confinement can be observed. This is not the case for $I = 7\,\mathrm{mA}$. Here, a strong localization of the FMR mode in all directions is detected. Since this localization cannot be caused by nonlinear self-localization effects due to the low driving microwave power and the applied direct current below the excitation threshold value, another mechanism has to be responsible for the observed behavior. To explain the observations, the formation of an effective potential well within the gap between the electrodes is proposed. This well is formed as a combination of three effects:

- The presence of an Oersted field within the gap between the Au electrodes induced by the direct current. Only within the gap significant contributions are expected, since the spatial extend of the electrodes is much larger than the dimensions of the Pt layer in the gap (Ampère's law). In the spin-Hall geometry for current orientations that lead to the amplification of spin waves, this field is always opposed to the orientation of the external static magnetic field and therefore leads to a reduction of the internal magnetic field within the gap.

- A reduction of the magnetization within the gap due to Joule heating. The flow of a direct current in the thin Pt layer is accompanied by a heating. Since the Curie temperature of YIG is only 560 K [40], its magnetization reacts very sensitive to temperature variations. Accordingly, the current induced heating leads to a notable reduction of the magnetization. This claim is confirmed by the measurements shown in Fig. 4.7. Here, the FMR frequency is plotted against the applied direct current. The displayed distribution is asymmetric due to the Oersted field, which reverses sign under reversal of the current flow. Taking this into account, the magnetization can be calculated using equation (2.6). It can be seen, that the magnetization is symmetric with respect to the current orientation, as expected for a purely heating induced magnetization reduction.

- A local compensation of the system's natural damping. For positive currents below the excitation threshold the natural damping is partly compensated by SOT. As can be taken from equation (2.18), this compensation linearly depends on the applied direct current. Accordingly, the effective damping within the active area is reduced with respect to the rest of the YIG disk.

The combination of these three effects leads to a spin-wave spectrum within the gap that is shifted to lower frequencies with respect to the surrounding material. Due to the proportionality between the relaxation frequency and the precession frequency $\omega_\mathrm{r} = \alpha\omega$ the frequency reduction facilitates excitation of spin waves within

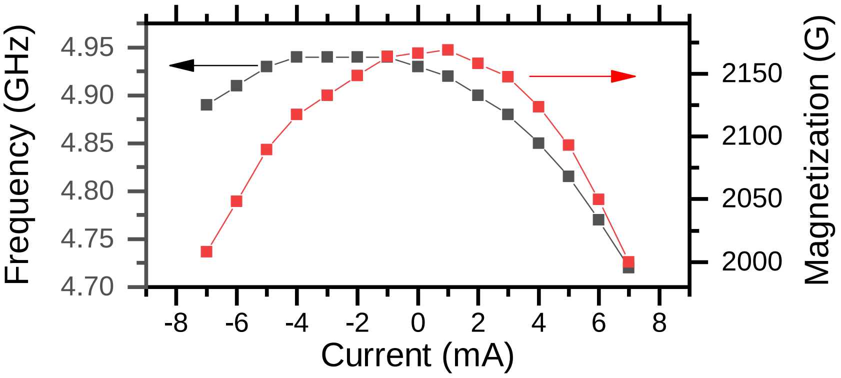

Fig. 4.7: Current dependence of the FMR frequency recorded by µBLS at the center of the disk and the magnetization calculated from the FMR frequency considering Oersted field corrections.

the gap that cannot propagate into the surrounding region due to a mismatch of the spin-wave spectra. The excitation efficiency within the gap is further enhanced by the SOT compensated natural damping. Accordingly, a potential well is formed within the active area that facilitates spin-wave excitation and prevents spin-wave propagation into the surrounding magnetic structure.

To support these claims micromagnetic simulations were performed. The 2 µm diameter disk was simulated on a grid of 10x10x10 nm^3 cells and the eigenmodes were determined as described in section 3.2. The standard value of the exchange constant for YIG was chosen $A_{\mathrm{ex}} = 3 \times 10^{-12}\,\mathrm{cm}^2$. The magnetization was set to $M_{\mathrm{s}} = 2200\,\mathrm{G}$, which is extracted from FMR measurements of an extended film, as was the Gilbert damping $\alpha = 2 \times 10^{-3}$ [28]. The static magnetic field was set to $H_0 = 1000\,\mathrm{Oe}$. For the simulations at $I = 0$ all parameters are uniform across the disk. The results are displayed in Fig. 4.6c) and reveal that the FMR mode is spread over the entire YIG/Pt disk, as it was the case for BLS measurements.
To represent our model in simulations for $I = 7\,\mathrm{mA}$, the static magnetic field, the magnetization and the Gilbert damping are reduced within the gap. The Oersted field is calculated using Ampère's law, the magnetization is taken from the measurements in Fig. 4.7 and the Gilbert parameter is linearly interpolated between the natural value for $I = 0$ and $\alpha = 0$ at $I = I_{\mathrm{c}}$. The results are shown in Fig. 4.6d). It can be seen, that the simulated linear FMR mode is strongly localized within the active area and matches the experimental results very well. It is very likely that this mode is first excited by SOT at the onset of the auto-oscillations.

In conclusion, the experiments show that auto-oscillations in YIG undergo a nonlinear self-broadening, which is in clear contrast to magnetic metals that demonstrate nonlinear self-localization. The broadening is enabled by the low natural damping of insulating magnets that enhances nonlinear mode coupling. This leads to the excitation of multimode auto-oscillations that form a nonlinear mode, which – for sufficiently high excitation currents – covers the entire active area. The broad spectrum of excited modes prevents the formation of highly coherent oscillations, as it is the case for singlemode self-localized auto-oscillations. Here, the self-localization is crucial to the stabilization of the mode. It seems, to achieve self-localization in YIG, further confining potentials or special patterning of the YIG film is needed.

4.2 High-efficiency control of spin-wave propagation in ultra-thin YIG by the spin-orbit torque

In the previous section a possibility to excite spin waves by compensating the systems natural damping through spin-orbit torques was presented. This efficient mechanism to control the effective dissipation in a magnetic system has further applications. In the emerging field of magnonics [5, 8, 74] spin waves are used as signal carriers to be transmitted between a point of emission and detection. Therefore, a mechanism to control the propagation length would be interesting. An implementation via SOT can be realized by shaping a bilayer of a magnetic material and a material with strong spin-orbit coupling into a stripe waveguide. Although this approach seems rather simple, so far only small variations in the propagation length could be achieved – even for all-metallic systems, where the increment was less than a factor of two [75, 76]. Similar experiments have been performed in micrometer thick YIG layers with an attached Pt film. However, since SOT is an interfacial effect, the variation of the propagation length was very limited [77, 78].

In this section, a study of an ultrathin YIG/Pt bilayer stripe waveguide with a YIG thickness of 20 nm is presented [44]. Therefore, propagating spin waves are inductively excited by a stripe antenna and amplified by SOT. The demonstrated technique allows for a highly efficient moderation of the propagation length by nearly a factor of ten. It can be shown, that the effective dissipation of the system linearly depends on the electric current as predicted by the theory (see equation (2.18)). The influence of SOT on the magnetic system can even be used to overcompensate the natural damping. At this point true amplifications would be expected, but the results demonstrate that the system is intensely overdriven, so that actually a suppression of propagating spin waves is observed.

4.2.1 Experimental setup

In Fig. 4.8 a schematic view of the experiment is shown. The magnetic structure consists of YIG(20 nm)/Pt(8 nm) bilayer grown on a GGG substrate with the corresponding layer thicknesses in parentheses. The bilayer is patterned into a 1 µm wide stripe waveguide. A microwave antenna with a width of 3 µm and a thickness of 250 nm on top of the waveguide enables the excitation of propagating spin waves via inductive excitation fields. An electric current in the Pt layer allows for the moderation of the effective damping in the magnetic system by means of the SOT and therefore enables control of the propagation length of the inductively excited spin waves. The magnetic field is applied perpendicular to the long axis of the waveguide and therefore to the propagation direction (the Damon-Eshbach geometry). The direction of the current I shown in Fig. 4.8 corresponds the amplification geometry of SOT and is defined as positive.

Magneto-optical measurements The measurements are performed using the µBLS setup described in section 3.1.1. The laser beam is focused through the GGG substrate on the YIG surface into a diffraction limited spot as described in the previous section. 1D and 2D spatial maps are obtained by rastering the laser spot in the lateral directions. The power of the probing laser was chosen to be $P_\mathrm{L} = 0.1\,\mathrm{mW}$ to assure negligible sample heating by laser light absorption.

Sample fabrication A YIG film of 20 nm thickness is grown on a GGG substrate by pulsed laser deposition [25]. It is covered by an 8 nm thick Pt layer that is created by dc magnetron sputtering. The bilayer is patterned into a stripe waveguide with a width of 1 µm by e-beam lithography. To insulate the system, it is covered by a SiO_2 layer with a thickness of 300 nm. Additionally, a broadband microwave antenna made of Au with a width of 3 µm and a thickness of 250 nm is defined on top of the SiO_2 layer by optical lithography.

4.2.2 Incoherent thermal spin waves and coherent auto-oscillations driven by spin-orbit torques

In a first step the subcritical influence of SOT ($I < I_\mathrm{c}$) on the thermally excited spin-wave spectrum is investigated as shown in Fig. 4.9a). For increasing positive current a strong enhancement of the incoherent magnetic fluctuation can be observed as expected for SOT [17]. Negative currents lead to a suppression indicating negligible spin-wave excitation due to thermal gradients [57, 59]. At currents of $I > 2.5\,\mathrm{mA}$ a sudden increase of the spin-wave intensity is detected marking the full compensation of the natural damping and the onset of coherent auto-oscillations (see Fig.4.9b)). For currents with $I > I_\mathrm{c}$ a spectral broadening of the peak can

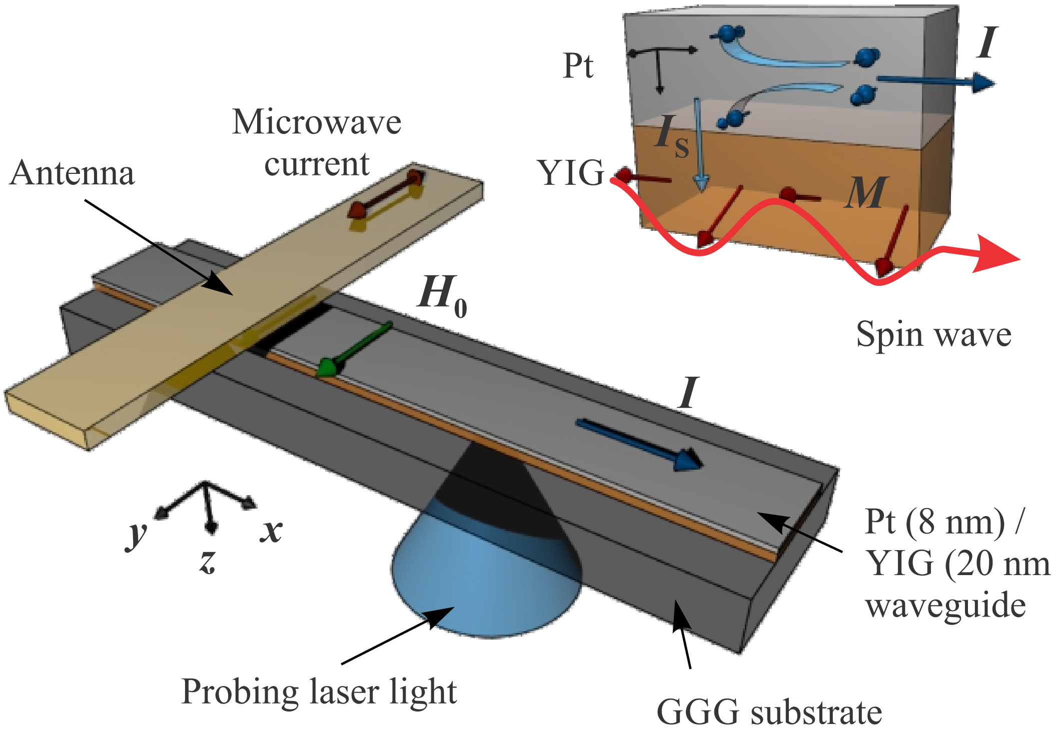

Fig. 4.8: A schematic view of the experimental setup. A YIG(20 nm)/Pt(8 nm) bilayer waveguide with a width of 1 µm. The microwave antenna is used to excite propagating spin waves, the electric current in the Pt layer to moderate the natural damping of the system. The shown current direction corresponds the amplification geometry. The probing laser beam is focused through the GGG substrate on the YIG surface. The inset demonstrates the generation of SOT in a YIG/Pt bilayer acting on the magnetization.

be observed as already known from the experiments on nano disks (see section 4.1) and other experiments on extended structures [17, 22, 47] indicating a multimode auto-oscillation.
To determine the critical current I_c more precisely the integral intensity and the inverse integral intensity of the detected spectra are plotted against the electric current (see Fig. 4.10a)). The data sets are normalized at $I = 0$. The integral intensity (black squares) shows a continuous increase to the point of full dissipation compensation where a strong enhancement is observed (note logarithmic scale). The

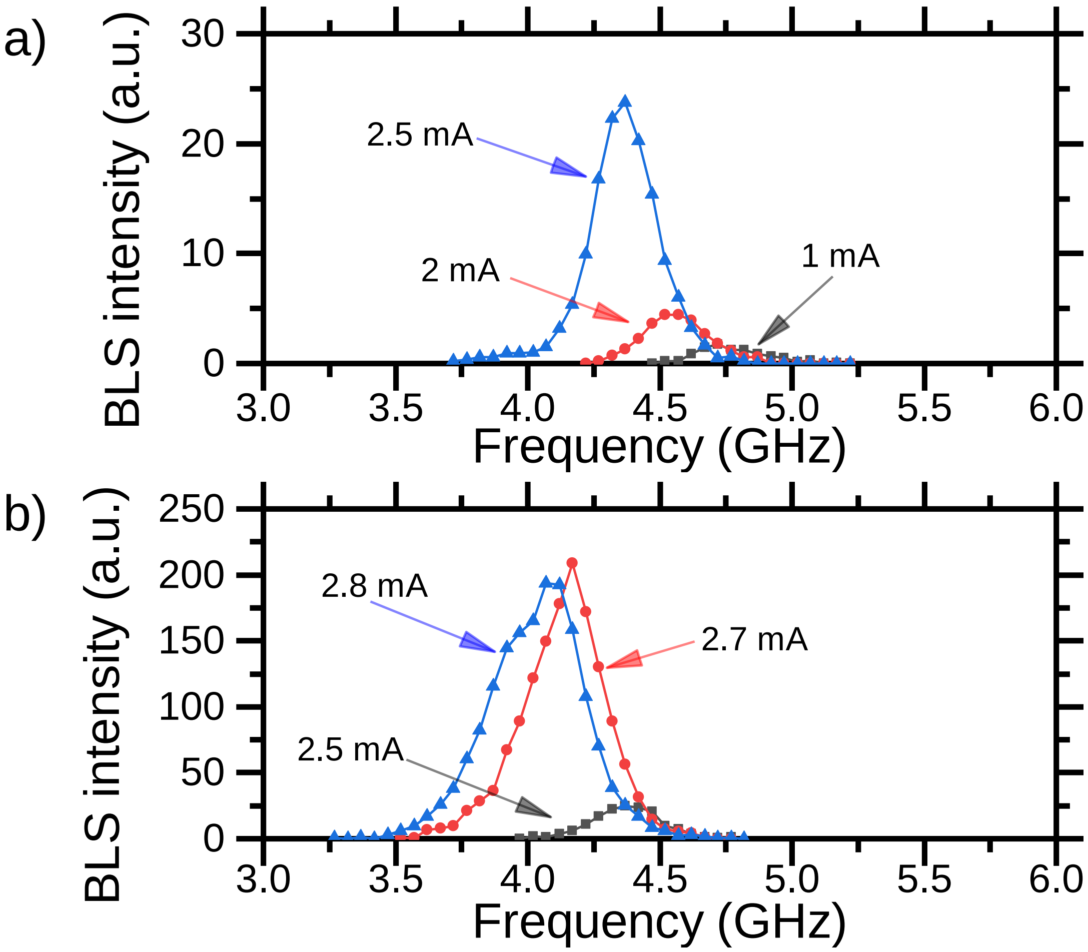

Fig. 4.9: a) and b) Representative spectra recorded by BLS of thermal magnetization fluctuations measured for different electric currents. b) shows 2 spectra for currents above the excitation threshold for auto-oscillations (2.7 and 2.8 mA). The data was measured at $H_0 = 1000\,\mathrm{Oe}$.

inverse integral intensity (red triangles) shows a linear behavior with a negative slope for currents below I_c as expected by theory [54]. A linear fit to the data enables the determination of the critical current as the intersept with the current axis, being $I_\mathrm{c} = 2.58\,\mathrm{mA}$ (see equation (2.25)). The corresponding current density is $j_\mathrm{c} = 3 \times 10^{11}\,\mathrm{A/m^2}$ and is in good agreement with the value reported in the nano disc experiments. At $I > I_\mathrm{c}$ the inverse integral intensity is negligibly small confirming the presence of large amplitude auto-oscillations in the system. Additionally, the value of the effective Gilbert damping α_eff is shown as the upper axis in Fig. 4.10a) as a linear interpolation from $I = 0$ with $\alpha_\mathrm{eff} = 2 \times 10^{-3}$ [28] and $\alpha_\mathrm{eff} = 0$ at the point of full compensation with $I = I_\mathrm{c}$.

The enhancement of the spin-wave intensity with increasing current is accompanied

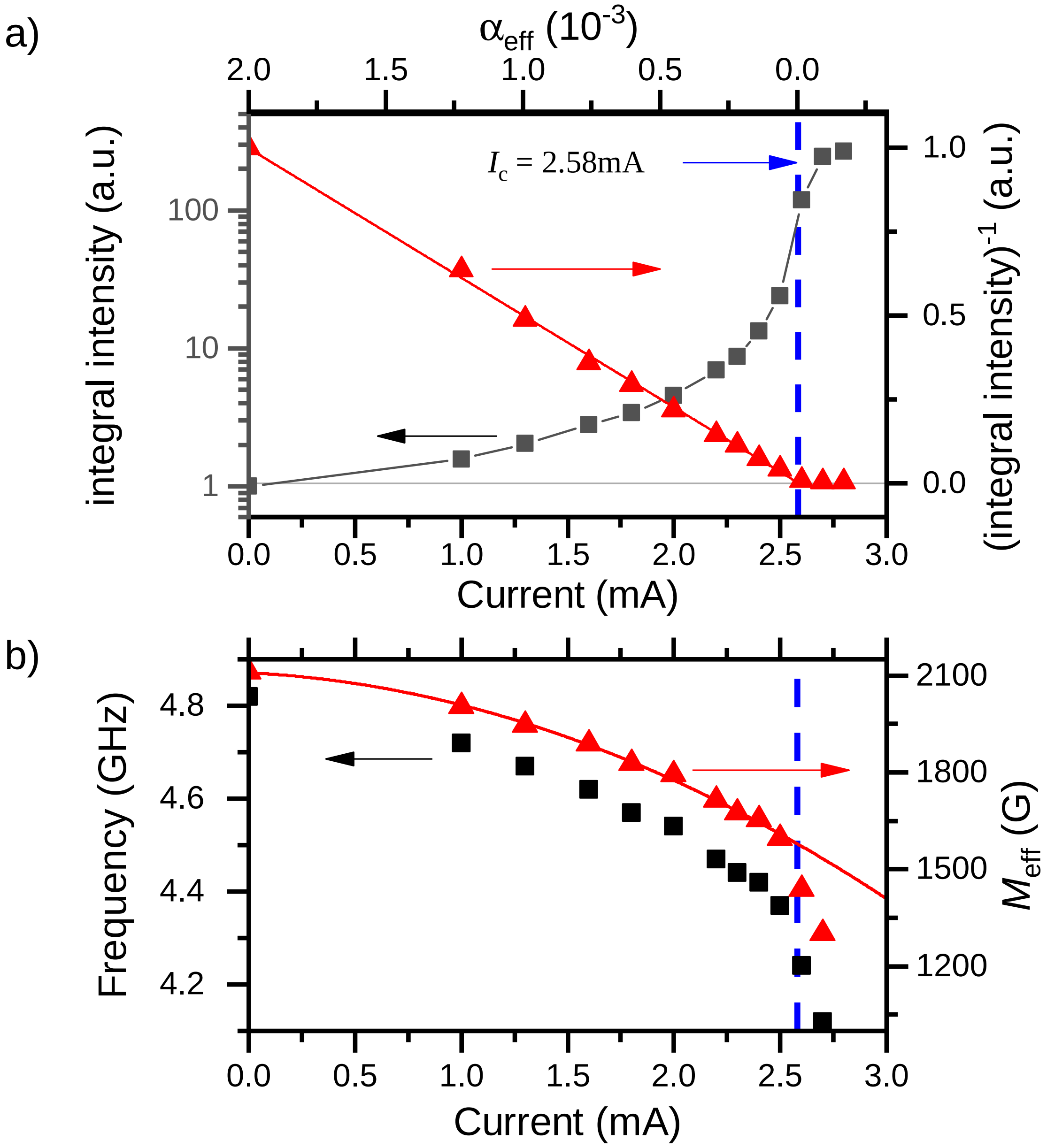

Fig. 4.10: The blue dashed line marks the threshold current, corresponding to full compensation of the natural damping at $I = I_c$ and $H_0 = 1000$ Oe. a) Current dependence of the normalized integral BLS intensity (black squares) and its inverse value (red triangles). The black curve is a guide to the eye, the red line is a linear fit to the data. The α scale is a linear interpolation for the measured Gilbert damping at $I = 0$ and $\alpha = 0$ at $I = I_c$.
b) Current dependence of the frequency of the quasi-uniform mode (black squares) and the magnetization calculated from the detected frequency (red triangles). The red curve is a quadratic fit to the magnetization for $I < I_c$.

by a reduction of the precession frequency of the quasi-uniform FMR mode (see Fig. 4.10b) as it was already observed in the previous section. For a better understanding of the systems behavior, the effective magnetization M_{eff} was calculated using equation (2.6). For currents below the excitation threshold M_{eff} continuously decreases with I^2 (see parabolic fit in Fig. 4.10b)) suggesting that this reduction is dominated by Joule heating. For $I > I_{\text{c}}$ we see, that the reduction is rapidly increased. Since magnetization oscillations at large amplitudes are accompanied by a reduction of the static magnetization component, this observation confirms the presence of auto-oscillations.

4.2.3 Control of the spin-wave propagation length by spin-orbit torques

After gaining inside into the influence of SOT on the magnetic fluctuations of the YIG/Pt waveguide, the interaction of SOT with propagating spin waves inductively excited by a stripe antenna is investigated. The driving frequency was chosen to excite spin waves with a wave length of 5 µm (see [11]). For an antenna with a width of 3 µm this wave can be efficiently excited. In Fig. 4.11a) a representative picture of a two dimensional scan of the propagating wave on a length of 10 µm, performed by rastering the laser spot in the lateral dimensions for $I = 2.55\,\text{mA}$ is shown. The transverse step size is 200 nm, while the longitudinal step size is 250 nm. The scan is started at a distance sufficiently large from the antenna to avoid near field influences. The transverse profile remains independent of the position along the longitudinal axis (see inset Fig. 4.11), indicating a singlemode propagation. This behavior matches the expectations, due to the strong separation of modes in a narrow waveguide [11].

To analyze the current dependence of the propagation length, the spin-wave intensity in the longitudinal direction is mapped for different electric currents (see Fig. 4.11b)). A well-defined exponential decay in all cases can be observed (note logarithmic scale) with the BLS intensity proportional to $\exp(-x/2\sigma)$, where σ is the propagation length defined as the distance over which the spin-wave amplitude is reduced by a factor of e. It can be seen, that the propagation distance significantly increases with increasing direct electric current in the Pt layer, as expected for SOT.

The current dependences of the propagation length (up triangles) and its inverse value – the decay constant (down triangles) – are displayed in Fig. 4.11c). The propagation length continuously increases for $I < I_{\text{c}}$. The maximum observed propagation length is $\sigma = 22.5\,\mu\text{m}$.

An increment of the electric current beyond the onset point of auto-oscillations – the region, where true amplification would be expected – leads to a rapid reduction of

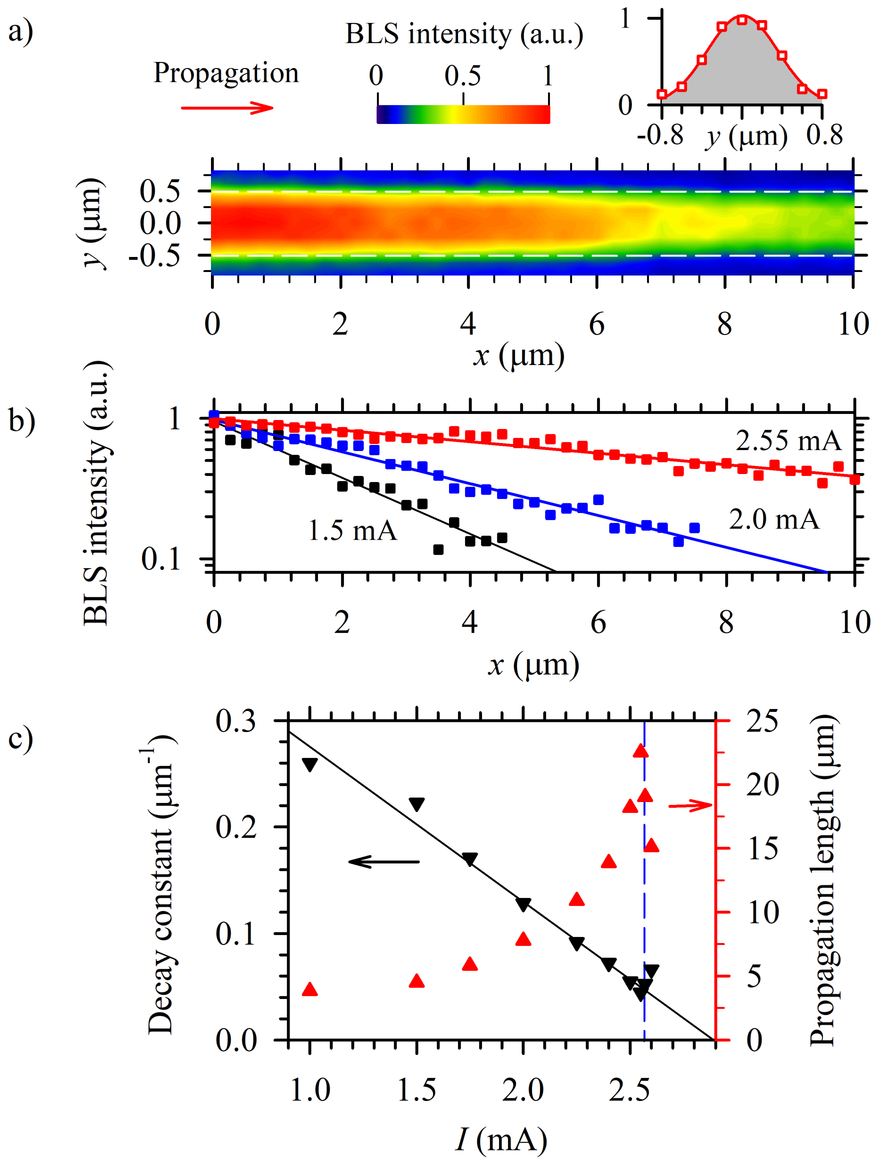

Fig. 4.11: a) Representative 2D mapping the BLS intensity of propagating spin waves excited by a stripe antenna at $I = 2.55\,\mathrm{mA}$ in a waveguide with a width of 1 μm. The scan is performed by rastering the laser spot in the lateral dimensions in an area of 1.6×10 μm. The inset shows a transversal profile of the spin-wave intensity.

b) Representative 1D longitudinal scans of the BLS intensity for different electric currents, in the log-linear scale. The lines are exponential fits to the data.

c) Propagation length (red up triangles) and decay constant (black down triangles) extracted from exponential decay in 1D mappings. The black curve is a linear fit to the decay constant. The blue dashed line marks the onset current I_c.

The data was measured at $H_0 = 1000\,\mathrm{Oe}$.

the propagation length. Already at $I = 2.65\,\mathrm{mA}$ the signal of spin waves excited by the antenna cannot be detected anymore. The behavior at $I > I_\mathrm{c}$ is caused by magnon-magnon scattering of the coherently excited propagating magnons from the high intensity auto-oscillation magnons that occupy the entire waveguide. Due to the low Gilbert damping in YIG this scattering process is highly efficient [6].

The decay constant shows a well-defined linear decrease with the electric current for $I < I_\mathrm{c}$ and therefore matches the expectations, since the decay constant is proportional to the effective Gilbert damping. From a linear fit to the data and an extrapolation to $I = 0$ the propagation length without the influence of SOT can be estimated to be $\sigma_0 = 2.4\,\mu\mathrm{m}$. This value is in good agreement with the predicted value ($\sigma_0 = 3\,\mu\mathrm{m}$) for the described waveguide with a Gilbert damping of $\alpha = 2 \times 10^{-3}$ and a wave length of $5\,\mu\mathrm{m}$, following the calculations in [11]. It is to be mentioned, that with the maximum observed propagation length of $22.5\,\mu\mathrm{m}$ the value of σ_0 is exceeded by nearly a factor 10, which is a strong improvement to previously demonstrated systems [75–78].
The linear fit to the decay constant additionally reveals that the intersect with the current axis is found at a value slightly above I_c. This deviation from first expectations can be explained by Joule heating. For increasing currents below I_c a continuous reduction of the magnetization is observed (see Fig. 4.10b)). This change is accompanied by a decrease in the group velocity v_g of the spin waves. Since the propagation length is proportional to v_g, Joule heating increases the decay constant and the described deviation from the expectations is observed.
For electric currents above the threshold the decay constant increases again due to efficient magnon-magnon scattering.

4.2.4 Discussion

The experiments demonstrate, that SOT is a highly efficient mechanism to control the propagation length of coherently excited spin waves in ultrathin YIG stripe waveguides. An increment of the propagation length by an approximate factor of ten could be observed, therefore exceeding the results of previous studies by far [75–78]. To put the observations into perspective, the normalized intensity after a propagation distance of $L = 10\,\mu\mathrm{m}$ – an application relevant distance – is plotted against the electric current (see Fig 4.12). The intensity is calculated following this equation

$$b(I) = b_0 \exp[-2L/\sigma(I)] \tag{4.1}$$

with b_0 as the amplitude at the point of excitation. $\sigma(I)$ uses the experimentally determined values. It can be seen, that for currents below the threshold value,

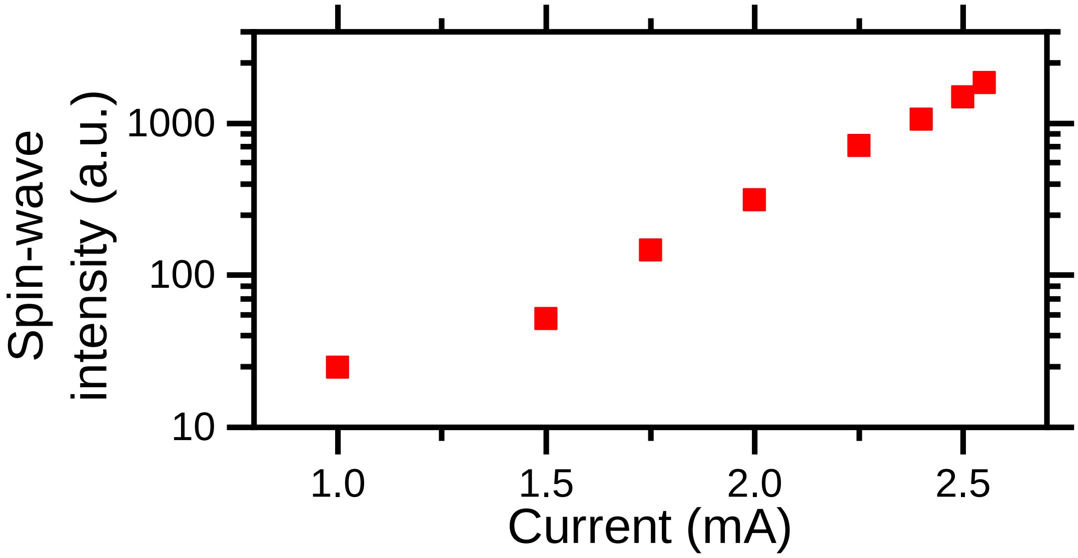

Fig. 4.12: Spin-wave intensity after propagating a distance of 10 µm displayed against the electric current calculated from measured propagation length.

the spin-wave intensity varies by more than three orders of magnitude and can be precisely controlled over the entire range.

Additionally, some limitations to this process were detected. For currents below the point of full damping compensation the efficiency is reduced due to Joule heating. The corresponding reduction of the magnetization and therefore of the group velocity leads to a decline of the propagation length. This effect can be reduced by using a narrower waveguide leading to an increment in the current density and therefore to a lower electric current that needs to be applied.

The second problem is the highly efficient magnon-magnon scattering for currents above the compensation threshold. If this effect could be avoided, true amplification of propagating spin waves should be expected due to the overcompensation of the system's natural damping. At this moment, it is not fully understood if this problem can be overcome in the future.

4.3 Spin-orbit torque induced auto-oscillations in ultrathin YIG grown on Pt

For the YIG films the Gilbert damping parameter strongly depends on the quality of the crystalline structure of the examined sample [24, 25, 79, 80]. Accordingly, to enable the growth of high-quality YIG, a proper substrate is needed. For YIG typically Gadolinium Gallium Garnet is chosen due to the same crystalline structure and a negligible lattice mismatch of 0.057 % [79, 81]. The utilization of a different substrate leads to a significantly increased magnetic damping [82]. This requirement sets two strong limitations on YIG as a material for applications:
Since one YIG surface has to be in contact with the substrate, the flexibility of SOT based devices is reduced. A double-sided injection of a pure spin-current into the magnetic layer is impossible under these conditions [83].
Another problem occurs with the integration of YIG based structures into traditional semiconductor technology, which is Si-based. Here, the need for a GGG substrate to produce high-quality YIG strongly reduces the compatibility.

In this section, a nano-oscillator based on a YIG film grown on a Pt layer is demonstrated [47]. The film is patterned into a nanowire, that allows for efficient suppression and enhancement of magnetic fluctuations by SOT. At current densities comparable to the values for structures described in the previous sections, the system's natural damping can be fully compensated and the onset of auto-oscillations is observed. Surprisingly, although the current density is similar to that of previously demonstrated structures, the linewidth and therefore the damping of the nanowire is relatively large, which should lead to an increment of the critical current density. The origin of this deviation from simple expectations is most likely to be found in an increased transparency of the YIG/Pt interface with respect to spin currents [84] for a YIG layer grown directly on the Pt layer instead of the other way around.

4.3.1 Experimental setup

A schematic view of the experiment is shown in Fig. 4.13. The magnetic structure consists of a YIG film with a thickness of 35 nm that is directly grown on a 5 nm thick Pt layer grown on top of a GGG (110) substrate. The YIG/Pt bilayer is patterned into a nanowire with a width of 200 nm, a length of 2 µm and two adjacent contact pads used for wire bonding. The inset of Fig. 4.13 shows an SEM image of the structure. The static magnetic field $\boldsymbol{H}_0$ is applied perpendicular to the longitudinal axis of the nanowire and therefore to the direction of the electric current flow (spin-Hall geometry). The displayed orientation of the electric current is defined as positive and corresponds to the amplification orientation, for which the natural damping of the system can be compensated by SOT.

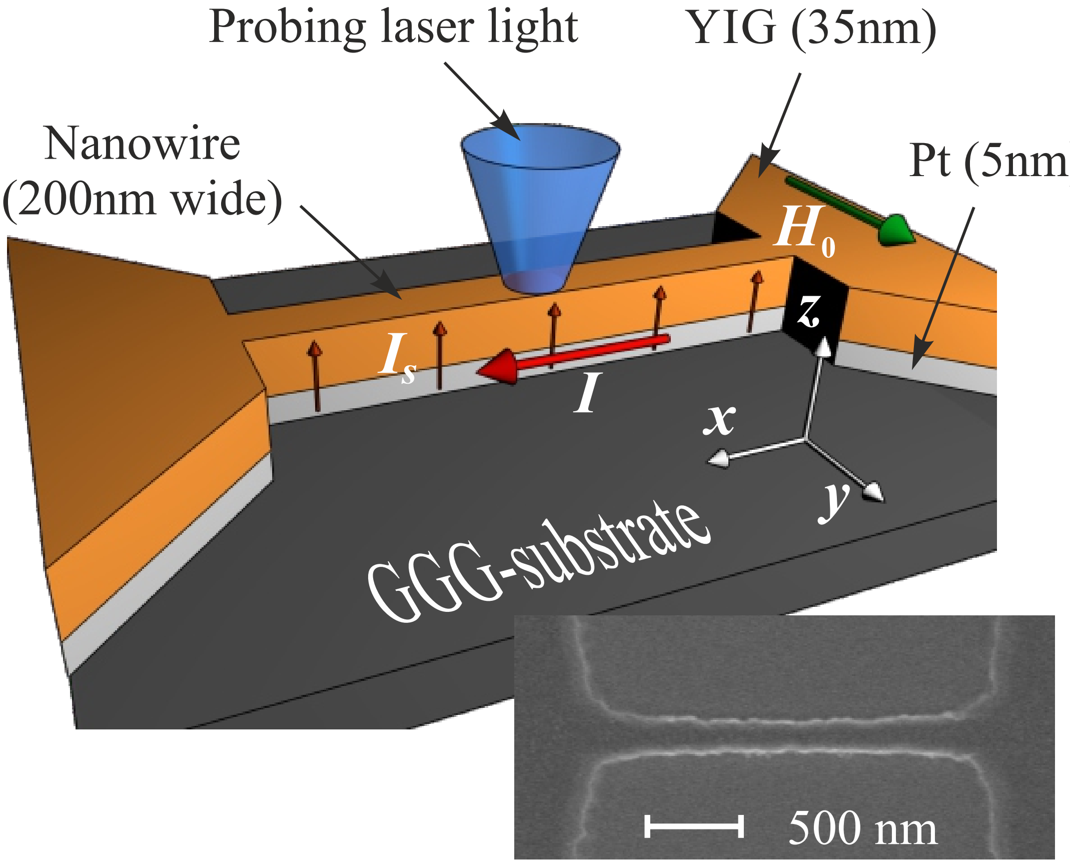

Fig. 4.13: Schematic view of the experiment. A GGG/Pt(5 nm)/YIG(35 nm) trilayer patterned into a nanowire of width 200 nm and length 2 µm. The shown current orientation corresponds to the amplification orientation by spin-orbit torques. The inset shows an SEM image of the examined structure.

Sample fabrication In a first step, the Pt layer is sputtered on the GGG surface by dc magnetron sputtering. Then, the YIG layer is grown by pulsed laser deposition and post annealing on the Pt layer. A description in more detail and the magnetic properties can be found in [81].
The nanowire with two contact pads is patterned by defining a negative resist etching mask via a single step e-beam lithography. Using ion mill etching, the mask pattern is transferred to the bilayer. The remaining resist is removed by oxygen plasma cleaning.

Magnetooptical measurements The magnetooptical measurements are performed using a µBLS setup as described in section 3.1.1. In contrast to the previous sections the laser is not focused through the substrate, but directly on the YIG surface, since the Pt layer does not block the light path.

4.3.2 Identification of edge and center modes

Due to the high sensitivity of Brillouin light scattering to even low amplitude magnetic fluctuations, the initial state of the nanowire without an electric current applied can be investigated. A representative BLS spectrum caused by thermally induced spin waves recorded at the center of the nanowire for $H = 500\,\mathrm{Oe}$ is shown in Fig. 4.14 (red curve). A broad spectrum of multiple spin-wave modes can be observed. To understand the nature of these thermal fluctuations, micromagnetic simulations are performed to determine the eigenmodes of the nanowire as described in section 3.2. The magnetization is independently determined to be $M_\mathrm{s} = 1600\,\mathrm{G}$ from BLS measurements of the frequency of the quasi-uniform FMR mode on the extended contacts pads. The Gilbert damping is chosen to be $\alpha = 5 \times 10^{-4}$ and is therefore artificially low to allow for a clear separation of the eigenmodes. The numerically calculated spectrum is shown in Fig: 4.14 (shadowed area). As for the BLS spectrum, the appearance of several modes can be observed. The two main peaks correspond to the fundamental mode of the edge modes (EM) and the center modes (CM). The transverse profiles of these modes are shown in the inset of Fig. 4.14. The large amplitude at the edges of the nanowire occur due to the absence of the magnetic wall boundary, which is only present in systems with a vanishing thickness to width ratio [48]. The smaller peaks observed at higher frequencies than of the main peaks are higher order longitudinal modes of the nanowire [22]. Higher order transversal modes are not expected to contribute to the observed spectrum, since – due to the narrow width of the wire – these modes correspond to much higher frequencies. It can be seen, that the simulated frequency of the center mode matches the center frequency of the main experimentally detected peak very well, therefore identifying it as the fundamental centre mode of the nanowire. As for the simulation, this peak is accompanied by a series of peaks with decreasing amplitude for

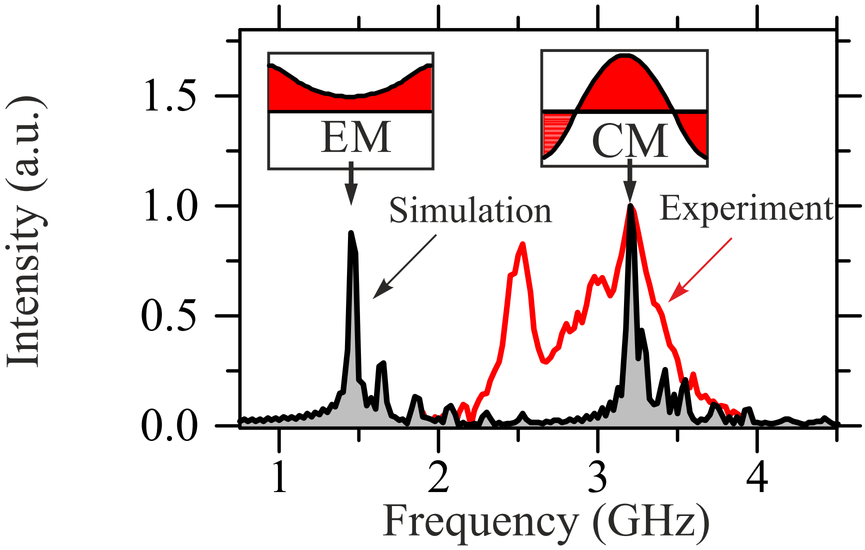

Fig. 4.14: Normalized BLS spectrum recorded at $I = 0$ at the center of the nanowire (red curve) and a simulated spectrum of the eigenmodes of the nanowire (shadowed area). The insets show the transversal amplitude profile of the edge mode (EM) and the center mode (CM).

increasing center frequency of the mode's peak, although these higher order modes are much harder to identify, due to the broad linewidth.

In contrast to the precise matching of the center mode, a clear mismatch between the predicted frequency of the fundamental edge mode and the suspected edge mode in the BLS spectrum at 2.5 GHz is observed. This behavior corresponds well to previous studies, where the measured EM was also located at frequencies above the simulated value [46, 85]. This deviation was attributed to a partial external pinning of spins at the edge of the nanowire [85] caused by a combination of several effects including edge dilution effects, a non-zero surface anisotropy and an edge roughness.

Nevertheless, due to the micromagnetic simulations the peak at 2.5 GHz can be clearly identified as the fundamental edge mode of the system. The higher order longitudinal modes overlap with the lower frequency tail of the fundamental center mode peak.

4.3.3 Current induced control of spin waves and auto-oscillations

After a deeper understanding of the nanowire's eigenmodes was gained, the dependence of the magnetic fluctuations in the nanowire under the influence of an electric current in the Pt layer is investigated. The corresponding BLS spectra are shown

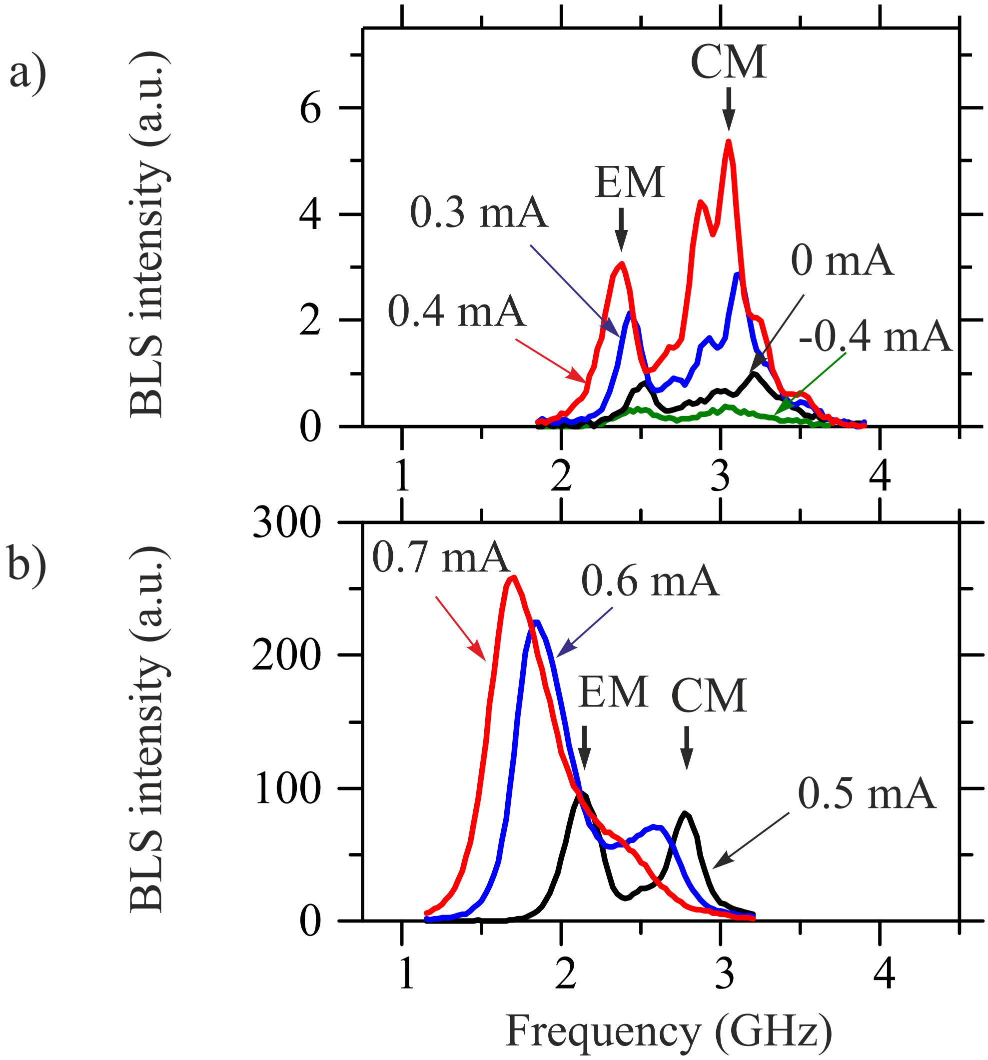

Fig. 4.15: BLS spectra recorded at the center of the nanowire under the influence of spin-orbit torques a) currents below the excitation threshold of auto-oscillations and b) for currents close to the excitation threshold ($I = 0.5\,\text{mA}$, black curve) and currents in the auto-oscillation regime.

in Fig. 4.15a) and b). For a positive current direction an amplification of the entire BLS spectrum caused by magnetic fluctuations is detected as it is known for SOT [17]. For $I < 0.5\,\text{mA}$ (see Fig. 4.15a)) a continuous increase of the intensity is observed, that is accompanied by a frequency red shift due to a reduction of the static magnetization by Joule heating as described in the previous sections. For currents with $I \geq 0.5\,\text{mA}$ a strong enhancement of the BLS intensity is observed

marking the point of full compensation of the natural damping and the onset of auto-oscillations. Increasing the electric current above $I = 0.5\,\mathrm{mA}$ leads to a significant spectral broadening of the BLS spectrum, until the center mode cannot be separated from the edge mode anymore. It is to be noted, that although initially the amplitude of the center mode slightly exceeded the peak detected for the edge mode, the amplitudes become approximately equal at the onset of the auto-oscillation, while for a further raise of the electric current the BLS spectrum is dominated by the amplified edge mode. This behavior is in good agreement with studies of the influence of SOT on the chemical potential that predicts a stronger increment of the spin-wave intensity for modes with a lower precession frequency [86]. For $I \geq 0.5\,\mathrm{mA}$ the frequency shift is dominated by a negative nonlinear frequency shift due to the presence of high amplitude spin waves as it was observed in the previous sections.
For negative currents a suppression of the magnetic fluctuations can be observed as it is shown in a representative image for $I = -0.4\,\mathrm{mA}$ in Fig. 4.15a) (green curve). Here, as for positive currents, a frequency shift due to Joule heating can be seen.

To determine the current dependence of the spin-wave intensity more precisely the integrated intensity (blue squares) and its inverse value (red squares) are displayed against the electric current (see Fig. 4.16a)). The data is normalized at $I = 0$. As described before, a strong enhancement of the BLS intensity can be seen at $I \geq 0.5\,\mathrm{mA}$ that for a further increment quickly reaches a point of saturation. This behavior supports the previously stated idea that close to $I = 0.5\,\mathrm{mA}$ the natural damping of the system is fully compensated and the onset of auto-oscillations is observed. This claim becomes even more evident, if we take a look at the inverse integral BLS intensity. For currents below $I = 0.5\,\mathrm{mA}$, a linear decrement over the entire measured range can be observed, even for negative currents. This demonstrates, that the enhancement and suppression of spin waves is dominated by spin-orbit torques and no significant contributions of spin-wave excitation due to thermal gradients is present. The absence of the spin-Seebeck effect [57, 59] – although previous experiments with YIG/Pt nanowires have demonstrated strong influence of thermal gradients on the spin-wave intensity [45,46] – can be explained by the reversed order of layers. In traditional systems the Pt layer is grown on top of the YIG layer where the GGG substrate acts as a heat sink, while the heating is produced in the Pt layer by Joule heating. This configuration leads to a thermal gradient across the YIG layer and therefore enables the excitation of spin waves by means of the spin-Seebeck effect [45, 46]. In the system examined here, the Pt layer and therefore the heat source is in direct contact with the heat sink so that no thermal gradient is created in the YIG layer.
By performing a linear fit to the inverse integral intensity for currents with $I < 0.5\,\mathrm{mA}$, the intercept with the current axis can be determined. This value coincides with the point of full damping compensation and therefore marks the onset current of auto-oscillations [54]. The value found is $I_\mathrm{c} = 0.51\,\mathrm{mA}$ corresponding to a current

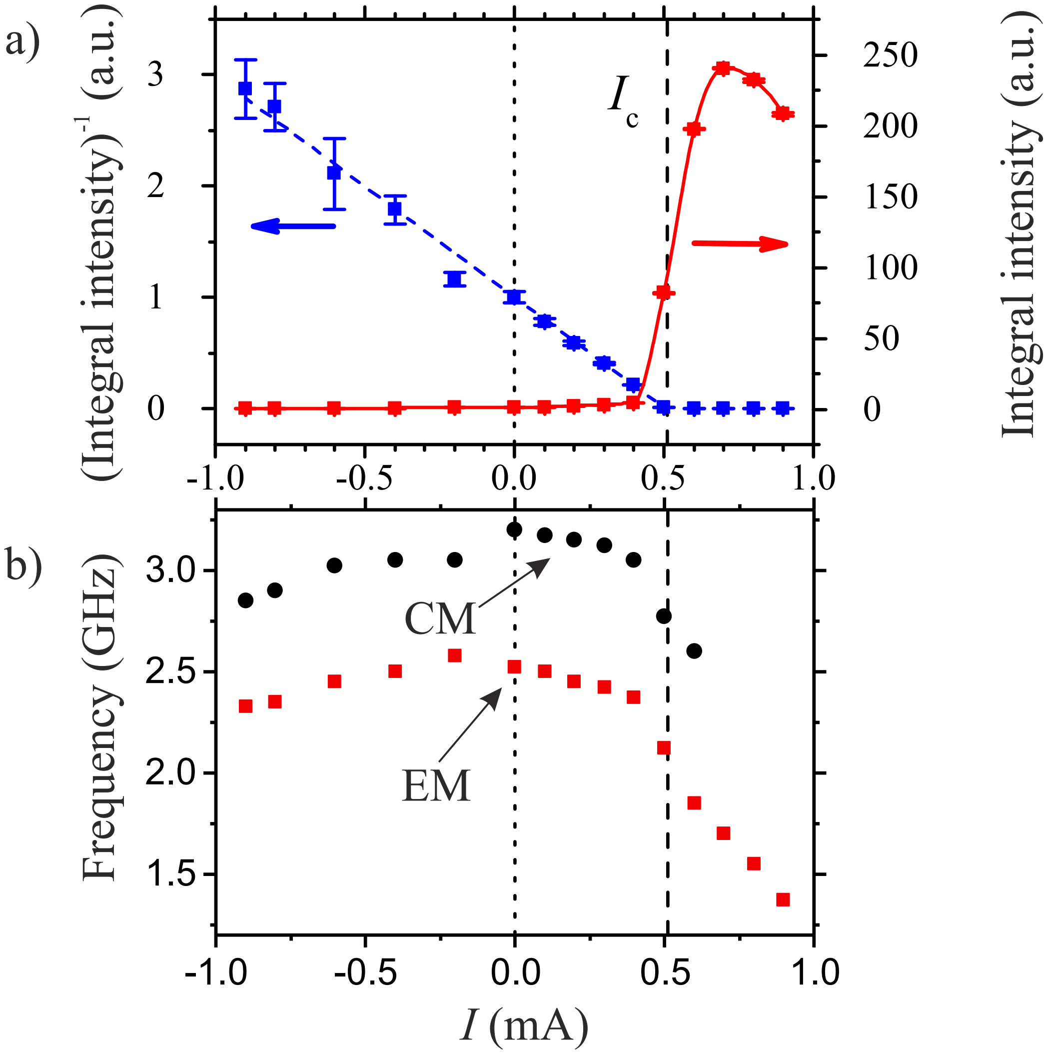

Fig. 4.16: a) Inverse integral BLS intensity and integral intensity displayed against the electric current both normalized at $I = 0$.
b) Frequency of the fundamental center and edge mode displayed against the electric current.
The dashed line in both figures marks the full compensation of the natural damping by SOT, the dotted line separates the region of spin-wave amplification by SOT from the suppression region ($I = 0$).

density of $j_c \approx 5 \times 10^{11}\,\mathrm{A/m^2}$, which is comparable to the values measured in systems grown in the classical order as demonstrated in the previous sections [43, 44]. Although a clear separation of the edge and centre mode is not possible due to their linewidth, it can be estimated that both modes enter the auto-oscillation regime at

$I \approx I_\mathrm{c}$ as it is known for all-metallic nanowires as well [22].

Additionally to the dependence of the intensity on the electric current, the frequency shifts for the fundamental edge and center mode are investigated. The results are shown in Fig. 4.16b). For $|I| < I_\mathrm{c}$, a nearly symmetric reduction with the magnitude of the electric current is observed as expected for a frequency shift purely caused by a reduction of the static magnetization by heating. The small deviation of the curve from a perfect symmetry with respect to $I = 0$ can be explained by an Oersted field that increases the internal magnetic fields with $I < 0$ and leads to a reduction for a reversed current orientation. Still, this effect is only visible for currents close to zero, for larger currents the behavior is dominated by Joule-heating.
For $I \geq I_\mathrm{c}$ a significant enhancement of the negative frequency shift can be observed. As described in the previous sections, this reduction of the precession frequency is caused by the presence of high-amplitude spin waves in the auto-oscillation regime that effectively reduce the static component of the magnetization and therefore the precession frequency. This behavior can be observed for the center mode and for the edge mode. For the center mode, this process can only be tracked up to an electric current of $I = 0.6\,\mathrm{mA}$. For higher values, the fundamental center mode cannot be properly separated from the edge mode anymore and a precise determination of the mode's frequency is not possible. This nonlinear frequency shift is not observed for negative currents, again confirming a dominant SOT influence.

4.3.4 Discussion

A similar behavior for the spin-wave intensity and frequency was observed in the entire measured range of the static magnetic field H_0 from 300 to 1000 Oe. In Fig. 4.17a) the current density for the onset of auto-oscillations j_c (blue squares) and the precession frequency of the center mode (black up triangles) and the edge mode (red down triangles) at the onset of auto-oscillations are displayed against the static magnetic field. As expected, the frequency of both modes continuously increases with the external field. In contrast, the onset current density remains constant over the entire measured range. This is in contradiction to the expectations, predicting a stronger influence of SOT on modes with a lower precession frequency [86]. According to theory, the onset current density is expected to be proportional to the to the relaxation frequency ω_r [54, 87]. In the approximation of an infinite thin film, the relaxation frequency is given by [54]

$$\omega_\mathrm{r} = \alpha\gamma(H + 2\pi M_0). \tag{4.2}$$

Consequently, the current density is expected to be vary by about 50 % in the investigated range of magnetic fields. This is apparently not the case here. As described

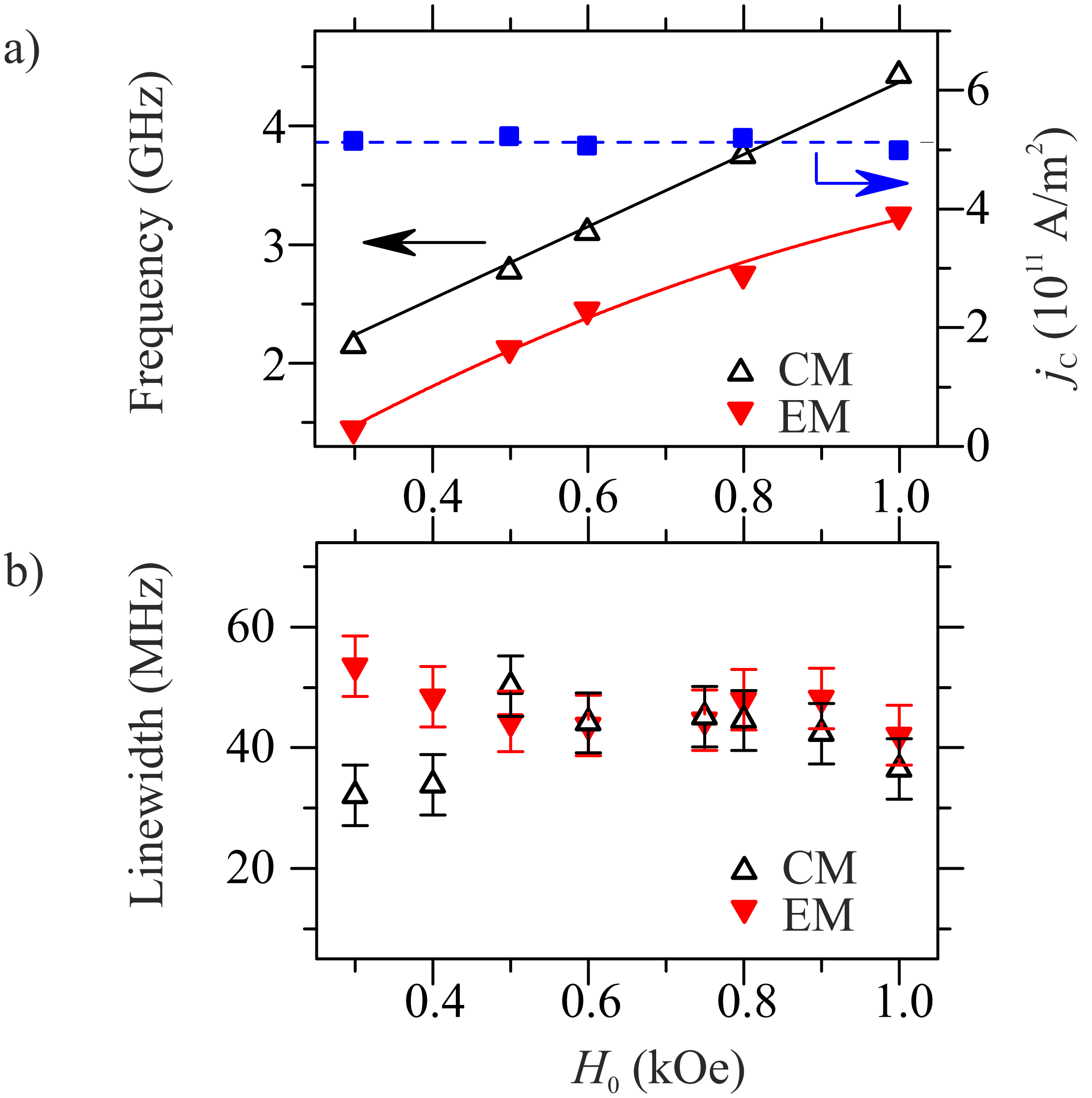

Fig. 4.17: a) Frequency of the edge mode (red down triangles) and the center mode (black up triangles) at the onset of auto-oscillations and the current density at the onset of the auto-oscillations j_c (blue squares) displayed against the static magnetic field. The blue dashed line marks the mean value current densities. The solid lines are guides to the eye.
b) Dependence of the spectral linewidth of the center mode (up triangles) and of the edge mode (down triangles) on the static magnetic field.

by Collet et.al. [28], for YIG films with a low Gilbert damping, an additional effect can contribute significantly to the relaxation rate – inhomogeneous broadening. This effect is independent of the applied static magnetic field and of the precession frequency of the examined spin-wave mode. For the measured range of magnetic fields the inhomogeneous broadening seems to dominate the relaxation frequency.
To further investigate this claim, high-resolution FMR-BLS measurements are performed. Therefore, the static magnetic field is rotated in plane by an angle of 5° with respect to the y-axis. Spin precession is excited by a microwave current in the Pt layer that is used as an antenna. Due to the small deviation from the purely perpendicular orientation, the mode structure in the nanowire remains nearly unchanged, while the Oersted field formed by the microwave current is oriented perpendicular to the wire axis and therefore contains a component perpendicular to the static magnetic field enabling inductive excitation of spin waves. From these measurements the linewidths of the fundamental edge and center mode are extracted. The results are shown in Fig. 4.17b). As for the onset current density, we see that no significant variation of the linewidth of both modes can be observed. Since the damping of a system and its linewidth are closely related, this confirms the previously made assumption: The natural damping of the system is not dominated by the Gilbert damping that depends on the magnitude of the applied static magnetic field, but by field independent inhomogeneous broadening effects as described in [28].

In conclusion, the experiments show that auto-oscillations can be excited in YIG films grown on top of a Pt layer patterned into a nanowire. The current density necessary to fully compensate the system's natural damping is $j_\mathrm{c} \approx 5.0\,\mathrm{A/m^2}$, which is comparable to the values found in previously demonstrated experiments for structures with a traditional growth order of GGG/YIG/Pt [28,43,44]. Since the growth of YIG directly on Pt is accompanied by an unavoidable enhancement of the system's natural damping, a comparable influence of SOT on the magnetic system indicates an improved transparency of the YIG/Pt interface for spin currents [84]. Additionally, it could be demonstrated that in the measured range of magnetic fields the natural damping is dominated by the field independent inhomogeneous broadening. Since the experiments show that an efficient YIG nano-oscillator can be grown on top of a Pt layer, these findings enable the possibility to utilize double sided spin injection and allow for more flexible designs.

4.4 Emission of coherently propagating spin waves by insulator-based spin-orbit torque oscillators

In the past years it could be demonstrated in metallic and insulating magnets that spin-orbit torques present an efficient mechanism to excite and control spin waves. A large variety of oscillator designs enabled the excitation of high amplitude auto-oscillations [19–22, 27, 43, 44, 47]. Other experiments allow for a precise control of the intensity of magnetic fluctuations [17, 18] and the propagation length of spin waves [44, 75–78]. Also the excitation of incoherently propagating spin waves via long distances was observed for subcritical driving currents [41, 42, 88–90]. Still, while this technique can be used to control the intensity at an output detection point, control mechanisms that rely on the phase of spin waves, need a coherent magnetization precession [8]. However, the excitation of coherently propating spin waves by SOT faces one major problem – self-localization. The high amplitude spin waves in the coherent auto-oscillation regime experience a strong nonlinear frequency red shift that prevents the propagation into the surrounding magnetic material, a phenomenon observed for metallic and insulating magnets [15, 19–22, 43, 47].

Accordingly, a mechanism is needed to overcome the nonlinear frequency shift in the auto-oscillation regime and therefore to avoid the effect of self-localization. Such a technique will be presented in this section. Here, the excitation of coherently propagating spin waves by spin-orbit torques in an extended Bi doped YIG film (BiYIG) with a pronounced perpendicular magnetic anisotropy (PMA) [91] is demonstrated [92]. A narrow Pt strip line on the film is used to locally compensate the natural damping of the system by SOT leading to the excitation coherent auto-oscillations. Due to the PMA of the BiYIG film, the shape anisotropy is compensated preventing a nonlinear frequency red shift that typically accompanies high-amplitude spin precessions. The absence of a frequency red shift enables the propagation of the coherently excited spin waves into the surrounding material. The detected critical current density necessary to excite auto-oscillations is comparable to the values demonstrated in the previous sections and the Gilbert damping of the free BiYIG film is only slightly increased with respect to undoped YIG films. Accordingly, Bi doped YIG films are a highly promising candidate for insulator based spintronics and magnonics, since the excitation of coherently propagating spin waves by SOT as demonstrated here allows for highly flexible designs.

4.4.1 Experimental setup

A schematic view of the experiment is shown in Fig 4.18. An extended Bi doped YIG film with PMA grown on a substituted GGG substrate (sGGG) was used as a magnetic medium. To enable excitation of spin waves by SOT, a Pt layer with a thickness of 6 nm is patterned into a strip line with a length of 4 µm, a width of 1 µm and two contact pads was grown on the magnetic film. The static magnetic field H_0 is applied perpendicular to the current direction I (spin-Hall geometry). The displayed configuration of current and magnetic field in Fig. 4.18 corresponds to the spin-wave amplification direction by SOT [17]. To minimize Joule heating, the current was applied in 500 ns long pulses with a repetition rate of 5 µs.

Sample fabrication The $\mathrm{Bi_1Y_2Fe_5O_{12}}$ (BiYIG) film is grown by pulsed laser deposition on a sGGG substrate using a frequency tripled YAG laser. The chosen concentration of Bi substitution induces a tensile strain in the YIG layer leading to a significant perpendicular magnetic anisotropy. A detailed description of the magnetic and structural properties can be found in [91].
The adjacent Pt strip line is patterned by optical lithography and lift-off of a sputtered Pt layer with a thickness of 6 nm. To be able to contact the strip line by wire bonding Ti/Au contacts are added to the Pt contact pads at the end of the strip line.

Magnetooptical measurements All magnetooptical measurements are performed using the µBLS setup with temporal resolution described in section 3.1.1. Due to the increased magnetooptical coupling for BiYIG in comparison with pure YIG [93–95], the probing laser is replaced by a diode pumped solid state laser with a wave length of $\lambda = 532\,\mathrm{nm}$ (green light)[1], since the improved visibility of green light simplifies alignment and working with the setup. The enhanced sensibility of blue light to magnetization dynamics in YIG [43] is not needed here, due to a sufficiently strong signal-to-noise ratio. The probing laser beam is focused through the substrate on the YIG surface into a diffraction limited spot. The laser power is chosen to be $P_\mathrm{L} = 0.1\,\mathrm{mW}$ to ensure for negligible heating of the magnetic material by absorption of light.

4.4.2 Determination of the perpendicular magnetic anisotropy

In a first step, the strength of the PMA is determined. Therefore, the spectrum of thermally excited magnetic oscillations is detected at the position of a free (BiYIG) and a Pt covered (BiYIG/Pt) part of the film for different static magnetic fields. A representative data set is shown in 4.19a) for $H_0 = 2000\,\mathrm{Oe}$. To obtain the

---

[1] EXLSR-532-200-CDRH by Spectra Physics

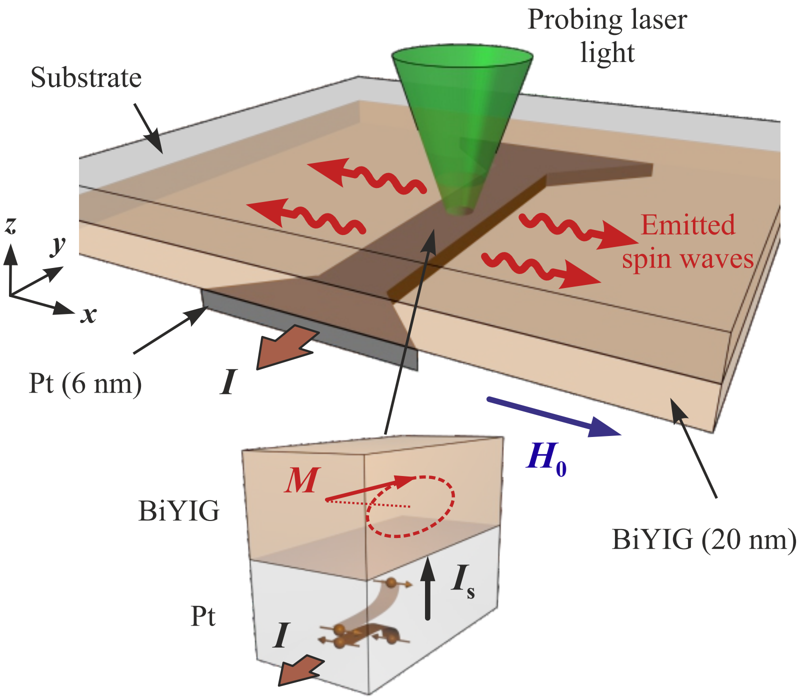

Fig. 4.18: Schematic view of the experimental setup. A Pt strip line with thickness of 6 nm, a width of 1 µm and a length of 4 µm is patterned on an extended 20 nm thick Bi doped YIG film. Sending an electric current through the Pt layer leads to the local excitation of coherent auto-oscillations below the Pt stripe and to the emission of coherently propagating spin waves into the surrounding material. The probing laser light is focused through the sGGG substrate onto the YIG surface. The inset shows a schematic view of the excitation of spin waves by SOT.

influence of the PMA on the precession frequency a modification to Kittel's equation is needed [96]:

$$\omega_0 = \gamma\sqrt{H_0(H_0 + (4\pi - N_\mathrm{a})M_\mathrm{s})} \tag{4.3}$$

where N_a is the magnetization independent anisotropy demagnetizing factor representing the PMA. To determine the effective magnetization $(4\pi - N_\mathrm{a})M_\mathrm{s}$ the frequency of the thermal fluctuation spectrum is displayed against the static magnetic field and a fit to the data is performed, using equation (4.3) (see Fig. 4.19b)). The

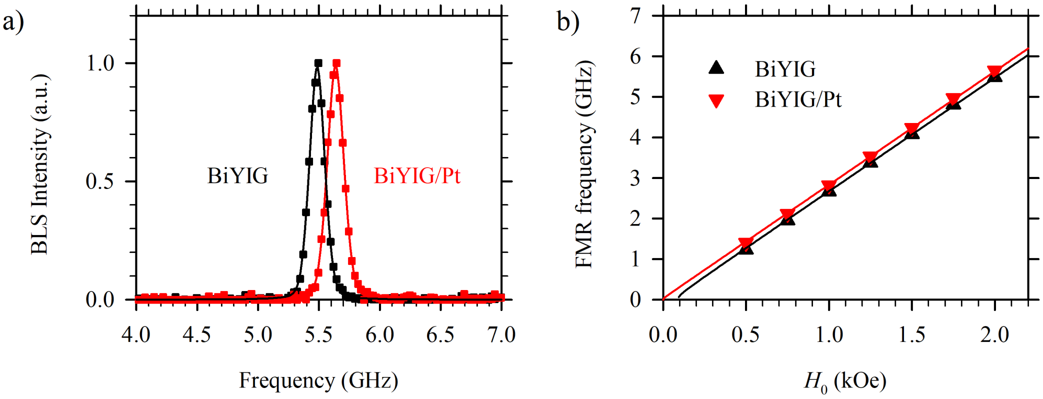

Fig. 4.19: a) BLS spectrum caused by thermal magnetic fluctuations in an extended free BiYIG film (black squares) and a BiYIG/Pt bilayer (red squares). b) The center frequency of the BLS spectrum displayed against the static magnetic field for an extended free BiYIG film (black up triangles) and a BiYIG/Pt bilayer (red down triangles). The solid curves are fits to the data using a modified Kittel equation by taking into account the PMA (see equation (4.3)).

effective magnetization is determined to be

$$(4\pi - N_{\mathrm{a}}^{\mathrm{free}})M_{\mathrm{s}} = -90\,\mathrm{G} \qquad \text{and} \qquad (4\pi - N_{\mathrm{a}}^{\mathrm{Pt}})M_{\mathrm{s}} = 20\,\mathrm{G}, \tag{4.4}$$

revealing a nearly magnetization independent precession frequency with $N_{\mathrm{a}} \approx 4\pi$. The small deviation between the determined values for a free and a Pt covered film is caused by a surface anisotropy at the BiYIG/Pt interface that partly compensates the strain induced PMA. Additionally, the anisotropy field is determined by

$$H_{\mathrm{a}} = N_{\mathrm{a}}M_{\mathrm{s}}. \tag{4.5}$$

Since the saturation magnetization is basically unaffected by the Bi doping [91], the anisotropy field can be extracted by using $4\pi M_{\mathrm{s}} = 1750\,\mathrm{G}$ for YIG:

$$H_{\mathrm{a}}^{\mathrm{free}} = 1840\,\mathrm{Oe} \qquad \text{and} \qquad H_{\mathrm{a}}^{\mathrm{Pt}} = 1730\,\mathrm{Oe}. \tag{4.6}$$

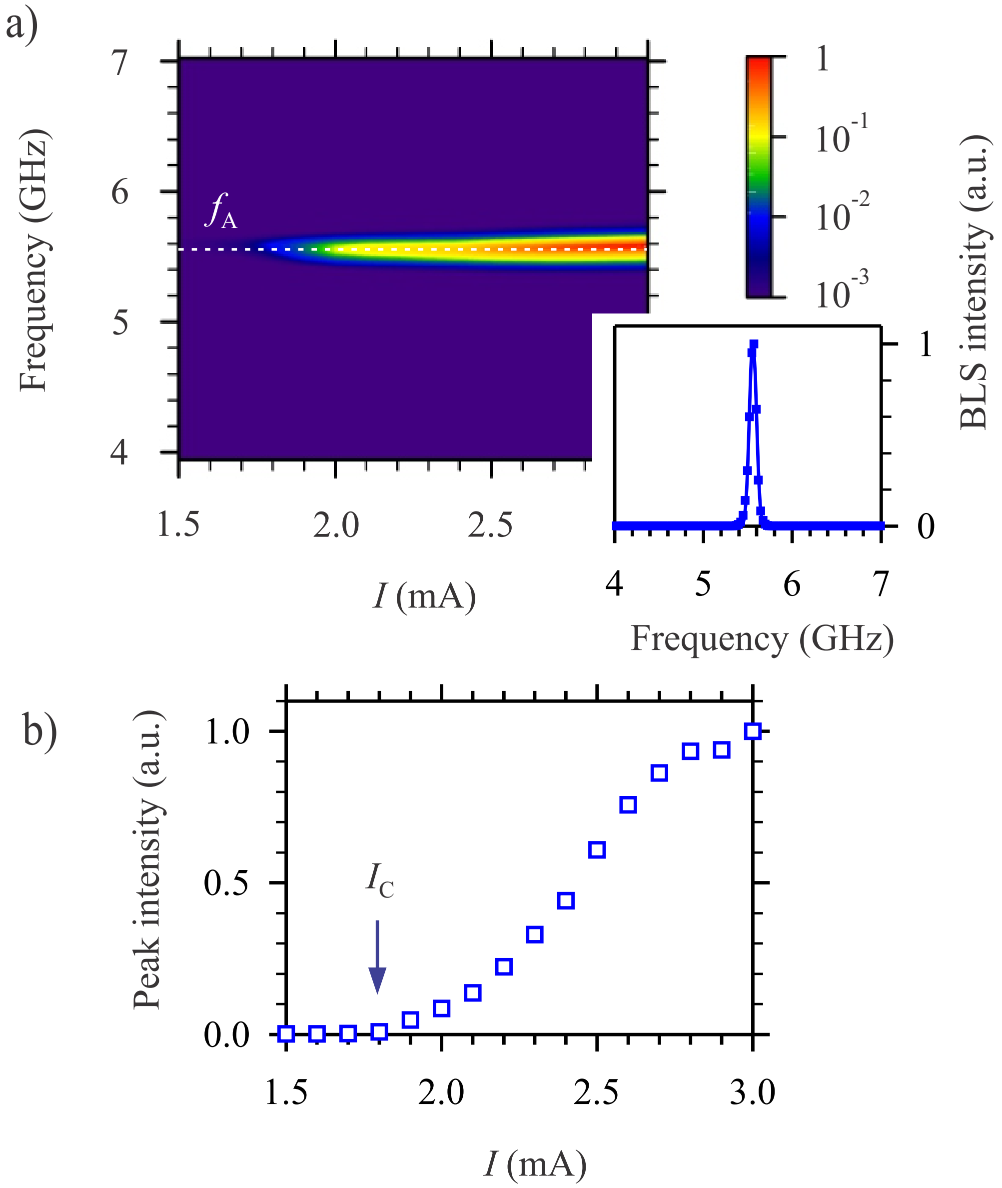

Fig. 4.20: a) Color map of the BLS spectrum recorded at the center of the Pt strip line in dependence of the applied electric current. The inset shows a representative spectrum at $I = 2.5\,\text{mA}$.
b) Current dependence of the peak BLS intensity.
All data was measured for $H_0 = 2000\,\text{Oe}$.

4.4.3 Excitation of localized auto-oscillations driven by spin-orbit torques

In Fig. 4.20a) the BLS spectrum recorded at the center of the Pt strip line is displayed against the electric current. At $I_c = 1.8\,\mathrm{mA}$ a strong increment of the detected BLS intensity can be observed marking the point of full damping compensation and the onset of auto-oscillations. This becomes even more evident, if we take a look at the peak BLS intensity (see Fig. 4.20b)). The found critical current corresponds to a current density of $j_c = 3 \times 10^{11}\,\mathrm{A/m^2}$, which is in good agreement with the values found for undoped YIG films [28, 43, 44, 47]. It can be seen, that for $I > I_c$ the BLS intensity caused by spin waves monotonously increases. In contrast to previously made experiments with undoped YIG or metallic structures [15, 19–22, 43, 47, 55], this increment of the BLS intensity is only accompanied by a tiny reduction of the precession frequency, which remains mainly unchanged in the entire measured current range (see Fig. 4.20a)). For a static magnetic field of $H_0 = 2000\,\mathrm{Oe}$, the auto-oscillation frequency is found to be $f_A = 5.56\,\mathrm{GHz}$, while for purely thermal fluctuations the precession frequency measured for the determination of the PMA is $f_0 = 5.63\,\mathrm{GHz}$. Accordingly, no significant frequency red shift due to nonlinear effects or due to Joule heating can be observed, as expected for the weak dependence on the static magnetization.

4.4.4 Coherently propagating spin waves excited by spin-orbit torques

Since the main mechanism for self-localization of spin waves in the auto-oscillation regime is the nonlinear frequency shift, the BiYIG film should not prevent spreading of the spin waves induced by SOT into the surrounding material. To investigate this hypothesis, two dimensional mapping of the BiYIG film is performed rastering the laser spot in the lateral directions. Centered with respect to the Pt strip line a $20 \times 7\,\mathrm{\mu m}$ area is scanned using a step size of $500\,\mathrm{nm}$ in both directions. The resulting map of the BLS intensity for an electric current of $I = 2.5\,\mathrm{mA}$ is shown in Fig. 4.21a). It can be seen, that the coherently excited magnons are efficiently emitted in all lateral directions of the BiYIG film. To gain a better understanding of the propagating spin waves that are free of the influence of SOT, the spatial dependence of the BLS intensity in the x direction is shown in Fig. 4.21b). The dashed lines frame the Pt stripe. The detected intensity follows a well-defined exponential decay (note logarithmic scale) as expected for propagating waves. From a fit to the data, the average propagation length – determined as the mean value of the propagation length on both sides of the Pt stripe – is found to be $\sigma = 3.7\,\mathrm{\mu m}$.

Additionally, the group velocity v_g can be determined from the temporally resolved

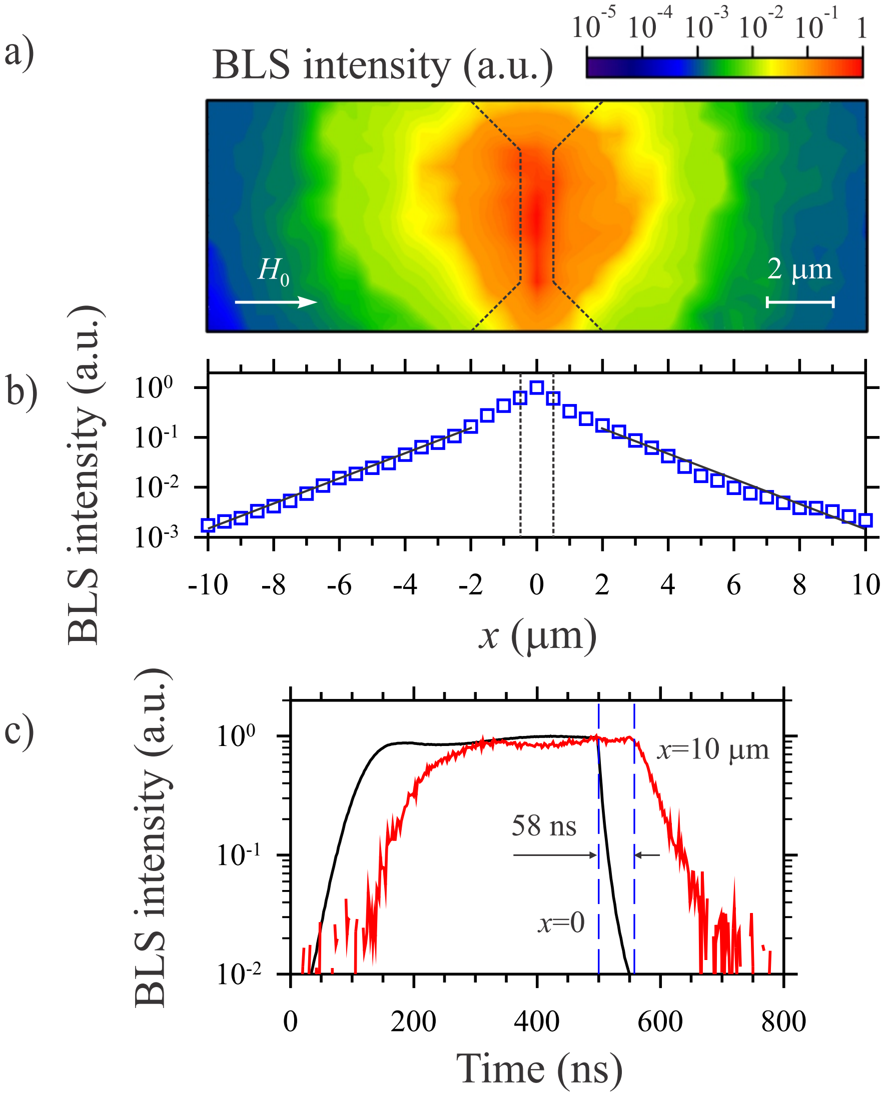

Fig. 4.21: a) Representative 2D mapping of the BLS intensity around the center of the Pt strip line recorded by rastering the probing laser spot in the lateral dimensions in a $20 \times 7\,\mu\mathrm{m}$ area with a step size of 500 nm. The dashed lines frame the region covered by Pt.
b) x-coordinate dependence of the normalized BLS intensity in the log-linear scale. The dashed lines frame the Pt strip line. The solid curves are exponential fits to the data at $|x| \geq 2\,\mu\mathrm{m}$.
c) Temporal dependence of the BLS intensity recorded at $x = 0$ (black curve) and $x = 10\,\mu\mathrm{m}$ (red curve). The dashed lines mark the beginning of the pulse decline that is used to determine group velocity of the propagating spin waves.
The presented data is recorded at a current of $I = 2.5\,\mathrm{mA}$ and a magnetic field of $H_0 = 2000\,\mathrm{Oe}$.

BLS intensity at $x = 0$ and $x = 10\,\mu\text{m}$ (see Fig. 4.21c)). For this purpose, the right flanks of the detected pulses are compared. The temporal shift between the two flanks at $x = 0$ and $x = 10\,\mu\text{m}$ is $58 \pm 6\,\text{ns}$ corresponding to a group velocity of $v_\text{g} = 0.17 \pm 0.02\,\mu\text{m/ns}$. The left edge is not functional for this type of analysis, since it demonstrates a smooth increment with time, due to the finite reaction time of magnetic system to the presence of SOT. Accordingly, a sharp definition of the temporal shift is not possible.

4.4.5 Theoretical analysis of spin-wave spectra

To gain a deeper understanding of the propagating waves, analytical calculations are performed using the anisotropy field for the free film as determined above. The dispersion relations for spin waves propagating parallel ($\varphi = 0°$) and perpendicular ($\varphi = 90°$) to the static magnetic field – calculated following the theory by Kalinikos et.al. [96] – are shown in Fig. 4.22a). The dashed line marks the experimentally detected precession frequency of the auto-oscillations f_A. It can be seen, that f_A is located at frequencies that correspond to existing spin-wave states. Accordingly, the high spin-wave intensities do not prevent the propagation into the surrounding material. It is to be mentioned, that spectral states exist for all angles between the wave vector k and the static magnetic field H_0. To illustrate this fact, an iso-frequency curve of f_A with the corresponding wave vectors is shown in the inset of Fig. 4.22a). The existence of spectral states for spin waves propagating in every direction is in agreement with the experimental emission pattern. Additionally, the angular dependence of the wave length and the group velocity are shown in Fig. 4.22b). The smallest wave length is found to be $\lambda = 340\,\text{nm}$ for $\varphi = 0°$, while for the same angle the largest group velocity is determined, which is given by $v_\text{g} = 0.21\,\mu\text{m/ns}$. This is in reasonable agreement with the experimentally determined value of $v_\text{g} = 0.17 \pm 0.2\,\mu\text{m/ns}$, therefore confirming the validity of the calculations.

4.4.6 Discussion

Finally, the quality of the examined films, quantified by the Gilbert damping α, will be investigated. Therefore, the field dependence of the spin-wave propagation length σ and its inverse value – the decay constant (the imaginary part of the wave vector) – k'' are measured. The results are shown in Fig. 4.23a). While the propagation length continuously decreases with the static magnetic field, a linear increment of the decay constant can be observed. This linear slope is predicted by theory [6]:
To calculate k'' the quotient of the relaxation frequency ω_r and the group velocity has to be determined:

$$k'' = \frac{\omega_\text{r}}{v_\text{g}}. \tag{4.7}$$

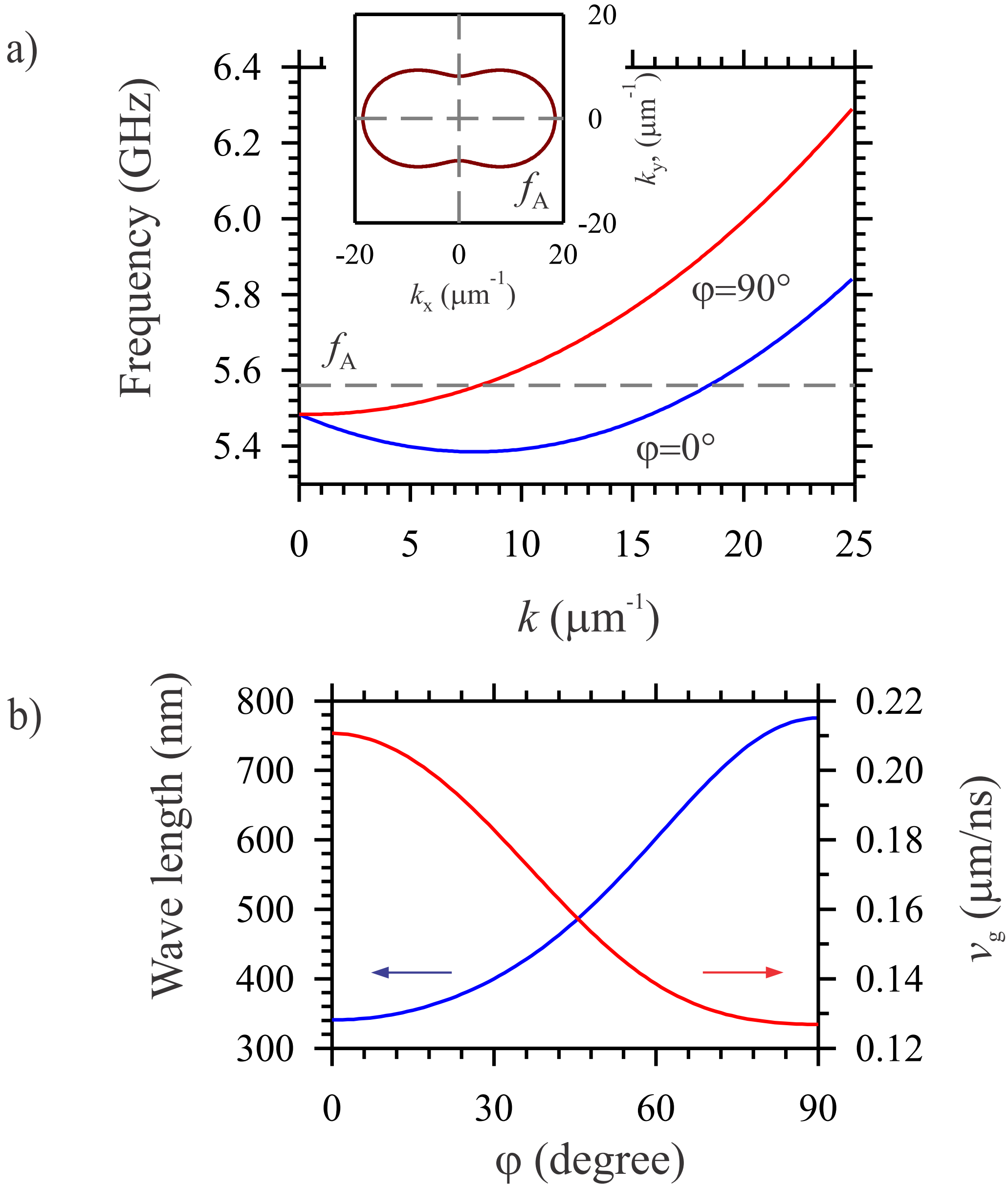

Fig. 4.22: a) Analytically calculated spin-wave spectrum for an extended free BiYIG film with the wave vector $\boldsymbol{k}$ parallel ($\varphi = 0°$, blue curve) and perpendicular ($\varphi = 90°$, red curve) to the static magnetic field. The dashed line marks the precession frequency f_A in the auto-oscillation regime. The inset displays an iso-frequency plane in the lateral wave vector plane.
b) Wave length (blue curve) and group velocity v_g (red curve) in dependence of the angle φ between the wave vector and the static magnetic field at the auto-oscillation frequency f_A.
All values are calculated for a static magnetic field of $H_0 = 2000\,\mathrm{Oe}$ and an experimentally determined effective PMA field of $H_\mathrm{a} = 1840\,\mathrm{Oe}$.

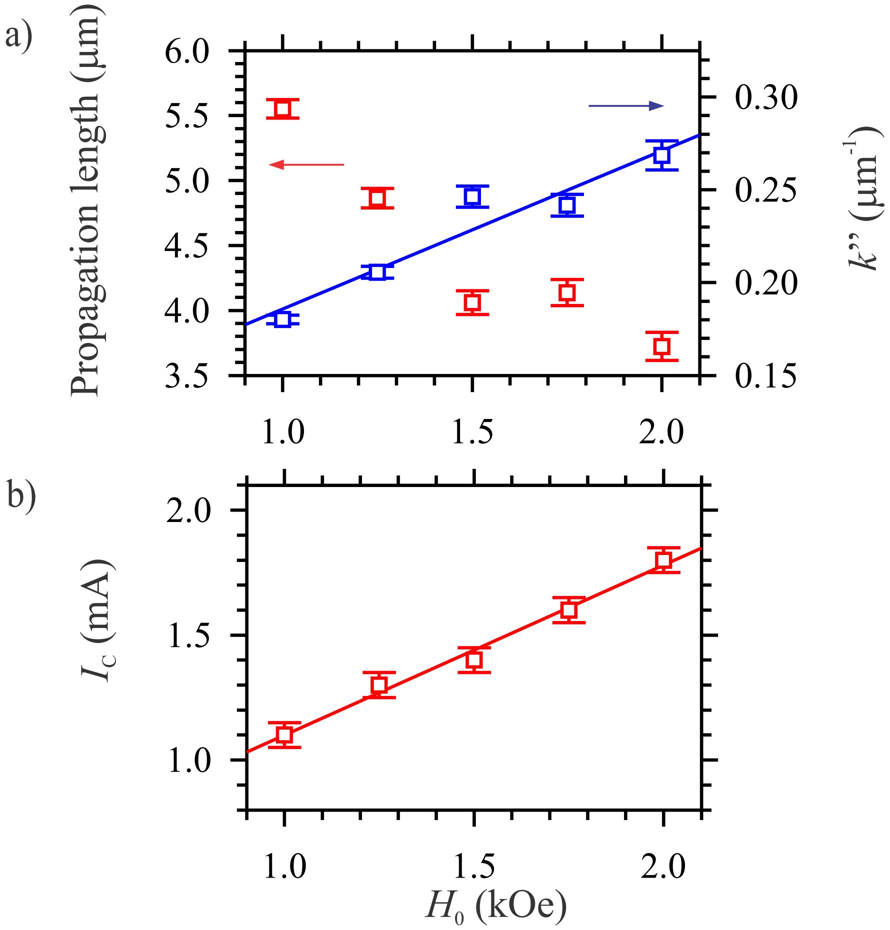

Fig. 4.23: a) Dependence of the propagation length (red squares) and the decay constant k'' (blue squares) on the static magnetic field H_0 in an extended free BiYIG film. The blue solid curve is a linear fit to the data of k''. The data were measured at a current of $I = 2.5\,\mathrm{mA}$.
b) Dependence of the critical electric current I_c on the static magnetic field H_0. The red solid line is a linear fit to the data.

As already demonstrated in section 4.3, for magnetic films with a low damping parameter the relaxation frequency can be significantly increased by a field independent inhomogeneous broadening ω_{r0}. Accordingly, equation (4.2) has to be slightly modified to

$$\omega_r = \omega_{r0} + \alpha\gamma H_0. \tag{4.8}$$

Combining equation (4.7) and (4.8) we get

$$k'' = \frac{\omega_{\mathrm{r0}}}{v_{\mathrm{g}}} + \alpha \frac{\gamma H_0}{v_{\mathrm{g}}}. \tag{4.9}$$

Since the group velocity was found to be nearly constant in the examined range of $H_0 = 1000 - 2000\,\mathrm{Oe}$, the Gilbert damping can be determined by a linear fit to the decay constant k'' (see Fig. 4.23a)) and we get $\alpha \approx 8.2 \times 10^{-4}$. This value is only slightly above the damping constant found for undoped YIG films of the same thickness [28, 97] and significantly smaller than for magnetic metals, making BiYIG a promising candidate for insulator-based magnonics. It is to be mentioned, that the found value of α is determined for a free Bi doped YIG film. For a BiYIG/Pt bilayer a significant enhancement is to be expected due to the presence of spin pumping. The Gilbert damping in the bilayer region can be determined from the onset current of the auto-oscillations. As for the relaxation frequency, a linear dependence of the critical current on the static magnetic field is predicted [54]

$$I_{\mathrm{c}} = \beta(\omega_{\mathrm{r0}} + \alpha_{\mathrm{YIG/Pt}} \cdot \gamma H_0) \tag{4.10}$$

with β as a proportionality coefficient representing the efficiency of SOT. The dependence of the critical current on the static magnetic field is displayed in Fig. 4.23b). By performing a linear fit to the data the Gilbert constant is determined to be $\alpha = 1.6 \times 10^{-3}$, which is very close to the value found for undoped YIG/Pt bilayers [28], therefore matching the good agreement between the onset current densities for YIG and BiYIG films.

In conclusion, the experiments show that the excitation of coherently propagating spin waves via spin-orbit torques can be realized in an extended Bi doped YIG film with a pronounced perpendicular magnetic anisotropy. Therefore, auto-oscillations are locally excited using a Pt strip line on a BiYIG film with a current density that is comparable to values reported for undoped YIG films. Due to the strong PMA, the shape anisotropy of the film is mainly compensated and the auto-oscillations are only accompanied by a negligible nonlinear frequency shift and no self-localization of the spin waves is observed. Instead, a propagation into the surrounding material is detected. Investigations of the critical current that leads to full compensation of the natural damping of the system, and of the propagation length of the spin waves in the extended BiYIG film demonstrate that the Gilbert damping of a Bi doped YIG film is not strongly increased with respect to an undoped film of identical thickness. The simple design demonstrated here allows for a high flexibility of possible SOT driven spin-wave emitters and should stimulate further research in this field.

5 Final discussion and conclusions

Finally, the obtained results will be discussed for each experimental study individually.

Direct observation of spin wave modes excited in a magnetic insulator

In section 4.1 ultrathin YIG/Pt bilayers patterned into nanodisks with a diameter of 2 µm and a YIG thickness of 20 nm were investigated. Electric contact was provided by gold contacts that overlap with the Pt layer, leaving a gap of uncovered Pt with a width of 1 µm. Due to the strong difference in the conductivity of Au and Pt, only within this gap a significant portion of the electric current flows through the Pt layer. Accordingly, only in this region – the active area – SOT act on the magnetization in the YIG disk. It could be shown experimentally and numerically that for currents below the point of full damping compensation, a potential well is formed in the gap by a joint effect of the reduction of the static magnetic field due to the presence of an Oersted field, a reduced damping in the gap mediated by SOT and a reduced magnetization due to Joule heating. The observed localized mode could be identified by simulations as a linear mode of comparable extend in all lateral directions. For electric currents above the compensation threshold, an enhancement of the current led to a spatial broadening of the excited mode within the gap until the entire active region was covered by auto-oscillations. This broadening process is caused by an efficient nonlinear mode coupling mediated by the low Gilbert damping in YIG. Accordingly, in contrast to metallic magnets, in ultrathin YIG films, there is no localized single mode to be observed in the auto-oscillation regime. Instead, a multimode auto-oscillation is excited by SOT that covers the entire active area.

High-efficiency control of spin-wave propagation in ultra-thin yttrium iron garnet by the spin-orbit torque

Section 4.2 presents the influence of SOT on inductively excited propagating spin waves in an ultrathin YIG/Pt bilayer waveguide. It could be shown that the dissipation in the magnetic system could be effectively controlled by SOT and even full compensation of the natural damping was observed, leading to the excitation of auto-oscillations in the entire waveguide. For electric currents below the compensation threshold, a precise tuning of the propagation length could be achieved and an increment of almost a factor of ten is observed. This enhancement corresponds

to a raise of the spin-wave intensity after propagating a distance of 10 µm – a relevant distance for technical applications – by three orders of magnitude. In future experiments, the enhancement could be further improved by decreasing the width of the waveguide to reduce Joule heating, that proved to be negative influence on the maximum achievable propagation length.
Still, at the critical current, an efficient scattering of inductively excited coherent spin waves from high amplitude spin waves exited by SOT was observed. For currents slightly above the compensation threshold, the propagation of inductively excited spin waves already was not measurable anymore. Accordingly, true amplification of propagating spin waves is not possible in the presented system. If this drawback can be overcome in the future, is yet to be understood.

Spin-orbit torque induced auto-oscillations in ultrathin YIG grown on Pt

The third experimental study in section 4.3 demonstrates the excitation of multimode auto-oscillations in a YIG/Pt nanowire, with the YIG layer grown directly on the Pt layer instead of the usually used GGG substrate. Typically, a GGG substrate is chosen due to the excellent matching of the lattice constants of YIG and GGG. Growing YIG on Pt is therefore inevitably accompanied by a reduction of the structural quality and therefore by an increased damping of the magnetization dynamics. In the experiments, the enhanced dissipation manifested in an increased linewidth with respect to the FMR FWHM found for YIG/Pt bilayers grown in the traditional order. Nevertheless, the critical current density needed to excite auto-oscillations is comparable to the values found for GGG/YIG/Pt structures with a similar YIG thickness, indicating an improved transparency of the YIG/Pt interface to spin currents for GGG/Pt/YIG samples. The successful demonstration of the functionality of a SOT driven YIG based nano-oscillator grown on Pt should stimulate further research since it allows for a higher flexibility of design with i.e. double sided spin-current injection, which is not possible if one YIG surface has to be grown directly on a GGG substrate.

Emission of coherently propagating spin waves by insulator-based spin-orbit torque oscillators

In section 4.4 the local excitation of coherent auto-oscillations by SOT in an extended Bi doped YIG film with an attached Pt strip line is presented. Due to the Bi doping, the YIG film is subject to a tensile strain that induces a strong PMA. The strength of the corresponding effective anisotropy field is sufficient to compensate the shape anisotropy of the extended film. As a consequence, the precession frequency only weakly depends on the static component of the magnetization vector. Accordingly, the excitation of high-amplitude auto-oscillations, that effectively reduces the static magnetization, only led to a weak nonlinear frequency shift. In previous experiments, frequency red shifts were sufficiently strong to excite auto-oscillations at frequencies below the spin-wave spectrum of the surrounding material, causing a self-localization of the excited spin waves. Since this was not the case here, the coherent auto-oscillations could propagate into the surrounding material. The threshold current density necessary to compensate the natural damping of the system is comparable to values found for undoped YIG/Pt bilayers, as is the Gilbert damping constant in the Pt covered region. For the free film, only a small increment of the Gilbert damping was observed in comparison with undoped YIG films of the same thickness. Accordingly, the demonstrated setup is an efficient emitter of coherently propagating spin waves driven by SOT, that allows for highly flexible designs in future applications, since no special geometry of the structure is needed to excite auto-oscillations.

In conclusion, the experimental studies performed for this project demonstrate that spin-orbit torques can be used to efficiently excite and control spin-waves in ultrathin YIG/Pt bilayers. The diversity of the presented oscillator designs reveals a huge flexibility in potential future applications and should stimulate further research. Especially the excitation of coherently propagating spin waves in Bi doped YIG films by SOT, that does not require any restricting geometry of the magnetic layer or inductive excitation techniques, opens new possibilities.

Bibliography

[1] S. A. Wolf, D. D. Awschalom, R. A. Buhrman, J. M. Daughton, S. von Molnár, M. L. Roukes, A. Y. Chtchelkanova, and D. M. Treger, “Spintronics: A spin-based electronics vision for the future,” *Science*, vol. 294, p. 1488, Nov 2001.

[2] D. Grundler, “Spintronics,” *Physics World*, vol. 15, no. 4, p. 39, 2002.

[3] M. N. Baibich, J. M. Broto, A. Fert, F. N. Van Dau, F. Petroff, P. Etienne, G. Creuzet, A. Friederich, and J. Chazelas, “Giant magnetoresistance of (001)Fe/(001)Cr magnetic superlattices,” *Phys. Rev. Lett.*, vol. 61, pp. 2472–2475, Nov 1988.

[4] G. Binasch, P. Grünberg, F. Saurenbach, and W. Zinn, “Enhanced magnetoresistance in layered magnetic structures with antiferromagnetic interlayer exchange,” *Phys. Rev. B*, vol. 39, pp. 4828–4830, Mar 1989.

[5] V. V. Kruglyak, S. O. Demokritov, and D. Grundler, “Magnonics,” *Journal of Physics D: Applied Physics*, vol. 43, no. 26, p. 264001, 2010.

[6] A. Gurevich and G. Melkov, *Magnetization Oscillations and Waves.* CRC Press, 1996.

[7] F. Bloch, “Zur Theorie des Ferromagnetismus,” *Zeitschrift für Physik*, vol. 61, no. 3, pp. 206–219, 1930.

[8] A. V. Chumak, V. I. Vasyuchka, A. A. Serga, and B. Hillebrands, “Magnon spintronics,” *Nature Physics*, vol. 11, pp. 453 EP –, Jun 2015. Review Article.

[9] J. H. E. Griffiths, “Anomalous high-frequency resistance of ferromagnetic metals,” *Nature*, vol. 158, pp. 670 EP –, Nov 1946.

[10] V. E. Demidov, M. P. Kostylev, K. Rott, P. Krzysteczko, G. Reiss, and S. O. Demokritov, “Excitation of microwaveguide modes by a stripe antenna,” *Applied Physics Letters*, vol. 95, no. 11, p. 112509, 2009.

[11] V. E. Demidov and S. O. Demokritov, “Magnonic waveguides studied by microfocus brillouin light scattering,” *IEEE Transactions on Magnetics*, vol. 51, pp. 1–15, April 2015.

[12] J. C. Slonczewski, “Current-driven excitation of magnetic multilayers,” *Journal of Magnetism and Magnetic Materials*, vol. 159, no. 1, pp. L1–L7, 1996.

[13] L. Berger, “Emission of spin waves by a magnetic multilayer traversed by a current,” *Phys. Rev. B*, vol. 54, pp. 9353–9358, Oct 1996.

[14] M. Tsoi, A. G. M. Jansen, J. Bass, W.-C. Chiang, M. Seck, V. Tsoi, and P. Wyder, “Excitation of a magnetic multilayer by an electric current,” *Phys. Rev. Lett.*, vol. 80, pp. 4281–4284, May 1998.

[15] V. E. Demidov, S. Urazhdin, G. de Loubens, O. Klein, V. Cros, A. Anane, and S. O. Demokritov, “Magnetization oscillations and waves driven by pure spin currents,” *Physics Reports*, vol. 673, pp. 1–31, 2017.

[16] A. Hoffmann, “Spin Hall effects in metals,” *IEEE Transactions on Magnetics*, vol. 49, no. 10, pp. 5172–5193, 2013.

[17] V. E. Demidov, S. Urazhdin, E. R. J. Edwards, M. D. Stiles, R. D. McMichael, and S. O. Demokritov, “Control of magnetic fluctuations by spin current,” *Phys. Rev. Lett.*, vol. 107, p. 107204, Sep 2011.

[18] V. E. Demidov, S. Urazhdin, E. R. J. Edwards, and S. O. Demokritov, “Wide-range control of ferromagnetic resonance by spin Hall effect,” *Applied Physics Letters*, vol. 99, p. 172501, Oct 2011.

[19] V. E. Demidov, S. Urazhdin, H. Ulrichs, V. Tiberkevich, A. Slavin, D. Baither, G. Schmitz, and S. O. Demokritov, “Magnetic nano-oscillator driven by pure spin current,” *Nature Materials*, Oct 2012.

[20] L. Liu, C.-F. Pai, D. C. Ralph, and R. A. Buhrman, “Magnetic oscillations driven by the spin Hall effect in 3-terminal magnetic tunnel junction devices,” *Phys. Rev. Lett.*, vol. 109, p. 186602, Oct 2012.

[21] V. E. Demidov, S. Urazhdin, A. Zholud, A. V. Sadovnikov, and S. O. Demokritov, “Nanoconstriction-based spin-Hall nano-oscillator,” *Applied Physics Letters*, vol. 105, no. 17, p. 172410, 2014.

[22] Z. Duan, A. Smith, L. Yang, B. Youngblood, J. Lindner, V. E. Demidov, S. O. Demokritov, and I. N. Krivorotov, “Nanowire spin torque oscillator driven by spin orbit torques,” *Nature Communications*, vol. 5, pp. 5616 EP –, Dec 2014. Article.

[23] B. Divinskiy, V. E. Demidov, S. Urazhdin, R. Freeman, A. B. Rinkevich, and S. O. Demokritov, “Excitation and amplification of spin waves by spin-orbit torque,” *Advanced Materials*, p. 1802837, 2018.

[24] Y. Sun, Y.-Y. Song, H. Chang, M. Kabatek, M. Jantz, W. Schneider, M. Wu, H. Schultheiss, and A. Hoffmann, "Growth and ferromagnetic resonance properties of nanometer-thick yttrium iron garnet films," *Applied Physics Letters*, vol. 101, p. 152405, Oct 2012.

[25] O. d'Allivy Kelly, A. Anane, R. Bernard, J. Ben Youssef, C. Hahn, A. H. Molpeceres, C. Carrétéro, E. Jacquet, C. Deranlot, P. Bortolotti, R. Lebourgeois, J.-C. Mage, G. de Loubens, O. Klein, V. Cros, and A. Fert, "Inverse spin hall effect in nanometer-thick yttrium iron garnet/Pt system," *Applied Physics Letters*, vol. 103, no. 8, p. 082408, 2013.

[26] H. Yu, O. d'Allivy Kelly, V. Cros, R. Bernard, P. Bortolotti, A. Anane, F. Brandl, R. Huber, I. Stasinopoulos, and D. Grundler, "Magnetic thin-film insulator with ultra-low spin wave damping for coherent nanomagnonics," *Scientific Reports*, vol. 4, pp. 6848 EP –, Oct 2014. Article.

[27] A. Hamadeh, O. d'Allivy Kelly, C. Hahn, H. Meley, R. Bernard, A. H. Molpeceres, V. V. Naletov, M. Viret, A. Anane, V. Cros, S. O. Demokritov, J. L. Prieto, M. Muñoz, G. de Loubens, and O. Klein, "Full control of the spin-wave damping in a magnetic insulator using spin-orbit torque," *Phys. Rev. Lett.*, vol. 113, p. 197203, Nov 2014.

[28] M. Collet, X. de Milly, O. d'Allivy Kelly, V. V. Naletov, R. Bernard, P. Bortolotti, J. Ben Youssef, V. E. Demidov, S. O. Demokritov, J. L. Prieto, M. Muñoz, V. Cros, A. Anane, G. de Loubens, and O. Klein, "Generation of coherent spin-wave modes in yttrium iron garnet microdiscs by spin-orbit torque," *Nature Communications*, vol. 7, pp. 10377 EP –, Jan 2016. Article.

[29] C. Herring and C. Kittel, "On the theory of spin waves in ferromagnetic media," *Phys. Rev.*, vol. 81, pp. 869–880, Mar 1951.

[30] L. Landau and E. Lifshitz, "On the theory of the dispersion of magnetic permeability in ferromagnetic bodies," *Phys. Z. Sowietunion*, vol. 8, pp. 153–169, 1935.

[31] V. Demidov and S. Demokritov, "Einführung in die Magnonik," 2014. Lecture at Westfälische Wilhelms-Universität Münster.

[32] T. Gilbert, "A Lagrangian formulation of the gyromagnetic equation of the magnetization field," *Phys. Rev.*, vol. 100, p. 1243, 1955. [Abstract only; full report, Armor Research Foundation Project No. A059, Supplementary Report, May 1, 1956].

[33] T. Gilbert, "A Phenomenological Theory of Damping in Ferromagnetic Materials," *IEEE Trans. Magn.*, vol. 40, pp. 3443–3449, Nov. 2004.

[34] W. Heisenberg, "Zur Theorie des Ferromagnetismus," *Z. Phys.*, vol. 49, no. 9-10, pp. 619–636, 1928.

[35] T. Holstein and H. Primakoff, "Field dependence of the intrinsic domain magnetization of a ferromagnet," *Phys. Rev.*, vol. 58, pp. 1098–1113, Dec 1940.

[36] R. I. Joseph and E. Schlömann, "Demagnetizing field in nonellipsoidal bodies," *Journal of Applied Physics*, vol. 36, no. 5, pp. 1579–1593, 1965.

[37] C. Kittel, "On the Theory of Ferromagnetic Resonance Absorption," *Phys. Rev.*, vol. 73, pp. 155–161, Jan. 1948.

[38] B. A. K. Slavin and A. N., "Theory of dipole-exchange spin wave spectrum for ferromagnetic films with mixed exchange boundary conditions," *Journal of Physics C: Solid State Physics*, vol. 19, no. 35, p. 7013, 1986.

[39] R. Damon and J. Eshbach, "Magnetostatic modes of a ferromagnet slab," *J. Phys. Chem. Solids*, vol. 19, no. 3-4, pp. 308 – 320, 1961.

[40] V. Cherepanov, I. Kolokolov, and V. L'vov, "The saga of YIG: Spectra, thermodynamics, interaction and relaxation of magnons in a complex magnet," *Physics Reports*, vol. 229, no. 3, pp. 81 – 144, 1993.

[41] S. T. B. Goennenwein, R. Schlitz, M. Pernpeintner, K. Ganzhorn, M. Althammer, R. Gross, and H. Huebl, "Non-local magnetoresistance in YIG/Pt nanostructures," *Applied Physics Letters*, vol. 107, p. 172405, Oct 2015.

[42] L. J. Cornelissen, K. J. H. Peters, G. E. W. Bauer, R. A. Duine, and B. J. van Wees, "Magnon spin transport driven by the magnon chemical potential in a magnetic insulator," *Phys. Rev. B*, vol. 94, p. 014412, Jul 2016.

[43] V. E. Demidov, M. Evelt, V. Bessonov, S. O. Demokritov, J. L. Prieto, M. Muñoz, J. Ben Youssef, V. V. Naletov, G. de Loubens, O. Klein, M. Collet, P. Bortolotti, V. Cros, and A. Anane, "Direct observation of dynamic modes excited in a magnetic insulator by pure spin current," *Scientific Reports*, vol. 6, pp. 32781 EP –, Sep 2016. Article.

[44] M. Evelt, V. E. Demidov, V. Bessonov, S. O. Demokritov, J. L. Prieto, M. Muñoz, J. Ben Youssef, V. V. Naletov, G. de Loubens, O. Klein, M. Collet, K. Garcia-Hernandez, P. Bortolotti, V. Cros, and A. Anane, "High-efficiency control of spin-wave propagation in ultra-thin yttrium iron garnet by the spin-orbit torque," *Applied Physics Letters*, vol. 108, no. 17, p. 172406, 2016.

[45] V. Lauer, M. Schneider, T. Meyer, C. Dubs, P. Pirro, T. Brächer, F. Heussner, B. Lägel, V. Vasyuchka, A. Serga, B. Hillebrands, and A. Chumak, "Auto-oscillations in YIG/Pt microstructures driven by the spin seebeck effect," *arXiv:1612.07305*, Dec 2016.

[46] C. Safranski, I. Barsukov, H. K. Lee, T. Schneider, A. A. Jara, A. Smith, H. Chang, K. Lenz, J. Lindner, Y. Tserkovnyak, M. Wu, and I. N. Krivorotov, "Spin caloritronic nano-oscillator," *Nature Communications*, vol. 8, no. 1, p. 117, 2017.

[47] M. Evelt, C. Safranski, M. Aldosary, V. E. Demidov, I. Barsukov, A. P. Nosov, A. B. Rinkevich, K. Sobotkiewich, X. Li, J. Shi, I. N. Krivorotov, and S. O. Demokritov, "Spin Hall-induced auto-oscillations in ultrathin YIG grown on Pt," *Scientific Reports*, vol. 8, no. 1, p. 1269, 2018.

[48] K. Y. Guslienko, S. O. Demokritov, B. Hillebrands, and A. N. Slavin, "Effective dipolar boundary conditions for dynamic magnetization in thin magnetic stripes," *Phys. Rev. B*, vol. 66, p. 132402, Oct 2002.

[49] A. V. Khvalkovskiy, V. Cros, D. Apalkov, V. Nikitin, M. Krounbi, K. A. Zvezdin, A. Anane, J. Grollier, and A. Fert, "Matching domain-wall configuration and spin-orbit torques for efficient domain-wall motion," *Phys. Rev. B*, vol. 87, p. 020402, Jan 2013.

[50] E. Saitoh, M. Ueda, H. Miyajima, and G. Tatara, "Conversion of spin current into charge current at room temperature: Inverse spin-Hall effect," *Applied Physics Letters*, vol. 88, p. 182509, May 2006.

[51] H. Kurebayashi, O. Dzyapko, V. E. Demidov, D. Fang, A. J. Ferguson, and S. O. Demokritov, "Controlled enhancement of spin-current emission by three-magnon splitting," *Nature Materials*, vol. 10, pp. 660 EP –, Jul 2011.

[52] T. Kimura, Y. Otani, T. Sato, S. Takahashi, and S. Maekawa, "Room-temperature reversible spin Hall effect," *Phys. Rev. Lett.*, vol. 98, p. 156601, Apr 2007.

[53] A. D. Kent and D. C. Worledge, "A new spin on magnetic memories," *Nature Nanotechnology*, vol. 10, pp. 187 EP –, Mar 2015.

[54] A. Slavin and V. Tiberkevich, "Nonlinear auto-oscillator theory of microwave generation by spin-polarized current," *IEEE Transactions on Magnetics*, vol. 45, pp. 1875–1918, April 2009.

[55] V. E. Demidov, S. Urazhdin, A. Zholud, A. V. Sadovnikov, A. N. Slavin, and S. O. Demokritov, "Spin-current nano-oscillator based on nonlocal spin injection," *Scientific Reports*, vol. 5, pp. 8578 EP –, Feb 2015. Article.

[56] A. Slavin and V. Tiberkevich, “Excitation of spin waves by spin-polarized current in magnetic nano-structures,” *IEEE Transactions on Magnetics*, vol. 44, pp. 1916–1927, July 2008.

[57] K. Uchida, S. Takahashi, K. Harii, J. Ieda, W. Koshibae, K. Ando, S. Maekawa, and E. Saitoh, “Observation of the spin Seebeck effect,” *Nature*, vol. 455, no. 7214, pp. 778 – 781, 2008.

[58] A. Kehlberger, U. Ritzmann, D. Hinzke, E.-J. Guo, J. Cramer, G. Jakob, M. C. Onbasli, D. H. Kim, C. A. Ross, M. B. Jungfleisch, B. Hillebrands, U. Nowak, and M. Kläui, “Length scale of the spin Seebeck effect,” *Phys. Rev. Lett.*, vol. 115, p. 096602, Aug 2015.

[59] J. Xiao, G. E. W. Bauer, K.-c. Uchida, E. Saitoh, and S. Maekawa, “Theory of magnon-driven spin Seebeck effect,” *Phys. Rev. B*, vol. 81, p. 214418, Jun 2010.

[60] S. Demokritov, B. Hillebrands, and A. Slavin, “Brillouin light scattering studies of confined spin waves: linear and nonlinear confinement,” *Physics Reports*, vol. 348, no. 6, pp. 441 – 489, 2001.

[61] S. O. Demokritov and V. E. Demidov, “Micro-brillouin light scattering spectroscopy of magnetic nanostructures,” *IEEE Transactions on Magnetics*, vol. 44, pp. 6–12, Jan 2008.

[62] H. Ibach and H. Lï¿½th, *Festkörperphysik.* Springer, 7st ed., 2009.

[63] A. Borovik-Romanov and N. Kreines, “Brillouin-Mandelstam scattering from thermal and excited magnons,” *PHYSICS REPORTS (Review Section of Physics Letters)*, vol. 81, pp. 351–408, 1982.

[64] L. Landau and E. Lifshitz, *Electrodynamics of Continuous Media.* Oxford: Pergamon Press, 1960.

[65] V. E. Demidov, S. O. Demokritov, B. Hillebrands, M. Laufenberg, and P. P. Freitas, “Radiation of spin waves by a single micrometer-sized magnetic element,” *Applied Physics Letters*, vol. 85, no. 14, pp. 2866–2868, 2004.

[66] H. Ulrichs, *Spin-wave instabilities on the nanoscale.* PhD thesis, Westfälische Wilhelms-Universität, 2014.

[67] A. Vansteenkiste, J. Leliaert, M. Dvornik, M. Helsen, F. Garcia-Sanchez, and B. Van Waeyenberge, “The design and verification of MuMax3,” *AIP Advances*, vol. 4, no. 10, p. 107133, 2014.

[68] A. Vansteenkiste and B. Van de Wiele, “MuMax: a new high-performance micromagnetic simulation tool,” *JOURNAL OF MAGNETISM AND MAGNETIC MATERIALS*, vol. 323, no. 21, pp. 2585–2591, 2011.

[69] G. Gubbiotti, G. Carlotti, T. Okuno, M. Grimsditch, L. Giovannini, F. Montoncello, and F. Nizzoli, “Spin dynamics in thin nanometric elliptical Permalloy dots: A Brillouin light scattering investigation as a function of dot eccentricity,” *Phys. Rev. B*, vol. 72, p. 184419, Nov 2005.

[70] A. Slavin and V. Tiberkevich, “Spin wave mode excited by spin-polarized current in a magnetic nanocontact is a standing self-localized wave bullet,” *Phys. Rev. Lett.*, vol. 95, p. 237201, Nov 2005.

[71] H. Suhl, “The theory of ferromagnetic resonance at high signal powers,” *Journal of Physics and Chemistry of Solids*, vol. 1, no. 4, pp. 209 – 227, 1957.

[72] C. Kittel, *Introduction to Solid State Phyics.* Wiley, 1953.

[73] V. E. Demidov, U.-H. Hansen, and S. O. Demokritov, “Spin-wave eigenmodes of a saturated magnetic square at different precession angles,” *Phys. Rev. Lett.*, vol. 98, p. 157203, Apr 2007.

[74] S. Urazhdin, V. E. Demidov, H. Ulrichs, T. Kendziorczyk, T. Kuhn, J. Leuthold, G. Wilde, and S. O. Demokritov, “Nanomagnonic devices based on the spin-transfer torque,” *Nature Nanotechnology*, vol. 9, pp. 509 EP –, May 2014.

[75] K. An, D. R. Birt, C.-F. Pai, K. Olsson, D. C. Ralph, R. A. Buhrman, and X. Li, “Control of propagating spin waves via spin transfer torque in a metallic bilayer waveguide,” *Phys. Rev. B*, vol. 89, p. 140405, Apr 2014.

[76] V. E. Demidov, S. Urazhdin, A. B. Rinkevich, G. Reiss, and S. O. Demokritov, “Spin Hall controlled magnonic microwaveguides,” *Applied Physics Letters*, vol. 104, p. 152402, Apr 2014.

[77] Z. Wang, Y. Sun, M. Wu, V. Tiberkevich, and A. Slavin, “Control of spin waves in a thin film ferromagnetic insulator through interfacial spin scattering,” *Phys. Rev. Lett.*, vol. 107, p. 146602, Sep 2011.

[78] E. Padrón-Hernández, A. Azevedo, and S. M. Rezende, “Amplification of spin waves in yttrium iron garnet films through the spin Hall effect,” *Applied Physics Letters*, vol. 99, p. 192511, Nov 2011.

[79] C. Tang, M. Aldosary, Z. Jiang, H. Chang, B. Madon, K. Chan, M. Wu, J. E. Garay, and J. Shi, “Exquisite growth control and magnetic properties of yttrium iron garnet thin films,” *Applied Physics Letters*, vol. 108, p. 102403, Mar 2016.

[80] C. Hauser, T. Richter, N. Homonnay, C. Eisenschmidt, M. Qaid, H. Deniz, D. Hesse, M. Sawicki, S. G. Ebbinghaus, and G. Schmidt, "Yttrium Iron Garnet thin films with very low damping obtained by recrystallization of amorphous material," *Scientific Reports*, vol. 6, pp. 20827 EP –, Feb 2016. Article.

[81] M. Aldosary, J. Li, C. Tang, Y. Xu, J.-G. Zheng, K. N. Bozhilov, and J. Shi, "Platinum/yttrium iron garnet inverted structures for spin current transport," *Applied Physics Letters*, vol. 108, p. 242401, Jun 2016.

[82] P. Che, Y. Zhang, C. Liu, S. Tu, Z. Liao, D. Yu, F. A. Vetro, J. P. Ansermet, W. Zhao, L. Bi, and H. Yu, "Short-wavelength spin waves in yttrium iron garnet micro-channels on silicon," *IEEE Magnetics Letters*, vol. 7, pp. 1–4, 2016.

[83] J. Li, Y. Xu, M. Aldosary, C. Tang, Z. Lin, S. Zhang, R. Lake, and J. Shi, "Observation of magnon-mediated current drag in Pt/yttrium iron garnet/Pt(Ta) trilayers," *Nature Communications*, vol. 7, pp. 10858 EP –, Mar 2016. Article.

[84] W. Zhang, W. Han, X. Jiang, S.-H. Yang, and S. S. P. Parkin, "Role of transparency of platinum-ferromagnet interfaces in determining the intrinsic magnitude of the spin Hall effect," *Nature Physics*, vol. 11, pp. 496 EP –, Apr 2015. Article.

[85] Z. Duan, I. N. Krivorotov, R. E. Arias, N. Reckers, S. Stienen, and J. Lindner, "Spin wave eigenmodes in transversely magnetized thin film ferromagnetic wires," *Phys. Rev. B*, vol. 92, p. 104424, Sep 2015.

[86] V. E. Demidov, S. Urazhdin, B. Divinskiy, V. D. Bessonov, A. B. Rinkevich, V. V. Ustinov, and S. O. Demokritov, "Chemical potential of quasi-equilibrium magnon gas driven by pure spin current," *Nature Communications*, vol. 8, no. 1, p. 1579, 2017.

[87] J. C. Slonczewski, "Excitation of spin waves by an electric current," *Journal of Magnetism and Magnetic Materials*, vol. 195, no. 2, pp. L261–L268, 1999.

[88] L. J. Cornelissen, J. Liu, R. A. Duine, J. B. Youssef, and B. J. van Wees, "Long-distance transport of magnon spin information in a magnetic insulator at room temperature," *Nature Physics*, vol. 11, pp. 1022 EP –, Sep 2015.

[89] D. Wesenberg, T. Liu, D. Balzar, M. Wu, and B. L. Zink, "Long-distance spin transport in a disordered magnetic insulator," *Nature Physics*, vol. 13, pp. 987 EP –, Jul 2017. Article.

[90] N. Thiery, A. Draveny, V. V. Naletov, L. Vila, J. P. Attané, C. Beigné, G. de Loubens, M. Viret, N. Beaulieu, J. Ben Youssef, V. E. Demidov, S. O. Demokritov, A. N. Slavin, V. S. Tiberkevich, A. Anane, P. Bortolotti, V. Cros,

and O. Klein, “Nonlinear spin conductance of yttrium iron garnet thin films driven by large spin-orbit torque,” *Phys. Rev. B*, vol. 97, p. 060409, Feb 2018.

[91] L. Soumah, N. Beaulieu, L. Qassym, C. Carrïétéro, E. Jacquet, R. Lebourgeois, J. B. Youssef, P. Bortolotti, V. Cros, and A. Anane, “Ultra-low damping insulating magnetic thin films get perpendicular,” 2018.

[92] M. Evelt, L. Soumah, A. B. Rinkevich, S. O. Demokritov, A. Anane, V. Cros, J. B. Youssef, G. de Loubens, O. Klein, P. Bortolotti, and V. E. Demidov, “Emission of coherent propagating magnons by insulator-based spin-orbit torque oscillators,” 2018.

[93] J. M. Robertson, S. Wittekoek, T. J. A. Popma, and P. F. Bongers, “Preparation and optical properties of single crystal thin films of bismuth substituted iron garnets for magneto-optic applications,” *Applied physics*, vol. 2, no. 5, pp. 219–228, 1973.

[94] P. Hansen, K. Witter, and W. Tolksdorf, “Magnetic and magneto-optic properties of lead- and bismuth-substituted yttrium iron garnet films,” *Phys. Rev. B*, vol. 27, pp. 6608–6625, Jun 1983.

[95] K. Matsumoto, S. Sasaki, K. Haraga, K. Yamaguchi, T. Fujii, and Y. Asahara, “Enhancement of magneto-optical Faraday rotation by bismuth substitution in bismuth and aluminum substituted yttrium-iron-garnet single-crystal films grown by coating gels,” *Journal of Applied Physics*, vol. 71, pp. 2467–2469, Mar 1992.

[96] B. A. Kalinikos, M. P. Kostylev, N. V. Kozhus, and A. N. Slavin, “The dipole-exchange spin wave spectrum for anisotropic ferromagnetic films with mixed exchange boundary conditions,” *Journal of Physics: Condensed Matter*, vol. 2, no. 49, p. 9861, 1990.

[97] M. Collet, O. Gladii, M. Evelt, V. Bessonov, L. Soumah, P. Bortolotti, S. O. Demokritov, Y. Henry, V. Cros, M. Bailleul, V. E. Demidov, and A. Anane, “Spin-wave propagation in ultra-thin YIG based waveguides,” *Applied Physics Letters*, vol. 110, p. 092408, Feb 2017.

Danksagung

Abschließend möchte ich noch allen danken, die zum Gelingen dieses Projektes beigetragen haben.
Beginnen möchte ich mit Sergej O. Demokritov, zunächst dafür, dass er es mir ermöglicht hat, an diesem spannenden Thema zu arbeiten. Ich möchte ihm aber auch dafür danken, dass er mich zur Teilnahme an diversen Konferenzen motiviert hat und auch ansonsten ein stets hilfsbereiter, unkomplizierter sowie entgegenkommender Betreuer war.
Ein besonderer Dank gilt Vladislav E. Demidov, der mir jederzeit eine große Hilfe bei der Erfüllung all meiner Aufgaben war. Egal ob es um experimentelle Probleme, Verständnisfragen oder einfach darum ging, das weitere Vorgehen wieder auf Kurs bringen – Vlad war stets bereit, seine Arbeit zu unterbrechen, um mir weiterzuhelfen und dafür möchte ich mich an dieser Stelle ganz herzlich bedanken.
Auch meinem Büropartner Boris Divinskiy möchte ich für viele anregende Diskussionen – sei sie nun fachlicher oder sonstiger Natur – danken, die mir die Arbeit häufig erleichtert und den Büroalltag deutlich amüsanter gestaltet haben.
Melanie Kind, Yvonne Liebe und Diana Nordhaus danke ich für die Lösung diverser organisatorischer Probleme. Besonders in der Anfangszeit war diese Unterstützung sehr hilfreich, bei der Verwaltung von Dienstreisen, Urlauben, Bestellungen oder der Verlängerung meiner Verträge. Auch für zahlreiche, äußerst unterhaltsame Gespräche ein ganz herzliches Dankeschön.
An Mathis Weber geht ein großer Dank für die schnelle Beseitigung meiner Software- und Hardware-Probleme. Auch der regelmäßige Austausch von Indiana Jones- oder sonstigen Zitaten wird mir in Zukunft sehr fehlen.
An alle verbleibenden Mitarbeiter des Instituts vielen Dank für die angenehme Arbeitsatmosphäre und gute Zusammenarbeit.
Meiner Familie und meinen Freunden möchte ich für so manche Kaffee- und Mensapause oder einfach für Ermunterung und Unterstützung in der gesamten Zeit danken.
Abschließend geht ein ganz herzliches Dankeschön an meine Verlobte Lisa, die mich auch in frustrierenden Phasen stets motiviert hat, weiterzumachen, und mich jederzeit unterstützt hat.